

ABSTRACT

O'MARA, RYAN PATRICK. Retrospective Dosimetry for Nuclear Nonproliferation and Emergency Response. (Under the direction of Dr. Robert B. Hayes).

One of the primary challenges to ensuring nuclear safety and security is the relatively large amount of radiological material in the world compared to the number of trained professionals and detector systems available to collect the necessary data. As a result, the possibility always exists for the diversion of nuclear material for illicit weapons production, or worse for radiological mass casualty incidents. Efficient prevention or response to these scenarios is predicated on the development of technologies capable of detecting not only those nuclear materials that are accessible, but also those that may have been present in the past. While advancements in radiation detector technology push the ability to detect and assay materials directly accessible by those detection systems, conventional and even cutting-edge radiation detectors lack the ability to collect information about historical radiation environments.

Relatively recent advances in the ability to probe the electronic states of insulating, and semiconducting, materials have facilitated the ability to reconstruct the historical radiation environments experienced by those materials. By measuring the populations of the electrons in specific elevated energy states using recombination luminescence or resonant microwave absorption, it is possible to determine the doses received by an almost endless number of ubiquitous materials, such as quartz grains in earthen building materials, confectionary, aluminum oxide ceramics and even dust. This ability, known as solid-state dosimetry, effectively transforms everyday objects into always-on, passive dosimeters.

In this work, solid-state dosimetry techniques are applied to a number of nonproliferation and emergency response problems in order to demonstrate the untapped potential for luminescence and paramagnetic resonance dosimetry in these fields. It was shown that using

luminescence dosimetry in common building materials it is possible to identify the energy of a radiological source without needing to directly access the source while it is present (Chapter 4). Additionally, coupling particle transport modeling with dosimetry data from common place materials, it was possible, for the first time ever, to locate the historical position of radiological source material, even without prior knowledge about the source's identity or location (Chapters 9 and 10). Both of these capabilities may, in the future, aid inspectors or nuclear authorities to reconstruct undisclosed, past radiological activities. The ability to detect covert nuclear operations, past and present, will increase the deterrent strength of the nuclear nonproliferation regime and thus make diplomacy more attractive to States seeking to produce nuclear weapons. Further, coupling the techniques presented in Chapters 4, 9 and 10 with multiple solid-state dosimetry modalities, a physical dosimetry suite capable of responding to radiological mass casualty events was developed.

This work expanded the applicability of solid-state dosimetry from the traditional archeological dating problems, well into the realm of nonproliferation and emergency response. In furtherance of these novel applications, Chapters 6 and 7 showed how many of these techniques can even be implemented with even the most minimalistic sample preparation and analysis protocols. While Chapter 8 illustrated a technique for estimating minimum detectable anthropogenic doses with relatively modest radiation detection equipment. With some extra effort, it may be possible to extend the techniques and results presented herein to include dosimetry with single grains of particulate matter. If possible, this would open the door to even more impressive uses of solid-state dosimetry such as treaty verification through stand-off nuclear assay using materials released into the atmosphere from nuclear facilities or materials collected from environmental samples taken within nuclear facilities.

© Copyright 2020 by Ryan Patrick O'Mara

All Rights Reserved

Retrospective Dosimetry for Nuclear Nonproliferation and Emergency Response.

by
Ryan Patrick O'Mara

A dissertation submitted to the Graduate Faculty of
North Carolina State University
in partial fulfillment of the
requirements for the degree of
Doctor of Philosophy

Nuclear Engineering

Raleigh, North Carolina
2020

APPROVED BY:

Dr. Robert B. Hayes
Committee Chair

Dr. John Mattingly

Dr. Jeffrey A. Favorite

Dr. Tatyana Smirnova

DEDICATION

To my grandfathers Daniel O'Mara and Jack Middleton, grandmother Rose Anne O'Mara who passed away before the completion of this dissertation and grandmother Dotty Middleton for their lifelong love, memories and influence on my parents.

To my parents and sister for their endless patience, support, guidance and sources of inspiration during my many years in and out of school.

To my fiancée, Rachel, also for the love, support and patience during the course of this process. And especially for the adventures and all of the baked goods!

BIOGRAPHY

Ryan O'Mara was born in Emerald Isle North Carolina on March 18th, 1986 to Donald and Karrie O'Mara.

He received his first undergraduate degree in Radiological Sciences, in 2010, from the University of North Carolina at Chapel Hill and his second undergraduate degree in Physics in 2014. After a brief stint researching in the Raman Spectroscopy Lab at Appalachian State University, he entered the Nuclear Engineering graduate program at North Carolina State University.

His graduate work focused on nonproliferation and emergency response applications of solid-state dosimetry under the advisement of Dr. Robert Hayes. Additionally, he completed a graduate certificate in Nuclear Nonproliferation Science and Policy in 2018.

Throughout his graduate career he held a number of internships under the broader nuclear engineering umbrella, including at: Harris Corporation (2016), Los Alamos National Lab (2017, 2018) and Oak Ridge National Lab (2019). In 2019, he was also able to be a visiting researcher at The Technical University of Denmark (DTU), in Roskilde, DN, where he explored single grain optically stimulated luminescence dosimetry applications for nonproliferation and emergency response.

ACKNOWLEDGMENTS

“No man is an island entire of itself; every man is a piece of the continent, a part of the main;”
-John Donne

I am eternally grateful to the many, many people who helped along this journey and made this dissertation possible.

To Dr. Hayes who ensured there was never a shortage of pep and energy in the lab. In addition, he provided mentorship and plethora of opportunities for research collaborations, “crazy-cool science” to explore and numerous (seemingly endless) reviews of this dissertation, a number of journal submission and countless conference presentations all made this dissertation possible.

To my mentors at the national labs, namely Jeff Favorite and Will Wieselquist, whose mentorship and hospitality not only enhanced my internship experiences but also introduced me to many of the computational techniques found herein. Also, to all of my collaborators at Technical University of Denmark (DTU), and especially Mayank Jain, for the hospitality, the opportunity to research there and the expertise they were willing to share with me during my time there.

To my committee members Dr. John Mattingly, Dr. Tatyana Smirnova and Dr. Jeff Favorite, I thank you for the insights, critiques and expertise that you have shared with me through this process.

Finally, to my colleague and officemate Dr. Joseph Cope for always being the first to the lab and the last to leave, for the competitive drive whether in classes or in publishing, for constant reminders about policies and deadlines. You were a great friend, motivator, travel-mate, editor and sounding board during my time at State.

This work was funded in part by federal grant NRC-HQ-84-14-G-0059 from the Nuclear Regulatory Commission and through a joint faculty appointment between North Carolina State University and Oak Ridge National Laboratory in coordination with the Office of Defense Nuclear Nonproliferation R&D of the National Nuclear Security Administration sponsored Consortium for Nonproliferation Enabling Capabilities under Award Number DE-NA0002576. The National Criticality Experiments Research Center (NCREC) at the Device Assembly Facility (DAF) is supported by the DOE Nuclear Criticality Safety Program, funded and managed by the National Nuclear Security Administration for the Department of Energy.

TABLE OF CONTENTS

LIST OF TABLES.....	viii
LIST OF FIGURES	x
Chapter 1: Introduction	1
Chapter 2: Retrospective Dosimetry.....	5
2.1 Historical Perspective	6
2.2 Retrospective Dosimetry	7
2.2.1 Archeological Dating	7
2.2.2 Emergency Dosimetry	8
2.2.2.a Challenges	8
2.2.3 Nonproliferation Dosimetry	9
2.2.3.a Emergency Dosimetry	9
Chapter 3: Basic Concepts in Retrospective Dosimetry.....	11
3.1 The Luminescence Signal.....	12
3.2 Dose Reconstruction Techniques	13
3.3 EPR Dosimetry	16
Chapter 4: Dose Deposition Profiles in Untreated Brick Material	18
4.1 Introduction	19
4.2 Materials and Methods	19
4.3 Results	22
4.4 Conclusions	24
Chapter 5: Characterization and Inter-Calibration of Laboratory Irradiation Sources Used Used for Multiple Solid-State Dosimetry Modalities	25
5.1 Introduction	26
5.2 Materials and Methods	27
5.2.1 Gammacell 220 Dose Rate Calibration	27
5.2.2 Measurement of the Vertical Dose Rate Profile	28
5.2.3 Calibration Quartz Exposure	29
5.2.4 Risø TL/OSL Reader Internal Sr90/Y90 Dose Rate Comparison	31
5.3 Results	32
5.3.1 Gammacell 220 Dose Rate Calibration.....	32

5.3.2 EPR Measurement of the Vertical Dose Rate Profile	34
5.3.3 Calibration Quartz Exposure.....	37
5.3.4 Inter-modality Comparison	38
5.4 Conclusions	44
Chapter 6: Grain Size and Density Separation Effects on Luminescence Dose Estimates Using Brick Material	45
6.1 Introduction	46
6.2 Materials and Methods	47
6.3 Results	49
6.4 Discussion	51
6.5 Appendix A: Detailed Description of Dose Reconstruction Protocols	53
Chapter 7: Monte Carlo Analysis of Optimally Selected Dose Points for the Additive Dose Method for Retrospective Dosimetry	55
7.1 Introduction	56
7.2 Materials and Methods.....	57
7.2.1 Nonlinear Responses	58
7.3 Results	60
7.3.1 Nonlinear Responses	62
7.4 Conclusions	65
Chapter 8: Radionuclide Assay of Brick Material Using a High Purity Germanium Detector and Low-level Detection Facilities	66
8.1 Introduction	67
8.1.1 New Energy Efficiency Methodology	69
8.2 Description of Measurements	71
8.2.1 Low-level Counting Experiments	71
8.2.2 In-situ Laboratory Measurements	72
8.2.3 Dose Rate Calculation Description	72
8.3 Measurement Results	74
8.3.1 Low-level Counting Experiments	74
8.3.2 Laboratory Measurements	78
8.3.3 Dose Rate Simulation Results	79

8.4 Discussion	84
8.6 Conclusions	85
Chapter 9: Retrospective Assay and Localization of an Unknown Source Using Luminescence Dosimetry.....	86
9.1 Introduction	87
9.1.1 The Inverse Radiation Transport Problem	88
9.2 Materials and Methods	89
9.2.1 Sample Setup	89
9.2.2 The Source	90
9.2.3 Sample Preparation – Source Localization	91
9.2.4 Sample Preparation – Energy Assay.....	91
9.2.5 Computational Optimization	92
9.3 Results	94
9.3.1 Source Location	94
9.3.2 Source Energy	97
9.4 Discussion	100
9.5 Conclusions	101
Chapter 10: Three-dimensional Positional Analysis of Weapons Grade Plutonium Using Gridded arrays of Dosimeters	102
10.1 Introduction	103
10.1.1 Analytical Source Position Analysis	103
10.2 Materials and Methods	104
10.2.1 OSLD Measurement	106
10.2.2 Source Position Analysis	107
10.2.3 Inverse Transport Methods	108
10.3 Results	110
10.4 Conclusions	115
Chapter 11: Conclusions	118
REFERENCES.....	122
APPENDIX.....	128

LIST OF TABLES

Table 4.1	Outline of the Single Aliquot Protocols Used for Dose Measurements	21
Table 5.1	SAR Protocol Setting for Calibration Quartz Dose Reconstructions	31
Table 5.2	Thicknesses and Masses of the Alanine Dosimeters Used to Characterize the Dose Deposition in the Alanine Pellets Under Irradiation by the Risø Reader's Internal Beta Source.....	32
Table 5.3	NIST Certified Doses Received from the Laboratory Gammacell 220	33
Table 5.4	NIST Certified Dose to Each Alanine Pellet in Dosimeter 0708	33
Table 5.5	Fit Parameters Obtained for the Axial Dose Rate Distribution in the Gammacell 220.....	35
Table 5.6	Dose Rate Estimates for the Risø TL/OSL Reader Sr-90/Y-90 Beta Source	37
Table 5.7	Dose Rate of the Risø Sr-90/Y-90 source Measured with Three Separate Dosimetric Materials	38
Table 5.8	Fit Parameters Obtained for the Dose Rate of the Risø's Beta Source Measured with nanoDot OSLDs	39
Table 5.9	Doses Delivered to the Alanine Dosimeters Using the Risø Internal Beta Source, as Measured Using EPR.....	40
Table 5.10	Fit Parameters Obtained for the Dose-Dosimeter Thickness Relationship with Errors Given at the One Standard Deviation Level.....	40
Table 5.11	Fit Parameters Obtained for the Dose Rate Gradient Simulated Through the Depth of a Regular Alanine Pellet	43
Table 5.12	Correction Factors Relating Dose Estimates Between the Three Dose Reconstruction Modalities	44
Table 6.1	Aliquot Grain Size and Densities Obtained from Each Sample.....	48
Table 6.2	Percentage of Useable Dose Estimates, by Size, Density and Protocol, for Sample B3C1S1	49
Table 6.3	Percentage of Useable Dose Estimates, by Size, Density and Protocol, for Sample B3C1S2	50

Table 6.4 Dose Estimates in Gy, by Size, Density and Protocol, for Sample B3C1S1	50
Table 6.5 Dose Estimates in Gy, by Size, Density and Protocol, for Sample B3C1S2	51
Table 6.6 Outline of the Conventional Single Aliquot Protocol Used for TL and OSL Dose Measurements	53
Table 6.7 Outline of the Modified Single Aliquot Protocol Used for TL and OSL Dose Measurements	53
Table 8.1 Detection Limits and Isotope Activity Concentrations Measured on Detector G23	75
Table 8.2 Detection Limits and Isotope Activity Concentrations Measured on Detector G30	76
Table 8.3 Detection Limits and Isotope Activity Concentrations Measured on Detector H1	77
Table 8.4 Specific Activities Determined by Each of the Three Detection Suites	78
Table 8.5 Isotope Activity Concentrations Measured on the microDetective HPGe	78
Table 8.6 Total Internal Dose Rates for Photons, Beta Particles and Alpha Particles	80
Table 9.1 Comparison of Estimated Spatial Parameters with the Known Values.....	96
Table 10.1 Estimated Source Position Coordinates Calculated from the Dosimeters in the Small Array (SA) and Large Array (LA).....	112
Table 10.2 t-Statistics Comparing the Known and Estimated Source Positions	113
Table 10.3 Estimated Source Position Coordinates Calculated from the Dosimeters in the Small Array (SA) and Large Array (LA).....	114

LIST OF FIGURES

Figure 3.1 Schematic representation of the luminescence phenomenon	12
Figure 3.2 Schematic representation of the Zeeman effect that gives rise to the EPR dosimetric signal of interest	16
Figure 4.1 Experimental exposure configuration	20
Figure 4.2a Examples of the exposure configuration model constructed in MCNP: Orientation of the cylindrical source and OSLDs.....	20
Figure 4.2b Examples of the exposure configuration model constructed in MCNP: Source shown along with the core and horizontal slices.	20
Figure 4.3 IRSL/TL curves for slice 1and slice 6.....	22
Figure 4.4 Dose deposition profile measured for the brick sample compared to simulated values obtained using MCNP	23
Figure 4.5 Measured values of equivalent doses as a function of the MCNP predicted values	23
Figure 5.1 Sample irradiation setup used for the irradiation of alanine dosimeters and quartz samples	27
Figure 5.2 Sample irradiation setup used for determining the vertical dose rate profile within the Gammacell 220 irradiator. The alanine pellets appear as white circles in the middle of the irradiation chamber.....	29
Figure 5.3 Dose rate as a function of vertical position within the GammaCell 220 irradiation chamber showing 95%CL with the dashed bands stradling the best fit	34
Figure 5.4 Dose rates for NIST dosimeters 0701 and 0702 (black square and triangle, respectively) plotted with the measured dose rate profile for the GC220.....	36
Figure 5.5 Doses measured using the InLight microStarrii meducal dosimtry unit.....	39
Figure 5.6 Measured dose delivered by the Risø's internal beta source versus the thickness of the dosimeter	41
Figure 5.7 MCNP6® model geometry for the Risø reader internal beta source irradiations.....	42

Figure 5.8 Electron flux (e^-/cm^2) within a single alanine pellet irradiated by the Risø's internal beta source	42
Figure 5.9 Relative dose deposition in the simulated alanine pellet calculated by MCNP6®.....	43
Figure 7.1 Contrived example of a dose reconstruction as would be utilized in solid-state dosimetry methods for estimating historical exposures to insulator materials	56
Figure 7.2 Effect of the m_3 parameter in Equation 1 on the x -intercept of the dose response.....	59
Figure 7.3 Relative error in the x -intercept as a function of the x -intercept's percent of the maximum dose point	61
Figure 7.4 Optimum number of high dose points as a function of the size of the x -intercept relative to the maximum additive dose point	62
Figure 7.5 Relative error in the x -intercept as a function of the x -intercept's percent of the maximum dose point	63
Figure 7.6 Relative error in the x -intercept as a function of the number of dose points in the fitted distribution	64
Figure 7.7 Relative error in the x -intercept as a function of the multiplicative step-size between dose points.....	64
Figure 8.1 Experimental setup with the brick shield in place.....	72
Figure 8.2 Origen calculated gamma, beta and alpha spectra based on brick sample activity concentrations measured by detector G30	79
Figure 8.3a Mesh tally of internal dose rate (rad/hr) within a single brick	81
Figure 8.3b Relative uncertainties in the dose rate estimates	81
Figure 8.4a Mesh tally results of the internal dose rate (rad/hr) in a simulated brick when including all emissions including those from neighboring bricks	82
Figure 8.4b Relative uncertainties in the dose rate estimates	82
Figure 8.5 Histogram of calculated annual volume averaged dose rates within the brick material for the 200 sample runs	83

Figure 8.6 Kernel density estimate of annual volume averaged dose rates within the brick material for the 200 sample runs.....	83
Figure 9.1 Images of the mock wall constructed for testing the ability to retrospectively assay and locate the unknown source	89
Figure 9.2 Vised rendering of the mock wall irradiated at the DAF in the summer of 2018	90
Figure 9.3a Wall, rebuilt at North Carolina State University, with OSLD doses (mGy) placed in the relative locations of the dosimeters	94
Figure 9.3b Doses measured to tile glaze samples taken from the row of tile dots.....	94
Figure 9.4 Marginal posterior density distributions obtained for the x-y-z position of the simulated point source.....	95
Figure 9.5 Measured dose deposition in the brick core plotted against depth into the brick.....	97
Figure 9.6 Plot of the sum-squared residuals between the measured and simulated dose deposition profile in the brick near the minimizing energy value.	97
Figure 9.7 Gaussian fit to the inverted sum-squared residuals between the measured and simulated dose deposition profile in the brick	98
Figure 9.8 Calculated photon spectrum from prompt fission gammas exiting the HEU core	99
Figure 10.1 Outer view of the dosimeter arrays	105
Figure 10.2 Underside of the exposure geometry, showing the weapons grade plutonium source and both of the dosimeter arrays	106
Figure 10.3 Method for determining the three-dimensional position of a point source using the dose estimates in two orthogonal linear arrays	108
Figure 10.4 Coordinate system used for the dosimeter arrays with respect to the WGPu source.....	110
Figure 10.5 Measured doses to the OSLDs in the large array (LA)	111
Figure 10.6 Measured doses to the OSLDs in the small array (SA).....	112

Figure 10.7 Contour plot of measured doses to the OSLDs in the Large Array
(left), and Small Array (right) 114

Figure 10.8 Plot of the chi squared between the simulated and measured
dosimeters in the small array as a function of the simulated radius
(cm) 115

Chapter 1

Introduction

Since the early-1990s, the International Atomic Energy Agency (IAEA) has maintained a database of incidents involving misuse of nuclear materials. According to the IAEA's Incident and Trafficking Database (ITDB), between 1993 and 2017 there were 3235 confirmed incidents involving nuclear material and of those 278 involved confirmed, or likely, malicious use or trafficking (IAEA, 2018). Moreover, in 2017 alone, 166 incidents of unauthorized use or mishandling of nuclear materials were reported to the IAEA (IAEA, 2018).

Among the most important functions of the global nuclear regime is to ensure the protection of radiation workers, the public and the environment from the potentially hazardous effects of radiation. In general, this role can be thought of as a triad including safety, security and safeguards. The nuclear safety arm of this triad includes measures taken to prevent damage due to unplanned or unintended events involving radiological materials. Nuclear security shares a similar mission, only, the primary concern is prevention of intentional misuses of nuclear materials. In fact, nuclear safety and security often employ the same, or similar, systems (IAEA, 2010). In contrast, nuclear safeguards often refer to systems put in place to prevent the production or diversion of materials, facilities or activities for malicious purposes. Nuclear safeguards commonly refer to the measures used to ensure that state-level actors fulfill their promise to the international community to refrain from nuclear proliferation. Nuclear safeguards can be thought of as the guns, guards and gates associated with nuclear facilities.

One of the primary limitations of the current tools available to inspectors in the security and safeguards regimes is that detection and assay of radiologic sources requires access to both the source material and reliable records or accountancy from the inspected entity. However, there are many cases where the validity of the claims made by an adversary may be questionable. In such cases, it would be preferable to have tools capable of confirming claims about nuclear activities without needing direct access to nuclear materials or reliance on operator information. Such a capability would require, at least, a distributed network of detectors with the ability to record the presence and type of nuclear materials. Unfortunately, with conventional radiation detector technology such a vast array of detectors would be prohibitively expensive both monetarily and logically.

The primary consequence of concern resulting from a failure of any of the three nuclear protection pillars is an incident of mass-destruction or mass radiation exposure, to the public, due to inadequate control of nuclear materials. As a result, it is also important to develop measures

that can be used to mitigate the effects that may arise following an accidental or malicious mass-exposure event. In the literature, three main classes of radiological emergencies of concern have been identified (Jaworska, 2009). First, incidents involving improvised nuclear devices (INDs). Second, incidents involving orphaned sources, such as those that may be found in improperly discarded blood irradiators or research related sources. Finally, there are incidents involving the malicious use of radiation other than INDs. This category of radiological emergencies includes radiological dispersion devices (RDDs), or so-called dirty bombs, and radiological exposure devices (REDs). No matter which category of radiological emergency, rapidly acquiring information about the timing and method of exposure will be critical for consequence management and possibly attribution (Jaworska, 2009).

Immediately following a mass-exposure incident, it will be imperative to identify which members of the public have received biologically significant doses and will need further medical treatment. The ability to rapidly and accurately reconstruct doses to significant numbers of citizens will be essential to quell the mass panic that will surely follow any radiological emergency. Ideally, all members of the public would carry commercial personal dosimeters that could be used to accurately measure individual dosimetric and source energy information. Unfortunately, it would be neither practical nor economical to begin a national personal dosimetry program just in case of a nuclear emergency. However, as has been shown, by making use of ubiquitous materials, such as electronic components, nearly every individual in the developed world does in fact have some type of dosimeter on their person at all times (Hayes and O'Mara, 2019).

The purpose of this dissertation is to develop retrospective dosimetry techniques aimed at filling the aforementioned needs in the nuclear security and emergency response regimes. As it happens, interactions between radiation and matter create lasting electronic changes in the exposed materials that can be used to measure the doses received. In the following two chapters, three electronic phenomena that give rise to the possibility of retrospective dosimetry will be reviewed. Both optically or thermally stimulated luminescence (OSL or TL) and electron paramagnetic resonance (EPR) spectroscopy have been used in the literature to reconstruct historical doses for a variety of applications. One of the main benefits of these methods is that they have been shown to perform well for reconstructing doses using materials ubiquitous in the

developed world (O’Mara and Hayes, 2018; Hayes and O’Mara, 2019; Hayes, O’Mara and Hooper, 2018).

The fourth chapter will detail how retrospective dosimetry can be used in the realm of nuclear security to assay nuclear source material, after the source has been removed. It will be shown that by coupling measured dose deposition profiles in materials with simulations, it is possible to characterize the gamma-ray energy of the radiation field (O’Mara and Hayes, 2018). In the nuclear security context, this technique can be used to verify claims about nuclear operations using the physical structures that house those operations.

In general, OSL/TL is used to measure doses to inorganic, crystalline materials while EPR spectroscopy excels at dose reconstructions using organic molecules. The fifth chapter will detail efforts towards the development of a cross-calibration procedure between three retrospective dosimetry systems: a commercial Landauer microStar ii OSL dosimetry unit, a Risø OSL/TL reader and a Bruker EPR spectrometer (O’Mara and Hayes, 2020). Because luminescence and EPR dosimetry methods are better suited for different material types, it would be advantageous to be able to relate dose estimates across modalities. Successful implementation of such a cross-calibration would be especially useful in an emergency response situation as it would allow for dose estimates for affected individuals using any number of items likely to be on their person.

The ninth and tenth chapters will present work that has been performed towards further expanding the capabilities of retrospective dosimetry to include spatial reconstruction of source geometries, or source imaging. Once again, coupling simulations with physical measurements it is possible to determine positional or geometric qualities about radiological sources. Such a capability should be attractive to nuclear security and treaty verification operations, where constant, around-the-clock monitoring of all nuclear sources is necessary but not yet possible.

Chapter 2

Retrospective Dosimetry

2.1 Historical Perspective

Thermoluminescence (TL), the first of the relevant solid-state dosimetry phenomena discovered, dates back to the 1600s when Robert Boyle noted light emitted from diamond after “holding it upon a warm part of my Naked Body” (Boyle, 1663). However, the study of the thermoluminescence phenomenon did not begin in earnest until the late 19th century when Trowbridge and Burbank (1898) showed that the thermoluminescence from a fluorite sample could be depleted by heating and then re-induced by exposing the sample to x-rays. Following this discovery, thermoluminescence was first applied to the dosimetry problem in 1953 when lithium fluoride (LiF) was used by Farrington Daniels to measure the radiation following an atomic weapon test (McKeever, 1985).

As early as 1963, it was noted that the electron traps responsible for the TL signal in calcite could be bleached (depleted) by sunlight, as well as heat (Aitken et al., 1963). While the use of TL dosimetry methods continued growing throughout the 1970s and 80s, optically stimulated luminescence (OSL) finally arrived onto the scene in the early 1980s. In 1984, Derrick Huntley and company published the first account of using OSL to date archeological sediments (Huntley et al., 1985). Since this initial study, OSL methods have seen rapid advancements ranging from the discovery of new light-sensitive electron traps to the development of specialized materials for personnel dosimetry.

While TL and OSL methods developed in concert with each other, the third solid-state dosimetry phenomenon of interest, electron paramagnetic resonance (EPR), developed in a relative vacuum from the others. Another difference between the development of EPR and stimulated luminescence is that the EPR phenomenon was theorized before it was observed. The theoretical framework for EPR was first outlined by Stern and Gerlach in the 1920s; the Stern-Gerlach experiment asserts that the magnetic moment of an electron can only occupy discrete orientations relative to an applied magnetic field (Weil, 2007). It would be almost another 20 years before the first resonance peak from electron paramagnetic resonance would be observed in CuCl₂.2H₂O, by scientists in the former Soviet Union (Zavoisky, 1945). Following the end of World War II, the widespread availability and low cost of microwave systems (formerly utilized in radar instruments) led to a rapid utilization and advancement of EPR technology (Weil, 2007).

2.2 Retrospective Dosimetry

Retrospective dosimetry broadly refers to the determination of the magnitude of a delivered dose after the irradiation event has taken place. Traditionally, retrospective dosimetry with solid-state materials has been studied for limited applications: archeological dating, food irradiation detection, epidemiology and emergency dosimetry. For archeological applications, the technique relies on doses accumulated in phosphor materials due to the presence of naturally occurring radiological materials (NORM) in the surrounding environment. To the extent that the environmental dose rate can be accurately measured, the age (time since the last bleaching event) of the material can be calculated. Since the radiation flux attributable to NORM is generally minute, archeological dating studies rely on extremely long exposure times. Food dosimetry relies mainly on bones and shells, whereas epidemiology relies on teeth extracted through routine dental practices (being fitted for dentures, wisdom teeth, crowns etc.). Emergency response applications are generally concerned with large (relative to background) radiation doses delivered by anthropogenic sources of radiation to members of the public. In these cases, the anthropogenic dose will be added to any accrued background dose because current measurement techniques are typically unable to distinguish the background from anthropogenic dose. Based on the work in this dissertation, nonproliferation has been identified as an additional application of retrospective dosimetry.

2.2.1 Archeological Dating

Although luminescence dating developed slightly after it was proposed for accident dosimetry, much of what is known about luminescence dosimetry has come from the dating community. This is likely because dosimetric dating fills an important gap between the upper limit of radiocarbon (^{14}C) dating (~50000 years) and the lower limit of potassium-argon (K-Ar) dating (1,000,000 years). Archeological dating by retrospective dosimetry can be categorized into two categories, based on the history of the sample being investigated: (1) unheated sediments and (2) baked artifacts. For both types of samples, it is assumed that there was an event in which the radiogenic signal (trapped electrons and holes) in the material was zeroed, either totally or partially. In unheated sediments, the zeroing event may be the point at which the sediments formed by solidification deep in the Earth's crust or the last time that the sediments were exposed to sunlight. For baked artifacts, such as pottery, the last zeroing event took place

when the artifact was fired. After deposition of the sediment or artifact and subsequent burial, further exposure to sunlight is blocked and the luminescence signal begins to build-up in the material.

2.2.2 Emergency Dosimetry

Following a large-scale radiation exposure or mass-casualty event, prompt assessment of the radiation doses received by the general public, as well as emergency responders, will be of paramount importance to both directing response resources and managing public fear. Depending on the extent and location of the incident, the number of people seeking treatment or assessment may be on the order of hundreds of thousands or even millions (i.e. New York City alone has an evening population of almost 9 million). As recent events have shown, if public panic cannot be controlled, hospitals and medical care facilities can easily be overwhelmed by a flood of patients seeking dosimetric evaluations. As a result, the development of rapid radiation exposure triage infrastructure will be critical in separation of those needing treatment and the worried well.

While numerous triage levels have been proposed for responding to a radiological emergency, it is generally well accepted that the most critical dose level for triage is 2 Gy (Alexander et al., 2007; Jaworska et al., 2014). That is, above the 2-Gy whole body dose level, patients would be referred for follow-up medical care and may even require subsequent intervention (Guskova et al., 1988). As a result, any technology developed for radiological triage would need to be at least sensitive enough to accurately detect radiations doses down to 2 ± 0.5 Gy.

2.2.2.a Challenges

Beyond the lower dosimetric limit of interest, 2 Gy, there are a number of challenges in emergency response dosimetry. Namely, the need for rapid dose readouts precludes the use of time-consuming sample preparations that are pervasive in archeological dating studies. Chapters 4 and 6 demonstrate efforts made to maximize the amount of dosimetric information available with little-to-no sample preparation. Still, the sample read out and dose reconstruction remains the most time-consuming part of the luminescence dosimetry studies. It is shown in Chapter 7 how optimizing the selection of dose reconstruction protocol parameters can minimize the inherent, high-throughput uncertainty in the reconstructed doses. Additionally, the entirety of the effectiveness of retrospective dosimetry for emergency response scenarios rests on the

assumption that a significant number of patients seeking care will be carrying common objects capable of recording their dose.

2.2.3 Nonproliferation Dosimetry

The general goal of nuclear nonproliferation is to prevent the illicit production of nuclear weapons through the diversion of nuclear material and covert nuclear activities. The applicability of retrospective dosimetry for nonproliferation is dependent on the amount of information that can be garnered from gross dose measurements, in ubiquitous materials. From a solid-state dosimetry point-of-view, the dosimetry problem is a marriage between the archeological and emergency response applications. In the nonproliferation realm, the doses to the samples would be expected to be generated from longer time scales (compared to emergency scenarios) due to exposure by lower intensity anthropogenic sources.

Although an emerging application, it has been demonstrated that retrospective dosimetry can provide both energy (O’Mara and Hayes, 2018; Chapter 4) and positional (Hayes and O’Mara, 2020; Chapter 9; Chapter 10) information about historical sources. The ability to reconstruct source energy and position using ubiquitous materials may allow inspectors to verify the past radiological activities at nuclear facilities even in the absence of any source material.

2.2.3.a Challenges

The challenges for retrospective dosimetry applications in nonproliferation are much the same as those for emergency response. Since timely detection of illicit radiological activities is ultimately of interest, rapid sample preparation and readout is desirable. Like in an emergency response scenario, nonproliferation related studies would have to be performed with whatever dosimeter material is available. As a result, the ability to obtain dosimetric information from a variety of materials is both desirable and necessary. An additional challenge for nonproliferation applications though, is the likelihood that any materials that could be used for dose reconstructions would need to be surface removable samples (assuming light and electrical fixtures are not removable and replaceable). Since environmental smears are routinely collected during radiological surveys, these smears would be the most likely avenue for sample collection. Performing dosimetry with surface removable materials presents a number of challenges including small sample sizes and the potential for sample populations with different levels of partial bleaching. When sample sizes are adequately large, retrospective dosimetry using EPR

may mitigate the problem of partial bleaching via differential trap population analysis for those traps with characterized lifetimes and cross sections (Hayes, O'Mara, Abdelrahman, 2019).

However, when sample sizes are small and partial bleaching is likely, then advanced luminescence techniques such as single grain OSL may be the only available option.

Chapter 3

Basic Concepts in Retrospective Dosimetry

3.1 The Luminescence Signal

The luminescence phenomenon is best described using the band gap model of solid-state physics, see Figure 3.1. Under the band model, electrons can have energies that exist in quasi-continuous energy bands that arise from the atoms forming a crystal lattice. The two bands of importance in the luminescence process are the valence and conduction bands. Electrons with energies within the valence band are primarily involved in atomic bonding and are confined to the bonding atoms. In contrast, electrons with energies within conduction band are relatively free to move throughout the volume of the crystal. In insulators and semiconductors, the valence and conduction bands are normally sufficiently separated, in energy, by the band gap (the energy difference between the top of the valence band and the bottom of the conduction band) such that electrons cannot move between the valence and conduction bands. As a result, the conduction band remains empty of electrons and the material does not conduct electricity.

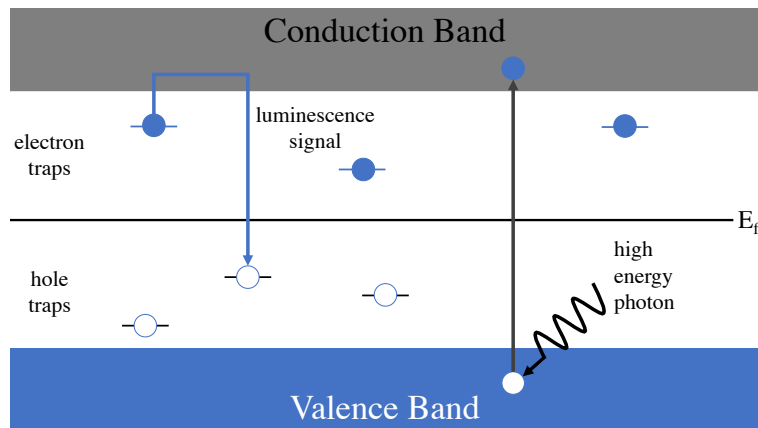


Figure 3.1. Schematic representation of the luminescence dosimetry phenomenon.

When a crystalline material absorbs an amount of energy greater than the band gap (ionization), electrons may be promoted from the valence band into the conduction band, leaving behind a hole in the valence band. In this context, a hole is defined as the excess positive charge resulting from the liberation of a bonding electron. If no metastable states exist within the crystal, then the electron will generally recombine with a hole in the valence band by means of stepwise relaxation (energy loss). However, in real crystals lattice defects such as inclusions, vacancies or dislocations can create localized metastable energy states that lie within the band gap, also known as traps. At these so-called traps the electrons or holes can become bound at the impurity site for on the order of hundreds of thousands of years (if near the Fermi energy, E_f).

The generation of the luminescence signal, for dosimetry, begins with an electron absorbing energy from a high-energy photon; resulting in the electron being excited from the valence band into the conduction band and the formation of a hole in the valence band. When the electron moves into proximity of a lattice defect with an excess positive charge, it may lose energy by becoming trapped at the defect site. Similarly, the resultant hole may travel throughout the valence band and become trapped at a negatively charged defect site replacing an electron below the Fermi energy in a hole trap (Figure 3.1). Once trapped, the electrons will remain at these defect sites until an energy greater than the difference between the trap and conduction band can be imparted to the material.

Below the saturation dose (ranging from 10 to 1E5 Gy depending on the material and its defect distributions), the number of trapped charges is proportional to the dose absorbed by the material. Thereby, the material itself holds a permanent record of the integral dose received. In TL and OSL, heat or light, respectively, is used to excite trapped electrons back into the conduction band. The excited electrons can then recombine at a lower energy level, whereby the recombination energy is dissipated as a visible light photon. The number of recombination events, and photons emitted, will be proportional to the number of trapped electrons and the number of recombination centers present in the material. As a result, counting the number of photons emitted gives a means to count the number of trapped electrons following irradiation. However, in order to relate the number of photons released following stimulation to a known radiation dose, the dose response of the material must be known. The material's dose response is determined by administering successive doses to the material using a calibrated radiation source.

3.2 Dose reconstruction techniques

For retrospective, luminescence dosimetry the quantity of interest is the total absorbed dose (usually in Gy) to the material of interest. In general, the total absorbed dose, D_T , can be separated into two main components, the cumulative dose due to natural background radiation D_{BG} and the cumulative dose to anthropogenic sources of radiation D_X . Although it is generally not possible to discriminate the background dose from the anthropogenic dose, the background dose is the product of the age of the material, A , and the effective annual dose-rate in the material's environment R_{BG} . Here, the age of the material refers to the date of the last signal clearing process, i.e. high-temperature firing or exposure to light. If the material's age and

effective annual dose rate can be known, then the anthropogenic dose can be extracted through $D_X = D_T - D_{BG} = D_T - A/R_{BG}$.

The most difficult step in the process of retrospectively determining dose from electronic signals is relating the number of trapped electrons to a dose, finding the dose response. In commercially produced dosimetry materials, the number of trapped electrons per unit dose is precisely known prior to irradiation allowing dose calculation based on material consistency. However, in ubiquitous materials such as bricks and tiles, the dose response is not known beforehand. As a result, dose reconstruction protocols must be used to determine the unique dose response behavior of the sample-at-hand. From this, one can use the measured dose response relationship to calculate the cumulative dose absorbed by the material.

A dose reconstruction protocol consists of a set of laboratory irradiations and luminescence measurements that are used to relate a measured, natural luminescence signal to an absorbed dose. Presently in the literature, there are two pervasive dose reconstruction schemes, or protocols, additive-dose (AD) methods and regenerative-dose methods. In general, the dose reconstruction protocols hinge on some form of interpolation, or extrapolation, of the measured natural luminescence signal in relation to the signal measured after laboratory irradiations. Dose reconstruction protocols can be further categorized as multiple aliquot or single aliquot methods. Multiple aliquot methods separate the sample into multiple sub-samples, or aliquots, and use the aliquots to measure a calibration curve for the dose response of the material in terms of signal intensity per applied dose. Multiple aliquots have the benefit that they aren't subject to sensitivity, the amount of light output per unit dose, changes during dose measurements, since each sample is only measured once. However, because they utilize multiple aliquots, it must be assumed that the sensitivity of each of the aliquots is precisely the same. In contrast, single aliquot methods use a single aliquot to both measure the natural luminescence signal and construct the dose response, or calibration, curve. The main disadvantage to single aliquot methods is that repeated irradiation and high temperature heating is likely to induce sensitivity changes in the aliquot during the dose reconstruction protocol.

In additive-dose protocols, the calibration curve is built by carrying out laboratory irradiations before measuring the cumulative signal. That is, the laboratory doses are added to the natural dose in sequential aliquots and at increasing doses. The luminescence signal measured after the additive irradiations can then be plotted against the added applied dose. The equivalent

dose to the sample can then be determined by back extrapolation of the calibration curve to the zero-intercept of the horizontal (absorbed dose) axis (conventionally plotted as the x-axis). One major drawback for additive dose protocols is that the dose estimate is based on extrapolation of the measured calibration curve. The disadvantage here is that uncertainty in estimates based on extrapolation grow outside of the bounds of measured data.

Another additive dose technique, known as the pre-dose technique, seeks to make use of the sensitivity changes caused by exposure to radiation. The pre-dose technique is based on sensitivity changes to the 100°C thermoluminescence peak that occur as a result of the combined effects radiation exposure followed by rapid heating (Bailiff, 1994). The sensitivity of the sample is taken to be the signal measured after administration of a small test dose. The sample is then rapidly brought to a high temperature (~500°C at 10°C/s) for thermal activation, and the signal is again measured after administration of the same small test dose. Repeating thermal activations and administration of test doses, the dose to the material can be estimated from sensitivity changes in the sample.

Regenerative dose protocols utilize interpolation of the calibration curve. Regenerative dose protocols consist of a sequence of steps where the luminescence signal is bleached (erased by illumination), then the sample is irradiated to a known absorbed dose using a standard source, and the resultant “regenerated” OSL signal is measured (Yukihara, 2011). The equivalent dose for the sample is then determined by interpolation of the regenerated signals to determine the equivalent dose of the natural signal. One of the main drawbacks of regenerative dose protocols is that they are based on the assumption that the sensitivity of the sample to the source of the natural signal is similar to the sensitivity to laboratory source. In the context of luminescence dating, this assumption may be invalid if the sample’s sensitivity is dependent on the source dose rate or sequential anneal physics. Additionally, the regenerative dose protocols are inherently single aliquot and may suffer from sensitivity changes induced in material during the measurements.

One of the most widely used dose reconstruction protocols for estimation of equivalent doses using OSL is the single aliquot regenerated dose (SAR) protocol. The SAR protocol was developed for the purpose of accounting for potential sensitivity changes in the sample material due to the measurement protocol. The novel aspect of the SAR protocol is the addition of an extra irradiation step after measurement of the regenerated dose signal. The extra irradiation

steps are included to track any sensitivity changes in the sample being measured. It has been proposed that if the sensitivity changes linearly throughout the dose reconstruction protocol, then the resultant dose estimate can be corrected for that sensitivity change.

3.3 EPR Dosimetry

The generation of the measurable signal in EPR dosimetry occurs in much the same way as luminescence signals. Radiation interactions with organic materials cause the formation of free radicals, or unpaired electrons, within the material. For a given range of doses, the number of unpaired electrons is proportional to the dose absorbed by the material. EPR has an advantage in also being able to directly measure trapped holes (which represent unpaired electrons located below the Fermi level) unlike TL/OSL. The magnitude of the integrated EPR signal is then used to quantify the number of unpaired electrons in the material.

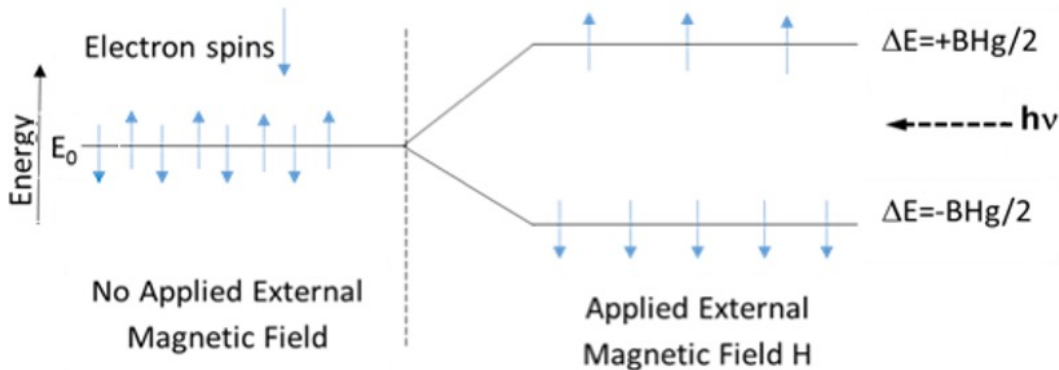


Figure 3.2. Schematic representation of the Zeeman effect that gives rise to the EPR dosimetric signal of interest.

A simplified schematic of the theory explaining the EPR signal is presented in Figure 3.2. In the absence of an applied magnetic field, unpaired electrons exist in energy levels corresponding to the trapped state of an associated radical species. When a strong magnetic field is applied, the energy levels split into aligned and anti-aligned, with respect to the applied magnetic field, states. The energy difference between the aligned and anti-aligned states, ΔE , is proportional to the external magnetic field strength H , the magnetic moment of the electron (or its orbital) B with the proportionality constant g (often called the g -factor) such that $\Delta E = BHg/2$. Application of a microwave field of specific frequency can supply necessary energy to flip the alignment of the electrons' magnetic moments parallel to the applied magnetic field.

In EPR dosimetry, an irradiated sample is placed in a resonant cavity with a fixed magnetic field. Microwaves are then delivered via a waveguide while measuring the incident and reflected resonator field strengths with a lock-in amplifier. At the point where the incident microwave photon energy is equal to the energy separation between the aligned and anti-aligned states, resonance absorption will be observed. The absorption of incident microwaves will manifest as a decrease in microwave field within the resonator cavity. The magnitude of the resonance absorption effect will be proportional to the number of unpaired electrons and therefore the absorbed dose for the radiogenic signals.

While EPR dosimetry and stimulated luminescence dosimetry take advantage of very similar physical mechanisms, there are some marked differences between the two techniques that can be exploited in order to provide coverage over a wide range of dosimetry scenarios. For example, stimulated luminescence dosimetry is better suited for inorganic insulator materials (due to amplification with the PMT) while EPR dosimetry is well suited for organic molecules due to their opacity for light transmission. As will be shown in Chapter 5, it is possible to cross-calibrate these two techniques such that precise, corroborating dose estimates can be generated with nearly any non-conducting material (O'Mara and Hayes, 2019). This ability is of particular interest to dosimetry using particulate matter from environmental samples, where there is little control over the type of material that may be collected (Hayes and O'Mara, 2018; Hayes, O'Mara and Abdelrahman, 2019).

Chapter 4

Dose Deposition Profiles in Untreated Brick Material

This material was published as:

O'Mara RB, Hayes RB. Dose deposition profiles in untreated brick material. *Health Phys.* 114(4), 414-420, 2018

This chapter has been published in the Health Physics Journal

4.1 Introduction

The benefit, to the radiation response community, of having a permanent record of radiation exposure is quite clear. However, the applicability of luminescence methods is limited by a variety of factors, including long sample preparation times, the necessity of harsh chemicals for sample preparation and that signal measurement is destructive to the signal. For both TL and OSL it is, in general, beneficial to have samples that are optically transparent and very small in size. As a result, the sample preparation generally includes crushing the samples and treating them with harsh chemicals, such as HF and HCL, to remove surface layers and impurities from the sample of interest.

Very few studies have been conducted to determine whether a suitable signal can be acquired from samples that have not been chemically treated. However, in 1995, Bøtter-Jensen, Junger and Poolton showed that radiation dose depth profiles could be directly measured with OSL scanning of untreated brick cores. This work attempts to build on that work, to determine if grain-size separation of the brick core material increases the quality of the signal.

The value in exploring such methods is two-fold. First, one of the major disadvantages of luminescence techniques for retrospective dosimetry is that traditional sample preparation techniques can be time consuming, if not tedious (Bøtter-Jensen and Murray, 2001). If satisfactory results can be obtained without the necessity of density separation and chemical treatment, then sample throughput should be able to be increased significantly. Second, negating the requirement of a full wet chemistry laboratory will represent a significant step toward the ability to make in field dose measurements with luminescence analysis.

4.2 Materials and Methods

Two generic, red bricks were purchased at a local home store. A 100 mCi, encapsulated Americium-241 source was placed between the two bricks for 3 hours and 18 minutes. Four Landauer nanoDot optically stimulated luminescence dosimeters (OSLDs) were placed around the source as a means of localizing the source for subsequent simulations. Figure 4.1 shows the exposure configuration with the top brick removed. The encapsulated Am-241 source was laid on top of the bottom brick and then another brick was placed on top of the first brick, sandwiching the source and OSLDs.



Figure 4.1: Experimental exposure configuration. The source--centered metal rod--was placed on the brick between 4 nanoDot OSLDs. The OSLDs served as independent verification for the source position.

After the exposure, spatial measurements were made, from photographs of the exposure configuration, to determine the approximate position of the source on the brick. A Monte Carlo n-particle (MCNP) model of the exposure configuration, was then built from the photographic measurements (Goorley, et al., 2011). The MCNP *pstudy* module was used to perform a perturbation analysis on the source and core locations to precisely determine the most likely location of the source (Brown et al., 2004). Figure 4.2 shows two orthogonal projections from the simulated exposure configuration. By comparing the results of the MCNP6 simulations to the doses measured to the OSLDs, the location of the source relative to the locations of the OSLDs was independently verified.

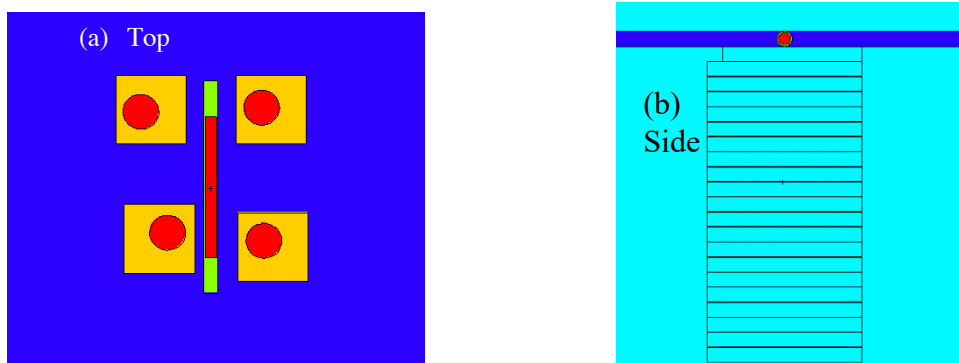


Figure 4.2. Examples of the exposure configuration model constructed in MCNP. (a) Shows the orientation of the cylindrical source and OSLDs (squares). In (b), the source is shown along with the core and horizontal slices. The red circle indicates the source position, and slices are numbered from top to bottom.

After localizing the source position, a 1-inch diameter core was taken from directly under the inferred source location. The removed core was then soaked overnight to ensure that the brick matrix was saturated. After soaking, the volume of the core was measured using liquid displacement. Following the volume measurement, the core was then oven-dried at 40°C for

three days and the mass was measured. The density of the core was then determined to be 2.24 g/cc.

The measured core density was used to update the original MCNP model for subsequent calculation of the theoretical dose to each layer of the sample core. There errors associated with the MCNP doses were calculated using MCNP *pstudy* to perturb the experimental observables, keeping all results in which the doses to the 4 OSLDs agreed to within $\pm 20\%$ of the measured values. A more in-depth discussion of the MCNP parameter studies can be found in the authors' other works (O'Mara and Hayes, 2017).

The brick core was then sliced, along its length, into twelve approximately 2-mm thick wafers using a low-speed Buehler IsoMet saw. Based on the MCNP calculations, the dose to the brick at depth of 4 cm was expected to be approximately 30 mGy, close to the detection limit for luminescence studies, therefore only 12 slices were taken. The 12 slices were then crushed and sieved into two grain size ranges, 90 to 250 μm and less than 90 μm . Since grains in the 90 to 250 μm size range are generally regarded as optimal (Wintle and Murray, 2006), those grains were saved for further processing, i.e. density separation and/or chemical treatment.

To test the abilities of OSL to measure dose depth profiles with minimal processing, the less than 90 μm grains were used. With no further processing, TL/OSL measurements were made on the less than 90 μm grains using a Risø TL/OSL-DA-15 reader (DTU Nutech, Denmark) fitted with blue light emitting diodes for OSL stimulation. The measurement approach was a modified infrared stimulated luminescence (IRSL), pulsed OSL (POSL) protocol based on the approach by (Colarossi et al., 2015). Table 4.1 shows the steps in the measurement protocol.

Table 4.1. Outline of the Single Aliquot Protocols Used for Dose Measurements.

Step	Description
Step 1	Dose (β source exposure, 0 s for natural dose)
Step 2	"Preheat" (TL at 260°C for 10 s)
Step 3	Infrared stimulated luminescence (40 s at 220°C)
Step 4	Pulsed optically stimulated luminescence (250 μs , 50 μs on, 50 μs off)
Step 5	Test dose (β source exposure for 300 s)
Step 6	"Preheat" (TL at 260°C for 10 s)
Step 7	Infrared stimulated luminescence (40s at 220°C)
Step 8	Pulsed optically stimulated luminescence (250 μs , 50 μs on, 50 μs off)

Figure 4.3 shows an example of the TL and IRSRL curves obtained for slice 1 (closest to the source) and slice 6. In slice 6 it was found that the optical luminescence signal was comparable to the noise level in our instrument and was therefore of limited utility. However, the TL signal for these samples exhibited a much better signal to noise ratio and was therefore selected to reconstruct the dose. Under this scheme, the signal of interest was taken to be the TL signal from the isothermal portion, 260°C, of step two. In order to account for sensitivity changes in the samples, the TL signal from the 220°C peak was measured for each test dose. This method yielded much more stable estimated dose calculations in the samples with lower doses, and also improved the recuperation (luminescence signal intensity at 0 Gy dose) values across all of the samples.

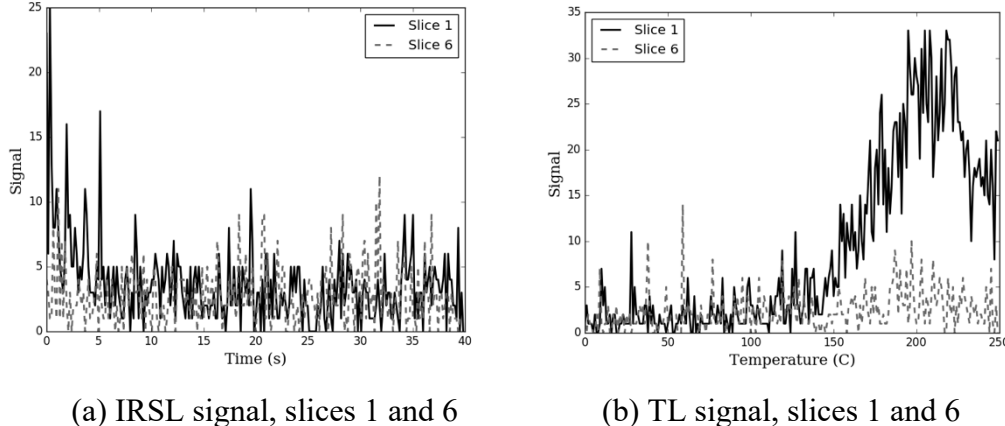


Figure 4.3. IRSRL/TL curves for slice 1 (solid) and slice 6 (dashed). The respective plots show the difference between the magnitudes of the curves for the two slices. Since the dose is estimated from the area under the curve, the larger the vertical displacement of the curve, the higher the estimated dose.

4.3 Results

Figure 4.4 shows the dose depth profile obtained from the measured samples, along with the estimated doses from the MCNP calculations. It can be seen from Figure 4.4 that the MCNP simulated dose values agree well with the measured doses, with each measured dose lying within the uncertainty interval for the simulated dose. The largest uncertainty in the simulated dose results was associated with layer number one. This is likely due to a combination of a significant defect that was present in the layer closest to the source coupled with the first layer having the greatest sensitivity to the experimental parameters. The defect in the first layer was affected by chatter in the coring bit, resulting in the loss of approximated 15% of the layer material. This

experimental detriment was modeled in the MCNP parameter study and resulted in even greater sensitivity of the dose in the first layer with respect to source positioning.

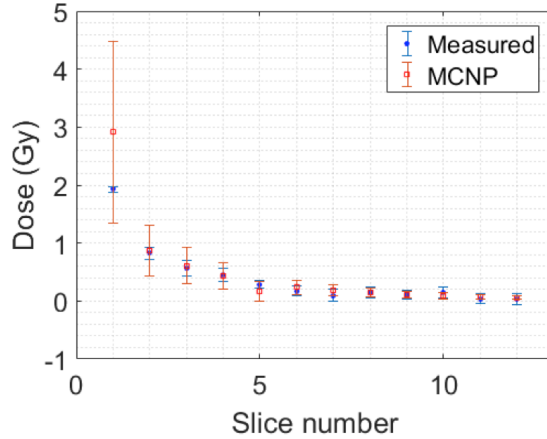


Figure 4.4. Dose deposition profile measured for the brick sample compared to simulated values obtained using MCNP.

From Figure 4.4, there also appears to be no consistent bias in the measured dose versus the simulated doses. Another way to test for the presence of a bias in measured data, compared to simulated data, is to plot the measured data as a function of the simulated data. Figure 4.5 shows a plot of the measured doses in all 12 layers versus the simulated doses. Figure 4.5 indicates that there is no consistent bias in the data versus the one-to-one correspondence line. As a result, it can be concluded that disagreement between the modeled doses and the measured doses are the result of random errors.

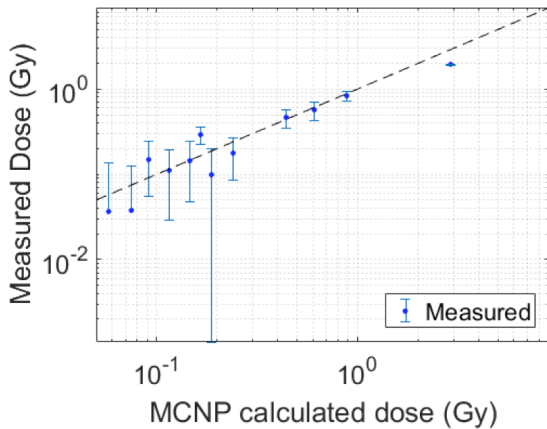


Figure 4.5. Measured values of equivalent doses as a function of the MCNP predicted values. The close adherence to the one-to-one (dashed) line indicates the lack of a bias in the measured doses.

4.4 Conclusions

It has been demonstrated that acceptable dose deposition profiles can be obtained from minimally prepared brick samples. This is an important development with respect to rapid processing of samples in the wake of nuclear incidents. Although it was found that the samples used here exhibited far less optical sensitivity than thermal sensitivity, this effect should be studied for larger grain sizes. Nonetheless, the thermal sensitivity of the samples in the study was sufficient to reliably reconstruct doses down to 36 mGy, comparable to the detection limits found with conventional OSL sample preparation. While the results from this study are a promising first step, more work should be devoted to fully characterizing the thermal response observed in this study.

Chapter 5

Characterization and Inter-Calibration of Laboratory Irradiation Sources Used for Multiple Solid-State Dosimetry Modalities

This material was submitted as:

O'Mara RP, Hayes RB. Characterization and Inter-Calibration of Laboratory Irradiation Sources Used for Multiple Solid-State Dosimetry Modalities. *Meas. Sci. and Tech.* 2019. (Submitted)

5.1 Introduction

As nuclear technology becomes more prevalent on a global scale, there is a risk of increased incidence of radiological incidents whether due to nuclear accidents or acts of terrorism. Following a radiological incident, it would be desirable for all affected individuals to be equipped with personal dosimeters. Such a capability would allow for rapid, accurate assessment of the doses received by those individuals. The benefit of being able to rapidly discriminate the worried well from those needing immediate medical attention cannot be understated (Hayakawa, 2016).

Presently, nuclear incident response for population exposure triage utilizes biodosimetry to determine the likely doses received by affected individuals (Alexander et al., 2007). Biodosimetry, however, has major drawbacks that will limit its effectiveness in the wake of a large-scale nuclear incident. Most notably, biodosimetry requires the cytogenetic analysis of an affected individual's blood for dicentric chromosomes (with lymphocyte kinetics and time to emesis if available). This involves constraints both in the number of patient blood samples that can be retrieved in a given period of time and in the number of blood samples that can be analyzed following a nuclear accident. Some estimates have indicated that an upper limit of approximately 100 samples per week could realistically be processed given the current biodosimetry infrastructure in the United States (REAC/TS, 2017). It is conceivable that a large radiological event in a major US city could easily swamp this infrastructure, leading to widespread panic and the potential for mental scarring of affected individuals (Rahu et al., 2015).

An alternative to biodosimetry that has been shown to have promise for future accident dosimetry practices is physical dosimetry. In physical dosimetry, doses received by individuals are reconstructed using doses to materials on the person's body. McKeever and Sholom (2016) have argued that physical dosimetry has comparable, or better, accuracy and precision to biodosimetry while also being easily scalable. As a result, there is a significant need for the development of physical dosimetry methods and techniques that could be implemented in the aftermath of a radiological emergency. Two of the most promising modalities for physical dosimetry are luminescence methods and electron paramagnetic resonance (EPR) (Alexander et al, 2007; Hayes and O'Mara, 2019).

In this study, a round-robin calibration of three dosimetry systems is performed using, as a calibrated reference, an in-house National Institute of Standards and Technology (NIST) EPR

calibrated Gammacell 220 irradiator. The dosimetry systems characterized in this analysis consist of a Landauer® microStar ii medical OSL unit, using nanoDot OSLD's, a Bruker EMXmicro EPR spectrometer, using alanine pellets, and a research-grade Risø TL/OSL spectrometer, using German secondary standard calibrated quartz. By characterizing the comparative responses between the three dosimetry systems, it will be possible to relate any dose measured by one system to the expected dose that would be measured with the other two. This will allow for secondary dose rate verification in future dosimetric studies involving multiple measurement methodologies.

5.2 Materials and Methods

5.2.1 Gammacell 220 Dose Rate Calibration

The laboratory is equipped with a Gammacell 220, consisting of 48 ^{60}Co pencil sources arranged in an annular array. The dose rate in the irradiation chamber was initially certified to be $9.58 \times 10^3 \pm 2.2\%$ Gy h⁻¹(air) in May of 1970. The first step in the laboratory cross-calibration was to perform a high-quality calibration on the in-house irradiator. The calibration was performed using five alanine transfer standard dosimeters (hereafter referred to as “standard dosimeters”) provided by the NIST. Each standard dosimeter consists of 4 alanine pellets, 4.9 mm in diameter and approximately 2.5-2.7 mm thick (Humphreys et al., 1998).

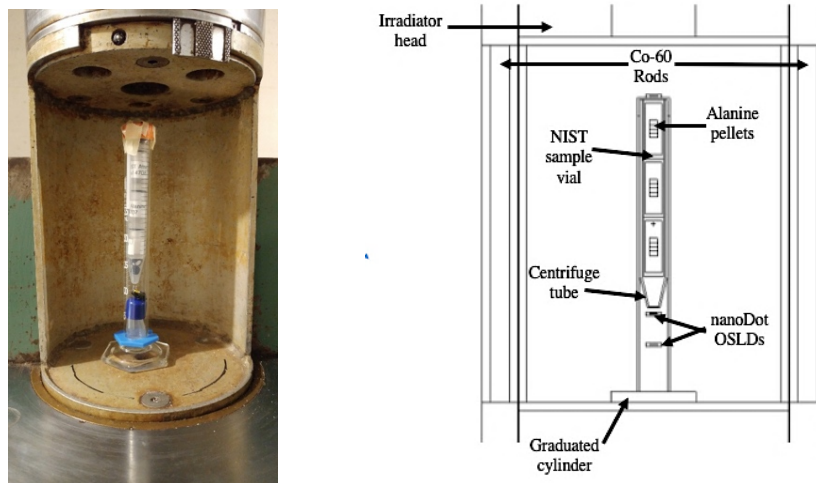


Figure 5.1. Sample irradiation setup used for the irradiation of alanine dosimeters and quartz samples (left) with MCNP6® modeled irradiation geometry (right).

The NIST dosimeters came housed in polystyrene cylinders. Three of these polystyrene cylinders (identification numbers 0706, 0707, and 0708) were stacked vertically in a Corning 15mL centrifuge tube and then placed in a fused borosilicate 25mL graduated cylinder (see Figure 5.1). The graduated cylinder was composed of ASTM E1266 Class A borosilicate glass with an outside diameter of 2.01 cm and inside diameter of 1.76 cm and a wall thickness of 0.125 cm. The Corning centrifuge tube was composed of polypropylene, with an outside diameter of 1.64 cm, an inside diameter 1.46 cm and a wall thickness of 0.09 cm. This sample holding configuration (sample holder 1) was used for the subsequent irradiations to ensure repeatability of the exposures. The graduated cylinder containing the standard dosimeters was then placed in the center of the Gammacell irradiator and irradiated for 16.05 hours.

One month before dosimeters 0706, 0707, and 0708 were irradiated, two additional NIST EPR dosimeters, 0701 and 0702, were irradiated alone for 26 hours and 97.83 hours respectively. These dosimeters were placed on a 10.16-cm tall polystyrene graduated cylinder, as a pedestal, during irradiation. All of the exposed standard dosimeters were returned to NIST for dose assessment.

5.2.2 Measurement of the Vertical Dose Profile

The vertical dose rate profile of the Gammacell central axis was measured using EPR with commercial alanine dosimeters via the Bruker EMXmicro spectrometer. The commercial alanine dosimeters used in this study were furnished by Harwell Dosimeters and consisted of a single alanine pellet, approximately 4.9 mm in diameter by 2.7 mm thick. Twenty-two alanine dosimeters were positioned with their horizontal axes in an array centered in sample holder 1. Each dosimeter was separated by an average center-to-center distance of 6 mm. The graduated cylinder containing the alanine dosimeters was then placed in the middle of the Gammacell's irradiation chamber and exposed for approximately 16 hours. Figure 5.2 shows the alanine dosimeters used for the vertical dose rate calibration inside the irradiation chamber.



Figure 5.2. Sample irradiation setup used for determining the vertical dose rate profile within the Gammacell 220 irradiator. The alanine pellets appear as white circles in the middle of the irradiation chamber.

All EPR spectra were collected with the alanine pellets in thin-walled quartz tubes and with the center of the alanine pellet positioned in the center of the resonator. The spectrometer parameters consisted of $796 \mu\text{W}$ microwave power, a 1G modulation amplitude, 150 G spectral width, 10^4 receiver gain, 20.5 ms conversion time and 100 ms time constant. Each spectrum consisted of 10 scans. Spectral manipulations included empty EPR tube subtraction and a linear background subtraction following the application of an exponential window function to dampen high frequency Fourier components in the spectra, as described elsewhere (Hayes et al., 2000). Three independent measurements were performed on each dosimeter. The closely packed alanine dosimeters provided a high-resolution dose rate profile for the laboratory's Gammacell irradiator for normalization to the NIST dose rate measurements.

5.2.3 Calibration Quartz Exposure

Unirradiated, sensitized quartz was provided by the manufacturer (Risø) for calibrations (Hansen et al., 2015). An aliquot of this calibration quartz was loosely loaded into a cylindrical polystyrene vial (3.25 cm long with 0.63 cm ID). The polystyrene vial was then placed inside of a centrifuge tube. Landauer nanoDot OSLDs were also placed inside the centrifuge tube, above and below the ampule containing the calibration quartz. The centrifuge tube was then tightly wrapped in black plastic to ensure that the quartz sample inside was protected from light degradation. The plastic wrapped centrifuge tube was then placed inside the same fused silica graduated cylinder as described in Section 5.2.1. The graduated cylinder was then placed in the

center of the Gammacell irradiator and exposed for 15 minutes. The measured dose rate profile of the Gammacell irradiator was used to calculate the dose rate to the sensitized quartz sample at its position in the cavity. Since the measured dose rate profile displayed a trend with vertical position in the irradiator cavity (discussed in Section 5.3.2), the dose to the quartz sample was taken to be the average expected value over the length of its distribution in the polystyrene vial. Additionally, the decrease in the dose rate to the quartz sample caused by attenuation of the sample holder and sample vial was accounted for using MCNP6® simulation (Goorley et al., 2011). Due to the small diameter (0.63 cm) of the vial, it was initially assumed that sample self-attenuation was negligible. The sample self-attenuation could have also been estimated with MCNP6®, but given the relatively large uncertainties budgeted for other factors, such as the measured gradient in vertical dose rate of the irradiator, and the good agreement across the modalities, it was ultimately determined that the additional simulations would add little to the ultimate conclusions.

Nineteen aliquots of the irradiated, sensitized quartz were analyzed using OSL dosimetry. Aliquots of lab irradiated quartz were loaded into stainless steel cups and read using the SAR protocol shown in Table 5.1 modeled after the protocol used by Kadereit and Kreutzer (2015). In addition to performing the dose reconstruction on the lab irradiated quartz, dose reconstruction was performed on aliquots of calibration sand provided by the manufacturer with an estimated absorbed dose of the 4.81 Gy.

Table 5.1: SAR Protocol Setting for Calibration Quartz Dose Reconstructions.

Step	Description
Test Dose	Sr/Y exposure: 0 s, 400 s, 1000 s, 2000 s, 400 s
Preheat	20 s at 260°C
OSL	40 s, blue LED (90% power) at 125°C
Test Dose	Sr/Y exposure: 540 s
TL	220°C, no preheat
OSL	40 s, blue LED (90% power) at 125°C
Signal Reset	40 s, Blue LED (90% power) at 280°C

5.2.4 Risø TL/OSL Reader Internal Sr90/Y90 Dose Rate Comparison

The final component of this analysis was calculation of the dose rate of the internal $^{90}\text{Sr}/^{90}\text{Y}$ beta source of the Risø TL/OSL reader using EPR spectroscopy and the Landauer microStar-ii medical dosimetry unit. Eight alanine dosimeters were given approximate doses of 5 Gy using the Risø reader's internal beta source. In order to account for the effects of inhomogeneous dose deposition within the alanine pellets, seven of the pellets were sanded down to decrease their thicknesses. In this way, comparing the measured dose per mass of alanine pellets allowed for analysis of the dose deposition's spatial dependency within the pellet. Table 5.2 contains the thicknesses and masses of the alanine pellets.

Table 5.2: Thicknesses and Masses of the Alanine Dosimeters Used to Characterize the Dose Deposition in the Alanine Pellets Under Irradiation by the Risø Reader’s Internal Beta Source.

Dosimeter ID Number	Dosimeter Thickness (cm)	Dosimeter Mass (mg)
A001	2.67	58.35
A002	2.41	52.89
A003	2.22	47.95
A004	2.06	45.06
A005	1.84	39.73
A006	1.47	31.35
A007	1.19	24.08
A008	0.96	19.4

In order to measure the dose rate of the Risø reader’s internal beta source with the Landauer microStarII medical dosimetry unit, 11 nanoDot dosimeters were loaded onto stainless steel disks in the Risø TL/OSL reader. The nanoDots were given doses between 35 mGy and 1 Gy using the Risø reader’s internal beta source. Plotting the doses measured by the Landauer microStarII medical dosimetry unit versus the irradiation time allowed for measurement of the beta source’s dose rate for this configuration. The Landauer’s NIST calibration was provided by independently exposed calibration dosimeters provided by the vendor.

5.3 Results

5.3.1 Gammacell 220 Dose Rate Calibration

The values obtained from NIST for the doses delivered to each of the standard dosimeters are shown in Table 5.3. The dose values were reported in units of kGy to silicon. These units were chosen for this analysis because the main interest in this study was to determine the dose rate to quartz, which is composed primarily of silicon. As a result, the dose rate to silicon was the closest approximation of the dose rate to quartz.

Table 5.3: NIST Certified Doses Received from the Laboratory Gammacell 220, Uncertainties are 95%CL.

Vial Number	Mean Dose (^{60}Co kGy(Si), NIST)
0701	0.504±2.7%
0702	1.92±2.7%
0706	0.296±2.7%
0707	0.290±2.7%
0708	0.269±2.7%

For dosimeters 0706 and 0707, NIST reported the dose values as the mean of the dose to each of the four pellets. However, for dosimeter 0708 an absorbed-dose gradient was observed and as a result the dose to each alanine pellet was reported (the value in Table 5.3 represents the average of the four values reported for dosimeter 0708). Table 5.4 contains the absorbed doses to each of the four alanine pellets in dosimeter 0708.

Table 5.4: NIST Certified Dose to Each Alanine Pellet in Dosimeter 0708.

Relative Pellet Position	Dose (^{60}Co kGy Si)
1 (Top)	0.264±2.7%
2	0.267±2.7%
3	0.271±2.7%
4 (Bottom)	0.272±2.7%

The values in Table 5.4 indicated the potential presence of a dose gradient in the vertical direction of the laboratory's Gammacell. Nonuniformities in the dose field within the irradiator cavity of the Gammacell 200 are well documented in the literature (Rodrigues et al., 2009; Rodrigues et al., 2010; Hefne, 2000). It was thus concluded that the observed dose gradient was a factor that would have to be characterized and accounted for to ensure repeatability in future irradiations.

5.3.2 EPR Measurement of the Vertical Dose Profile

The EPR dose estimates made in-house confirmed the presence of a vertical dose gradient in the laboratory's Gammacell, as indicated by NIST (note, only NIST was allowed to measure their dosimeters). Using the measured dose rate gradient combined with the NIST dose values, it was possible to compute an optimized functional fit for the dose rate gradient along the vertical axis of the Gammacell's irradiation cavity. First, dose rate profiles were constructed using both the NIST measurements and the laboratory EPR measured dose values. Then a quadratic fit was performed on the laboratory measured dose rate profile. The fit parameters obtained for the laboratory measured dose rate profile were used to estimate the slope and curvature of the dose rate across the standard dosimeters 0706 and 0707, where only the mean doses across the four alanine pellets were reported by NIST. The doses to the individual alanine pellets in these NIST dosimeters were calculated using the dose rate profile's slope and curvature. Here, the average value of the 4 alanine pellets within each NIST dosimeter was normalized to maintain equality with the dosimeter's reported dose value. The magnitude of the laboratory measured doses were then proportionately scaled to give the same dose rates as the NIST calibration doses as shown in Figure 5.3. This process was iteratively repeated until successive iterations resulted in insignificant changes in the dose profile's fit parameters (i.e. four iterations).

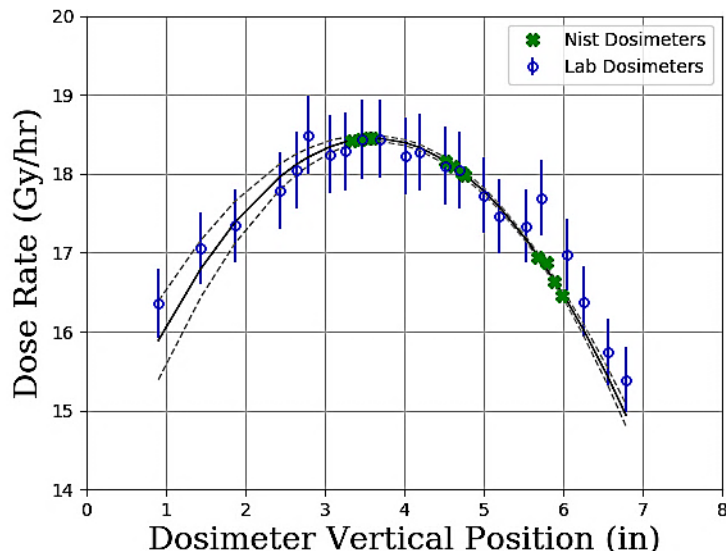


Figure 5.3: Dose rate as a function of vertical position within the GammaCell 220 irradiation chamber showing 95%CL with the dashed bands straddling the best fit.

Figure 5.3 shows the vertical dose rate profile measured by the in-house EPR system along with the dose rate values provided by NIST. For qualitative comparison an MCNP6® model of the Gammacell 220 irradiator was constructed. Table 5.5 contains the fit parameters for the dose rate profile along the central axis of the Gammacell 220’s irradiation chamber, assuming a quadratic functional form,

$$D \left(\frac{Gy}{h} \right) = ax^2 + bx + c. \quad (1)$$

Table 5.5: Fit Parameters Obtained for the Axial Dose Rate Distribution in the Gammacell 220.

Fit Parameter	Optimized Value
a	$-0.35 \pm 0.01 \text{ (Gy h}^{-1} \text{ cm}^{-2}\text{)}$
b	$2.5 \pm 0.1 \text{ (Gy h}^{-1} \text{ cm}^{-1}\text{)}$
c	$13.9 \pm 0.3 \text{ (Gy h-1)}$

A straightforward method to visualize statistical agreement between models and measurement is to compare the measurements to the model and its associated confidence interval. In Figure 5.3, the model for the irradiator’s dose rate profile (the best-fit line) is shown along with the 95% confidence bands for the model. The confidence bands were created using the standard “delta method” (Wolberg, 1992). For each independent variable in the model space, the distance of the confidence band from the line-of-best-fit, D , can be calculated as

$$D = \sqrt{J \cdot C \cdot J'} \sqrt{E/DF} \cdot T^{crit}. \quad (2)$$

In Equation (2), J contains the elements of the Jacobian matrix at the point of interest, C is the standard normalized covariance matrix, J' is the transpose of the Jacobian elements, E is the sum of the squared errors, DF is the degrees of freedom for the best fit line and T^{crit} is the critical t for the desired confidence level and number of degrees of freedom. We can then assume that measurements, with their associated uncertainties, that lie within the 95% confidence bands are in statistical agreement with the underlying fit to the data. Applying this statistical check to the lab measured EPR dosimeters, it can be seen that only one of the 21 dose rate measurements falls

outside of the 95% confidence region for the model derived from the NIST measured data values.

It was evident from Figure 5.3 that the agreement between the dose rate profile (black line) calculated with the NIST dosimeters and the measured doses to the lab dosimeters (empty circles) decreased with increasing distance from the center of the irradiator chamber. In order to characterize this disagreement, a least squares fit was performed on the lab measured dosimeters, assuming the functional form in Equation (1). Then the percent difference between the two dose rate functions was calculated as a function of the vertical position inside the irradiator chamber. It was found that the maximum percent difference between the two models was less than 5% and occurred towards the bottom or top of the irradiation chamber. Accordingly, within the central, 10 cm (approximately) of the irradiation chamber, the two dose rate models agreed within 1%. It was concluded that the observed dose rate disagreement should be considered as excess uncertainty in the dose rate of the irradiator and included in the overall uncertainty budget for future irradiations.

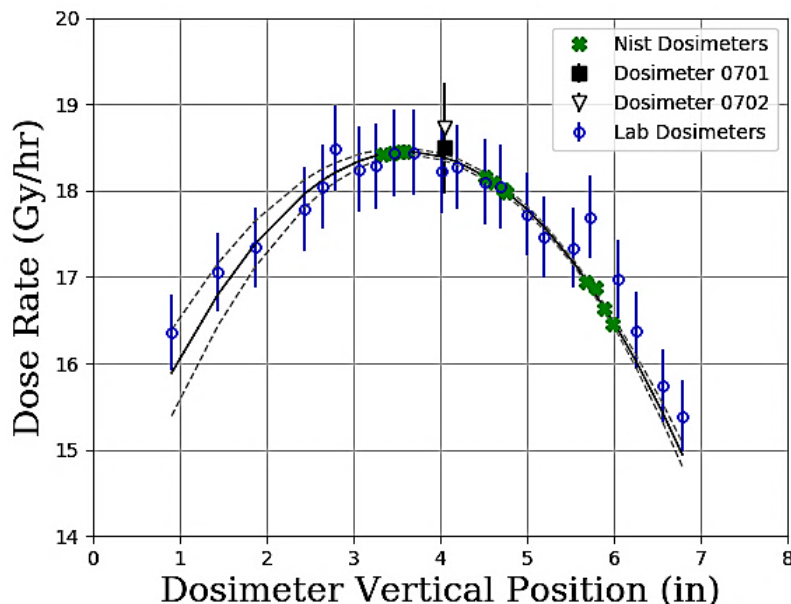


Figure 5.4: Dose rates for NIST dosimeters 0701 and 0702 (black square and triangle, respectively) plotted with the measured dose rate profile for the GC220.

A similar approach was applied to the two additional dosimeters that NIST analyzed, dosimeters 0701 and 0702. Figure 5.4 shows the dose rates determined for dosimeters 0701 and 0702, along with the other NIST dosimeter data and the derived model of the dose rate profile. An MCNP6® simulation was performed to determine the dose rate differences for alanine pellets

in the two different sample holders. Combining the effect of the different sample holders with the expected decrease in activity in the irradiator over the span of a month brought the dose rate estimates of dosimeters 0701 and 0702 into agreement with the measured dose rate profile of the Gammacell 220 as seen in Figure 5.4. It can be seen in Figure 5.4, that the dose rates measured for dosimeters 0701 and 0702 agreed with the measured dose rate profile to within the measurement uncertainty.

5.3.3 Calibration Quartz Exposure

Table 5.6 contains the dose rate to quartz estimates for the Risø's internal $^{90}\text{Sr}/^{90}\text{Y}$ beta source. These were obtained from both the Risø provided 4.81 Gy sensitized quartz and in-house Gammacell irradiated, sensitized quartz. The dose rate of the reader beta source calculated using the Risø-provided, calibration quartz agreed with the dose rate calculated using the lab-irradiated, sensitized quartz. The uncertainty in the dose rate of the Risø reader's internal beta source, determined using the lab irradiated quartz, was dominated by the assumed uncertainty in the dose rates over the length of the sampled positions shown in Figure 5.3.

Table 5.6: Dose Rate Estimates for the Risø TL/OSL Reader Sr-90/Y-90 Beta Source.

Sample	Dose Rate (Gy/s(quartz))
Risø-provided	0.0071 ± 0.0001
Lab-irradiated	0.0072 ± 0.0004

5.3.4 Inter-modality Comparison

Finally, the dose rates of the Risø TL/OSL unit's beta source was estimated using the Landauer microStarrii nanoDots and alanine pellets read on the Bruker EMXmicro. Table 5.7 contains the dose rate estimates for Risø TL/OSL unit beta source calculated with all three modalities.

Table 5.7: Dose Rate of the Risø Sr-90/Y-90 Source Measured with Three Separate Dosimetric Materials.

Dosimeter	Dose Rate Estimate (Gy/s(quartz))
Risø-provided quartz	0.0071±0.0001
Lab-irradiated quartz	0.0072±0.0004
microStarrii	0.0069±0.0001
EMXmicro	0.00708±0.00003

Figure 5.5 shows the doses (in Gy) measured by the Landauer nanoDot dosimeters plotted versus the applied exposure times in the Risø reader. The slope of that line was then taken to be the measured dose rate for the nanoDot OSLDs, as reported in Table 5.7. In addition, the uncertainty in the measured dose rate represents the uncertainty in the slope parameter (0.0001 Gy/s) from the linear regression. Table 5.8 contains the fit parameters from the linear least squares fit, along with the chi squared value for the fit. The intercept for the fit was calculated to be 9±8 mGy. It does not appear that accumulation of background radiation on the nanoDot OSLDs contributed any significant bias to the calculated dose rate. Although a small dose accumulation is expected on OSLDs due to background radiation exposure, each of the selected nanoDots was read for background contributions before irradiation in the Risø reader and background subtraction was applied (note a single read removes less than a few percent of total signal in a background read measurement).

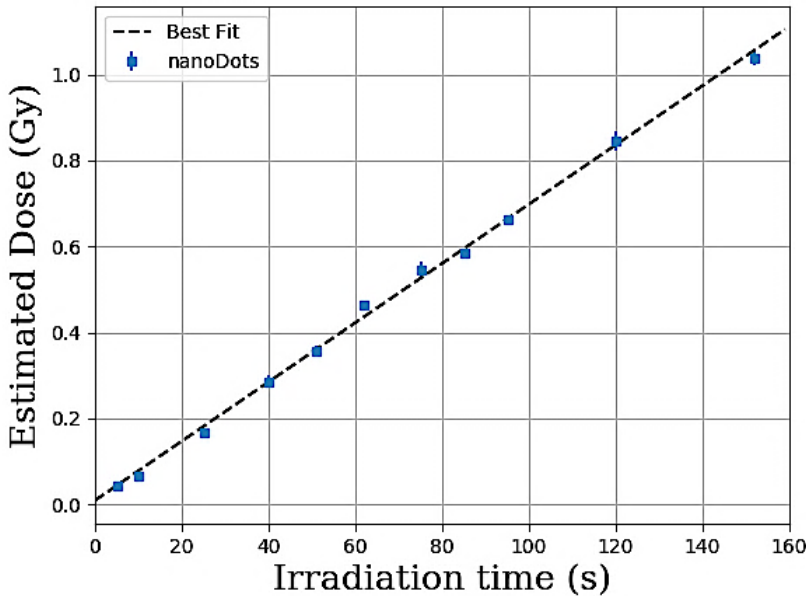


Figure 5.5: Doses measured using the InLight microStarri mediscal dosimetry unit. The associated pointwise uncertainties are the uncertainties in the dose estimates reported by the dosimetry unit. The fit was obtained by weighted linear regression.

Table 5.8: Fit Parameters Obtained for the Dose Rate of the Risø’s Beta Source Measured with nanoDot OSLDs.

Fit Parameter	Optimized Value
slope	0.0069 ± 0.0001 (Gy/s)
intercept	9 ± 8 (mGy)
χ^2	0.005

For the dose rate measurement using EPR dosimetry, it was first necessary to characterize the dose deposition in the alanine dosimeters from the Risø’s beta source. The internal beta source of the Risø reader is generally used to irradiate very thin ($90\text{-}250\ \mu\text{m}$) samples. As a result, the thickness of the alanine pellets represented a significant departure from the usual application of the Risø reader’s irradiation setup. The first step in this process was to determine what, if any, trend existed between the measured dose and the thickness of the dosimeter. Table 5.9 shows the measured doses and thicknesses for each of the 8 sampled dosimeters. The data shows a negative correlation between the dosimeter thickness and the measured dose. These data can be seen plotted in Figure 5.6.

Table 5.9: Doses Delivered to the Alanine Dosimeters Using the Risø Internal Beta Source, as Measured Using EPR.

Dosimeter ID Number	Dosimeter Thickness (cm)	Measured Dose (Gy)
A001	2.67	3.44 ± 0.09
A002	2.41	3.56 ± 0.09
A003	2.22	3.7 ± 0.1
A004	2.06	3.9 ± 0.1
A005	1.84	4.0 ± 0.1
A006	1.47	4.4 ± 0.1
A007	1.19	4.7 ± 0.1
A008	0.96	4.9 ± 0.1

The best fit line in Figure 5.6 was an exponential of the form

$$D(t) = m_1 e^{-m_2 t} + m_3, \quad (3)$$

where t was the thickness of the dosimeter and m_3 was the uncorrected native signal seen in alanine at low doses. Table 5.10 contains the fit parameters obtained for the dose deposition trend in the alanine dosimeters.

Table 5.10: Fit Parameters Obtained for the Dose-Dosimeter Thickness Relationship with Errors Given at the One Standard Deviation Level.

Fit Parameter	Optimized Value
m_1	4.8 ± 0.5 (Gy)
m_2	0.35 ± 0.09 (mm^{-1})
m_3	1.6 ± 0.7 (mGy)

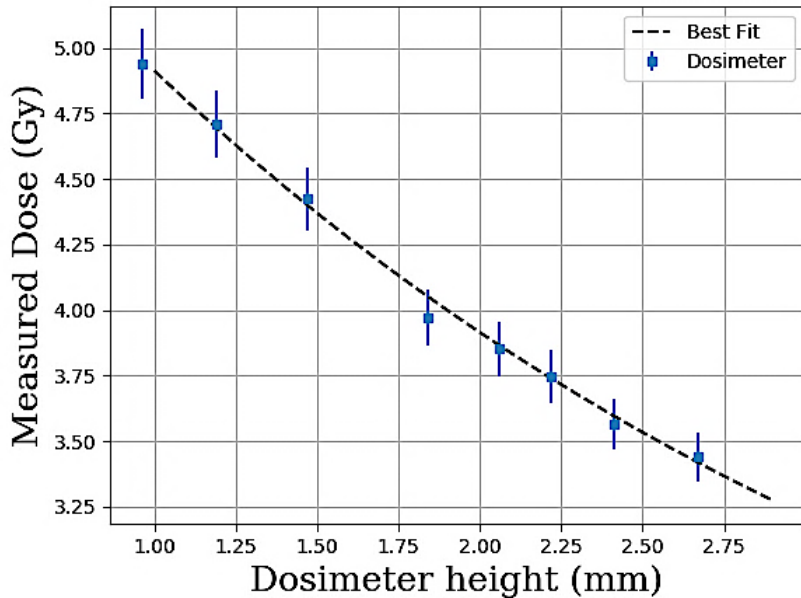


Figure 5.6: Measured dose delivered by the Risø's internal beta source versus the height (thickness) of the dosimeter. The line of best fit was assumed to follow a decaying exponential where its parameters were calculated using Levenberg-Marquardt fitting.

Given the observed dose-dosimeter thickness relationship, it was determined that the dose to the alanine dosimeters was not uniform throughout the thickness of the dosimeter. Since EPR dosimetry measures the average dose to the bulk dosimeter material, it was important to correct for the dose deposition profile within the alanine dosimeter administered by the Risø reader's beta field. Figure 5.7 shows the modeled geometry with the alanine pellet position below the beta source. The model was used to calculate the particle flux inside of the alanine pellet. A track-length estimate of the electron flux on a cylindrical mesh (FMESH4 tally) was applied to the model using MCNP6®. The mesh spacing used was 0.02 cm in the radial direction, 0.02 degrees in the azimuthal coordinates and 0.01 cm in the vertical direction. Figure 5.8 shows the simulated electron flux inside the alanine pellet. There were 3 characteristics of interest. First, there was a decrease in the flux with depth in the alanine pellet as expected. Second, the flux in the outermost annulus of the alanine pellet is greater than would be predicted by material attenuation within the material alone. This is likely due to backscattering of unattenuated electrons on the peripheral edges of the stainless-steel cup holding the pellet. The final feature of interest is that the flux in the layers closest to the stainless-steel cup are also elevated. This is likely the result of backscattered electrons off of the stainless-steel cup itself directly under the alanine pellet.

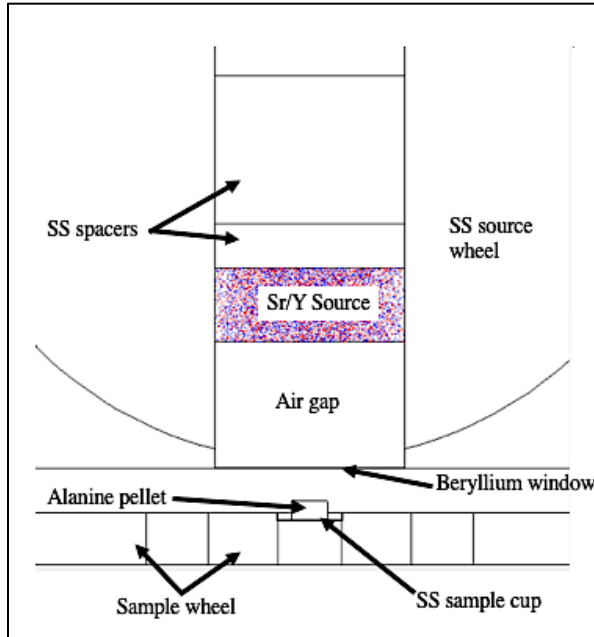


Figure 5.7: MCNP6® model geometry for the Risø reader internal beta source irradiations.

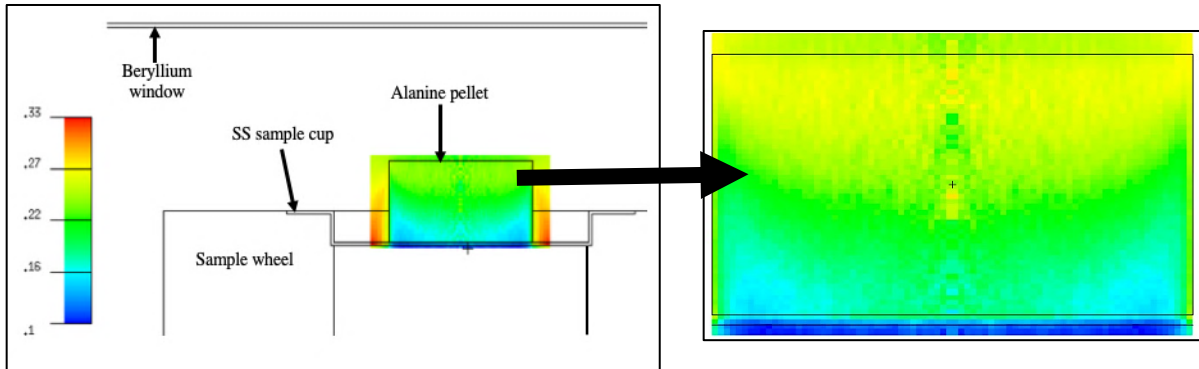


Figure 5.8: Electron flux (e/cm^2) within a single alanine pellet irradiated by the Risø's internal beta source. As expected, the simulations predicted a decrease in electron flux with depth into the alanine pellet. There also appears to be an increase in the electron flux in the pellet near the bottom and radial surfaces of the pellet.

The alanine pellet was segmented into 9 equal thickness slices and pulse height tallies, modified to provide energy deposition (*F8 tallies), were used to calculate the dose to each segment. The calculated dose deposited in each dosimeter segment was normalized to the top (closest to the source) segment and plotted in Figure 5.9. The data in Figure 5.9 were then fitted with a three-parameter decaying exponential function of the form of Equation (3).

Table 5.11: Fit Parameters Obtained for the Dose Rate Gradient Simulated Through the Depth of a Regular Alanine Pellet.

Fit Parameter	Optimized Value
m_1	0.97 ± 0.02 (Gy)
m_2	0.97 ± 0.08 (mm^{-1})
m_3	0.28 ± 0.02 (Gy)

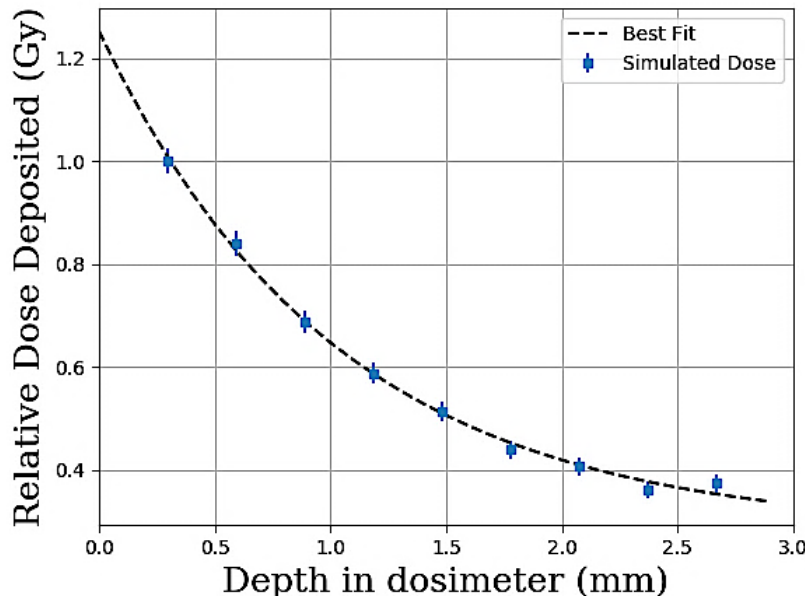


Figure 5.9: Relative dose deposition in the simulated alanine pellet calculated by MCNP6®. The best fit line was calculated for a three-parameter exponential decay function.

Table 5.11 contains the fit parameters for the line of best fit for the dose deposition profile in the alanine pellet. The relative dose deposition function was used to determine the correction factor for the dose delivered to the alanine pellet by the Risø reader. The correction factor was taken to be the average of the dose deposition function over the length of the alanine pellet. The corrected dose rate measured by EPR dosimetry is show in Table 5.7.

Finally, from each of the independent dose rate estimates for the Risø's internal beta source the correction factors for converting dose estimates between each of the modalities were calculated. Table 5.12 contains the calculated correction factors. The correction factors are tabulated such that if a dose, D_0 , were measured with one dosimetry system then a dose estimate, D' , from another system would be given by the multiplying D_0 with the associated correction factor.

Table 5.12: Correction Factors for Relating Dose Estimates Between the Three Dose Reconstruction Modalities.

	Risø	EPR*	microStar
Risø	1.00	1.02 ± 0.01	1.04 ± 0.01
EPR*	0.98 ± 0.01	1.00	1.03 ± 0.02
microStar	0.96 ± 0.01	0.97 ± 0.02	1.00

*The corrections applied to the EPR measurements in Section 5.3.4 were to account for EPR dosimetry measuring the absorbed dose to bulk material, whereas the Risø 90Sr/90Y source basically delivers an entrance dose. These corrections would not generally be necessary for comparing doses irradiated by other sources.

5.4 Conclusions

TL, OSL and EPR all have demonstrated utility in retrospective dosimetry studies. Such studies have broad application fields such as radiation effects, nonproliferation and accident response. This paper has demonstrated a technique for comparative analysis between multiple modalities for retrospective reconstruction of doses. The benefit of such analyses is that by combining multiple modalities, it is possible to turn nearly every ubiquitous object in the developed world into a dosimeter (O’Mara and Hayes, 2018; Hayes and Sholom, 2017; Hayes and O’Mara, 2019; Hayes, Hooper, O’Mara, 2019). Utilizing the multi-modal calibration technique could allow for large scale, retrospective dose mapping since the doses indicated by different modalities can now be accurately related back to one another.

Chapter 6

Grain Size and Density Separation Effects on Luminescence Dose Estimates Using Brick Material

This material was published as:

O'Mara RP, Hayes RB. Grain Size and Density Separation Effects on Luminescence Dose Estimates Using Brick Material. *Advances in Nonproliferation Technology and Policy Conference*, Orlando Fl, Nov 12-15, 201

This paper is published in the Transactions of the American Nuclear Society

6.1 Introduction

One of the fundamental roles in nonproliferation is the verification of any state's nuclear activities. A variety of instruments and techniques have been developed to facilitate the measurements that make verification possible. However, traditional measurement instruments suffer from the limitation that they require the operator to have access to the nuclear material of interest. Optically and thermally stimulated luminescence dosimetry has the potential to remove that requirement.

Recent efforts have shown that it is possible to retrospectively reconstruct doses and extract source energy information using optically and thermally stimulated luminescence (OSL/TL) from material extracted from bricks (O'Mara and Hayes, 2018; Chapter 4; Chapter 9). However, one of the major limitations of these luminescence techniques is that extensive sample preparation is generally required. In most cases, laborious steps are taken to isolate and purify grains of quartz from the rest of the constituent materials (Bøtter-Jensen and Murray, 2001). This is because quartz has been shown to be a reliable dosimetry material capable of reconstructing doses up to hundreds of Grays (Wintle and Adamiec, 2017).

After the sample preparation stage, samples are subjected to a dose reconstruction algorithm. The dose reconstruction algorithm matches the luminescence of the sample due to the environmental radiation dose to the luminescence that results from exposing the sample to a controlled, laboratory source for a given amount of time. By precisely knowing the dose rate of the laboratory radiation source, the environmental dose to the sample can be related to dose received from the laboratory source, or dose equivalent.

In quartz dosimetry, one of the prevailing dose reconstruction algorithms is the single aliquot regenerative (SAR) dose technique. In the SAR technique, after the natural luminescence of each subsample, or aliquot, is measured, the aliquots are each subjected to successive iterations of laboratory irradiation and luminescence signal measurement, to build a dose response curve. After each laboratory irradiation and measurement step, the luminescence signal from a small test dose is also measured. This additional step is meant to track the sensitivity change in the aliquots due to measurement protocol (Wintle and Murray, 2006).

In the traditional SAR protocol, in quartz, the signal of interest is the luminescence under blue light stimulation (Wintle and Murray, 2006). However, it has been demonstrated that dose reconstructions can be performed using other luminescence signals, such as the isothermal

thermoluminescence signal (Colarossi et al., 2015). Additionally, implementing the isothermal TL was recently used to reconstruct dose deposition profiles in bricks using minimally prepared samples, i.e. brick samples that had been separated by grain size only (O’Mara and Hayes, 2018; Chapter 4). However, the effect of additional treatment, e.g. density separation in addition to grain size separation, was not tested in the previous work.

The purpose of this study is to test the effect of sample preparation in a tradition SAR protocol using the blue light OSL signal and in a modified-SAR protocol using the isothermal TL signal. By comparing the dose estimates from each of the protocols on aliquots of different grain sizes and densities to Monte Carlo dose estimates, it will be possible to determine the adequacy of the dose reconstructions at different levels of sample treatment. Further, it will be possible to preliminarily identify the minimum level of sample treatment necessary for each dose reconstruction algorithm to perform adequately.

Unlike the process of risk estimation, epidemiological doses can be estimated from reconstructed doses to buildings as well as individuals’ personal items where sample preparation time is not a critical issue (Bailiff et al., 2016). However, in emergency response dosimetry, it is necessary to rapidly prepare dose estimates. As a result, the usual long accrual time for dose estimation may prevent the applicability of luminescence dosimetry techniques whenever rapid assays are sought. Along the same lines, developing dose reconstruction algorithms that do not require strenuous sample preparations represent progress towards acquiring the ability to perform luminescence dose measurements in the field.

6.2 Materials and Methods

Two common, red bricks purchased from a local hardware store were exposed to 100 mCi ^{241}Am source for three hours. A 1-inch cylindrical core was drilled from directly underneath the source’s location, perpendicular to the exposed surface of the brick. The cylindrical core was then sliced longitudinally into twelve, approximately 2-mm disks. Each disk was crushed and sieved into two aliquots grain size: less than 90 μm and 90-250 μm .

The subsamples from the two disks closest to the source, B3C1S1 and B3C1S2, were selected for further division by density separation. Material from each grain size aliquot was separated into 4 density ranges: <3 g/cc, 3-2.7 g/cc, 2.7-2.65 g/cc and 2.65-2.5 g/cc. Quartz densities typically fall within the range of 2.6-2.66 g/cc, while feldspars generally have lower

densities. The density ranges were chosen primarily to separate the quartzes from the feldspars because feldspars have been shown to exhibit anomalous fading (Wintle, 1973). The sample aliquots obtained from each core slice can be found in Table 6.1.

Table 6.1. Aliquot Grain Size and Densities Obtained from Each Sample.

Grain Size	<90 μm	90-250 μm
>3 g/cc	None	B3C1S2 [†]
3-2.7 g/cc	Both	Both
2.7-2.65 g/cc	Both	Both
2.65-2.5 g/cc	Both	Both
<2.5 g/cc	Both	Both

[†]Only obtained enough sample for a single aliquot test

As can be seen in Table 6.1, each slice did produce every grain size and density combination below 3 g/cc. This resulted from the small total amount of material obtained from each core slice. During the analysis, some of the aliquots failed the statistical checks for the performance of the reconstruction algorithm. An aliquot failing to meet the statistical checks was considered as not optimal for the corresponding dose reconstruction algorithm.

In order to test the effect of sample preparation on the dose estimates for the brick material, a conventional SAR, using the blue light OSL signal, protocol was performed on each of samples. A modified-SAR using the isothermal TL signal (ITL-SAR) was also performed on each aliquot for comparison. The steps employed in each of the dose reconstruction protocols can be found in Appendix A.

The expected doses to the two selected core layers were also estimate using the Monte Carlo particle transport code MCNP6® (Goorley et al., 2011). The specifications of the calculations were also described in Chapter 4 (O’Mara and Hayes, 2017). The simulated brick material composition was taken to be that of standard red brick, with a density equal to the measured density of the core removed from the brick (McConn Jr, 2011). In addition to the dose estimates a parameter perturbation study was performed using MCNP’s *pstudy* module (Brown et al., 2004). The associated uncertainty estimates were reported at the $1-\sigma$ level from the dose distributions calculated by randomly sampling many of the nominal parameters in the simulation (e.g. source position, brick density, brick composition, etc.).

6.3 Results

One criterion that can be used to judge the dosimetric value of a particular sample of brick material is the percentage of aliquots that yield a useable signal or that pass specified statistical checks and demonstrate expected functional dependencies. The assessment of the signals' usability was based on two statistical tests: the recycling ratio test and recuperation tests, described elsewhere as part of the SAR protocol (Wintle and Murray, 2006). Table 6.2 contains the percentage of aliquots that passed the statistical tests for each grain size and each dose reconstruction algorithm for grains from sample 1. Table 6.3 contains the percentage of aliquots that passed the statistical tests for each grain size and each dose reconstruction algorithm for grains from sample 2.

As expected, for the conventional SAR protocol (labeled SAR in Table 6.2 and Table 6.3) a higher proportion of useful aliquots come from samples in density ranges closer to the density range for feldspars and quartz (approximately 3-2.5 g/cc). In contrast, for the modified SAR protocol (labeled ITL-SAR in Table 6.2 and Table 6.3) the correlation between density and the proportion of useable aliquots is less pronounced. In particular, for the <90 µm aliquots from slice 2 100% of the aliquots with densities less than 2.5 g/cc produced useable signals.

Table 6.2: Percentage of Useable Dose Estimates, by Size, Density and Protocol, for Sample B3C1S1.

Density	<90 µm		90-250 µm	
	SAR	ITL-SAR	SAR	ITL-SAR
>3 g/cc	-	-	-	-
3-2.7 g/cc	100%	-	0% [†]	33%
2.7-2.65 g/cc	67%	-	100%	67%
2.65-2.5 g/cc	75%	-	50%	0%
<2.5 g/cc	50%	-	67%	100%

-Sample volume was too small to yield an aliquot for the associated test.

[†]All tests failed although a small sample was obtained.

Table 6.3: Percentage of Useable Dose Estimates, by Size, Density and Protocol, for Sample B3C1S2.

	<90 μm		90-250 μm	
<i>Density</i>	<i>SAR</i>	<i>ITL-SAR</i>	<i>SAR</i>	<i>ITL-SAR</i>
>3 g/cc	-	-	0% [†]	-
3-2.7 g/cc	67%	33%	25%	100%
2.7-2.65 g/cc	67%	0%	50%	67%
2.65-2.5 g/cc	100%	33%	67%	67%
<2.5 g/cc	67%	100%	33%	33%

-Sample volume was too small to yield an aliquot for the associated test

[†]All tests failed although a small sample was obtained.

A second important criterion by which the dosimetric value of a particular sample is how well the sample performs in reconstructing a given dose. The doses predicted using MCNP6® for B3C1S1 and B3C1S2 were 2.2 ± 0.7 Gy and 1.4 ± 0.4 Gy, respectively. Table 6.4 and Table 6.5 contain the reconstructed doses for B3C1S1 and B3C1S2, respectively. Each dose estimate was taken to be the weighted mean of the dose estimates for the aliquots of that subgroup.

Table 6.4: Dose Estimates in Gy, by Size, Density and Protocol, for Sample B3C1S1.

	<90 μm		90-250 μm	
<i>Density</i>	<i>SAR</i>	<i>ITL-SAR</i>	<i>SAR</i>	<i>ITL-SAR</i>
3-2.7 g/cc	1.3 ± 0.2	-	-	1.0 ± 0.4
2.7-2.65 g/cc	1.16 ± 0.08	-	1.5 ± 0.4	1.45 ± 0.1
2.65-2.5 g/cc	0.88 ± 0.06	-	0.87 ± 0.07	1.0 ± 0.7
<2.5 g/cc	0.87 ± 0.09	-	0.88 ± 0.09	1.9 ± 0.5

-Aliquot did not yield any “useable” dose estimates.

Table 6.5: Dose Estimates in Gy, by Size, Density and Protocol, for Sample B3C1S2.

Density	<90 μm		90-250 μm	
	SAR	ITL-SAR	SAR	ITL-SAR
3-2.7 g/cc	1.4±0.8	0.7±0.5	0.2±0.3	0.9±0.2
2.7-2.65 g/cc	0.5±0.6	N/A*	1.0±0.3	0.7±0.1
2.65-2.5 g/cc	0.52± 0.08	0.54± 0.09	0.7±0.1	0.70±0.02
<2.5 g/cc	0.52± 0.09	0.7±0.3	0.39± 0.08	0.74±0.02

*Aliquot did not yield any “useable” dose estimates.

It can be seen from the data in Table 6.4 and Table 6.5 that the reconstructed doses universally underestimate the predicted dose. Another feature that should be noted is that the uncertainties reported in Table 6.4 and Table 6.5 are the standard deviations of the dose estimates that passed the statistical tests. The relatively large standard deviations are indicative of the large spread in the individual dose estimates. This characteristic could indicate that a larger number of aliquots should be averaged to improve the dose estimates

Another feature of interest that can be seen in the data from sample B3C1S1 is that the higher density grains, across both grain sizes and both dose reconstruction protocols, yielded dose estimates closer to the predicted dose (2.2±0.7 Gy). A similar trend is also present, to a lesser extent, in the dose estimates for B3C1S2. This result is promising, because it was expected that these higher density grains were primarily composed of the zircons and quartz

6.4 Discussion

Much of the historical research on luminescence (TL and OSL) dose reconstruction with earthen materials relates to dating of archeological artifacts (Wintle and Adamiec, 2017). These same technologies can be, and have been, applied to dose reconstruction problems in the fields of nuclear nonproliferation and emergency response. However, some limitations in archeological dating are not of concern for nonproliferation or emergency response applications and vice versa. For example, in archeological dating applications, feldspars are sometimes regarded as problematic due to anomalous fading. Whereas for nonproliferation-related applications, anomalous fading is not of concern and, as a result, feldspars may be more attractive than quartz, if they exhibit comparable or greater sensitivity, or luminescence emission per unit dose. In order

to expand the applicability of luminescence dosimetry for nuclear applications, much of the conventional wisdom in the field should be reassessed to account for the disparate challenges between the applications.

This paper seeks to provide preliminary information that will help to define the minimum amount of sample preparation needed to obtain adequate results for nonproliferation or emergency response applications. This type of analysis is important because nonproliferation and emergency response situations are likely to be time sensitive. In nonproliferation applications, two problems of particular interest are source localization and energy discrimination. For both of these problems, one may be willing to sacrifice accuracy in absolute dose determination for increased dose resolvability, or sensitivity. This is because uncertainties in absolute dose determination, for nonproliferation problems, relate to a source's activity or dwell time in a particular location whereas dose resolution affects the energy or spatial resolution of these techniques.

One of the main questions that remains following the present study is how the number of grains in each aliquot might affect the grain-size-density relationships found herein. Throughout this analysis, aliquot sizes were generally on the order of 30 individual grains, or less. It has been suggested in the literature that, even in samples where a prescribed quartz isolation routine has been applied, only on the order of 5% of grains yield useful dosimetric TL or OSL signals (Li et al, 2016). As a result, the utilization of relatively small aliquots, such as those employed in this analysis, may decrease the sensitivity causing an increase in the detection limit. As a result, future studies are planned to perform a similar analysis with larger aliquots (more grains), and more aliquots, in order to more completely assess the statistical distributions of grains of dosimetric value for retrospective dosimetry.

Another question, relevant to nonproliferation and emergency response problems, is the minimum detection limit for a given sample. In dating applications, there is a greater interest in the upper dose limit since the size of the dose scales with the age of the sample. In contrast, typically a dose that would be of interest in nonproliferation situations can credibly be comparable to background. As a result, a logical extension of the present study would be to test the above findings at lower dose levels. O'Mara and Hayes used untreated, non-density separated, brick material in the less than 90 μm diameter range to reconstruct doses down to

hundreds of mGy (O’Mara and Hayes, 2018). Future efforts will be directed towards assessing whether density separation can extend this dose range to lower doses.

6.5 APPENDIX A: DETAILED DESCRIPTION OF DOSE RECONSTRUCTION PROTOCOLS

Table 6.6: Outline of the Conventional Single Aliquot Protocol Used for TL and OSL Dose Measurements.

	Description
Step 1	Dose (β source exposure, 0s for natural dose)
Step 2	“Preheat” (TL at 260°C for 10 s)
Step 3	Blue stimulated luminescence (40 s at 125°C) [†]
Step 4	Test dose (β source exposure for 300 s)
Step 5	“Cut heat” (TL at 220°C for 0 s)
Step 6	Infrared stimulated luminescence (40 s at 220°C)

[†] Signal component used for final dose reconstruction.

Table 6.6 contains the in-house, conventional SAR protocol used in this experiment. The protocol is very similar to the standard, adapted from (Wintle and Murray, 2006), with the exception that the sample’s luminescence is also recorded during the preheat and cut heat steps (steps 2 and 6).

Table 6.7: Outline of The Modified Single Aliquot Protocol Used for TL and OSL Dose Measurements.

	Description
Step 1	Dose (β source exposure, 0 s for natural dose)
Step 2	“Preheat” (TL at 260°C for 10 s)
Step 3	Infrared stimulated luminescence (40 s at 220°C)
Step 4	Pulsed optically stimulated luminescence (250 μ s total, 50 μ s on, 50 μ s off)
Step 5	Test dose (β source exposure for 300 s)
Step 6	“Preheat” (TL at 260°C for 10 s)
Step 7	Infrared stimulated luminescence (40 s at 220°C)
Step 8	Pulsed optically stimulated luminescence (250 μ s, 50 μ s on, 50 μ s off)

[†] Signal component used for final dose reconstruction

Table 6.7 contains the modified-SAR protocol used in this analysis. The protocol was designed to maximize the amount of data collected in each step. A similar protocol was used by Colarossi et al. (2015) to reconstruct doses in feldspar contaminated quartz samples

Chapter 7

Monte Carlo Analysis of Optimally Selected Dose Points for the Additive Dose Method for Retrospective Dosimetry

This material was published as:

O'Mara, R.P. and Hayes, R.B. "Monte Carlo Analysis of Optimally Selected Dose Points for the Additive Dose Method for Retrospective Dosimetry." *Trans. Amer. Nuc. Soc.* 121:1223-1226 (2019)

This paper is published in the Transactions of the American Nuclear Society

7.1 Introduction

Solid-state dosimetry commonly involves interpolation of a measured electronic response to an unknown radiation dose after sequential administrations of known laboratory doses. In the ideal case, such samples would display a linear response to these additive irradiations. When linearity in the response is observed, then linear least squares methods are well suited for dose estimation via extrapolation. Here, a material whose dosimetric signal increases with dose can be subject to laboratory additive doses to back extrapolate to the equivalent dose the sample had when it came into the laboratory. The question of how to optimize laboratory additive doses has been looked at elsewhere (Hayes et al., 1997).

An example of the additive dose process is shown in Figure 7.1. Note the extrapolation back to the x -intercept is required to obtain the dose estimate of the sample corresponding to the reconstructed dose estimate. This is a contrived example but shows the basic principle with reconstructing historical doses when the dose response has a known functional shape (such as linear). Errors were selected to be an ad-hoc combination of constant and relative components for this example. Basically, a material will have its dosimetric signal measured and then additive doses are applied to aliquots to construct its overall response function.

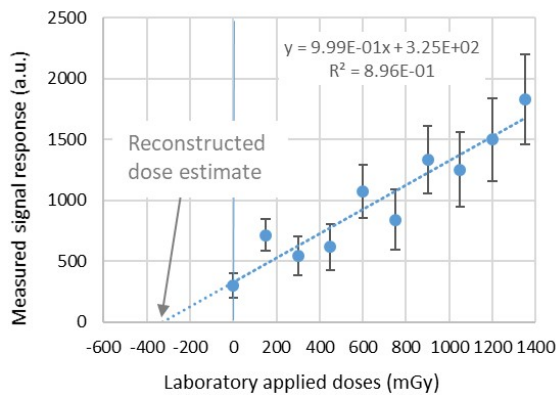


Figure 7.1. Contrived example of a dose reconstruction as would be utilized in solid-state dosimetry methods for estimating historical exposures to insulator materials.

It has been shown previously that the errors in dose reconstructions made by least squares methods are strongly dependent on the distribution of additive dose points. The question asked was whether the additive doses could be spaced in a more optimized fashion rather than constant spacing as seen in Figure 7.1. The goal is to minimize the projected error back on the abscissa so as to obtain the most precise estimate without compromising any accuracy (Hayes et al., 1997).

One simplification is to note that when the errors in individual dose points can be approximated as constant, that is when the relative errors are negligible, then expected error in a dose estimation can be easily approximated prior to performing the experiment (Hayes et al., 1997).

A mathematical approach for optimal additive dose distribution was proposed in Hayes et al. (1997). This approach was based on a closed-form equation derived maximum likelihood estimate error in the x-intercept term for a linear fit to given additive dose distributions. Notably, the authors found that the intercept error was minimized when: (a) additive dose points were more concentrated at zero added dose, and (b) when dose points were placed only at the extrema of the dose distribution, i.e. at zero dose and some pre-determined maximum dose (Hayes et al., 1997). While these findings allowed the authors to make useful suggestions for optimal additive dose point distributions, no attempt was made to verify the theoretical consideration. The present study sought to confirm, by Monte Carlo analysis, the theory originally developed in Hayes et al. (1997).

This work also seeks to generalize the recommendations made by Hayes et al. (1997) to account for nonlinear responses to additive doses. Although many commonly utilized dosimetric materials, such as quartz, alanine, aquatic shells and bone, have linear dose responses up to very high doses, there may be times where nonlinear dose responses are encountered. In general, dose responses can be approximated as one or more superposed saturating exponential functions. The saturating behavior of the dose responses for solid-state dosimetry materials are characterized by the material specific charge trapping parameters. As such, it is important to address such nonlinear behaviors when considering solid-state dosimetry using fortuitous materials (Grün, 1996).

7.2 Materials and Methods

In order to assess the validity of the claims made in Hayes et al. (1997), a Monte Carlo analysis was designed in accordance with the assumptions made in Hayes et al. (1997) (linear responses, known error types, zero bias from other confounding contributors). The assumed response and applied fitting functions were taken to be a simple linear form. The slope of the response function and the maximum additive dose point were taken to be constants, while the intercept was varied as a percentage of the maximum additive dose point. Both a relative error term and a constant error term were added to the dose responses before applying the fit function

(comparable to Figure 7.1). The Monte Carlo analysis consisted of randomly sampling these error terms applied to the additive dose points. The dose was then reconstructed from the least squares fit parameters to the additive dose points. The distributions of additive dose points were then chosen to replicate the distributions in the original analysis (Hayes et al, 1997).

7.2.1 Nonlinear Responses

In order to analyze the behavior of the uncertainty in x-intercept estimates when the response is nonlinear, a saturating exponential function of the form

$$f(x) = m_1(1 - e^{-m_2(x-m_3)}) \quad (1)$$

was taken to be the underlying dose response function. This was used to generate the simulated measurements at each dose point. In Equation (1), the parameters m_1 and m_2 are essentially shape parameters (e.g., m_1 is the maximum amplitude of the response at infinity) and were taken as constants during the generation of the underlying dose response function (all three parameters in Equation (1) were solved for normally during the fitting of Equation (1) to the simulated dose measurements). In a realistic measurement scenario, the m_2 and m_3 parameters are intrinsically related to sample specific characteristics, e.g. lattice defect type and number density, and are likely to vary widely between different materials. However, varying those parameters here would add little generality to this analysis since the absolute magnitude of the maximum amplitude and exponential rate of the equation are unimportant, insofar as the function is sublinear over the range of the dose points.

When doses are small compared to the saturation dose of m_2^{-1} , the response in Equation (1) can accurately be approximated by a linear function (Grün, 1996). Here, additive irradiations will not be able to resolve curvature from the saturation behavior until the maximum applied dose is sufficiently large with errors sufficiently low to distinguish any sublinearity due to the saturation effect. To ensure that range additive dose points included the nonlinearity of the underlying response function, the x-intercept, and thereby dose estimate (m_3), was varied as a percentage of the maximum additive dose point. Fig. 2 shows the effect of varying the m_3 parameter on the x-intercept, while holding m_1 and m_2 constant.

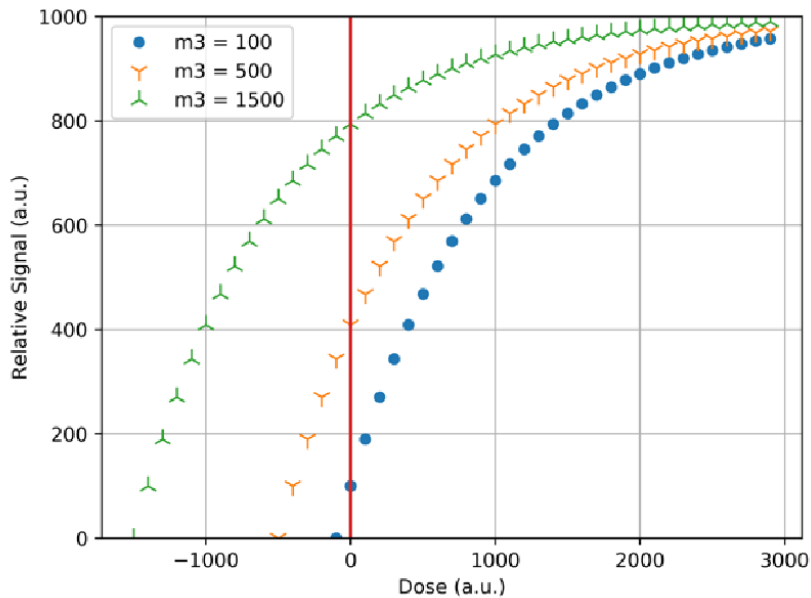


Figure 7.2: Effect of the m_3 parameter in Equation 1 on the x-intercept of the dose response. It can be seen that varying m_3 essentially shifts the entire dose response function, and thus x-intercept, by the value of m_3 .

It can be seen in Figure 7.2 that varying m_3 shifts the entire functional form of Equation (1) but has no effect on the overall shape of the function. Figure 7.2 also illustrates for small m_3 (the natural dose) relative to m_1 and m_2 , how the dose response to additive irradiations appears approximately linear near the abscissa. It has been shown that in this low dose range, a linear dose response model provides reasonably accurate dose estimates. However, as the m_3 parameter grows, so does the response function's departure from linearity.

In addition to the responses calculated using Equation (1), both a relative error term and a constant error term were folded into the simulated measurement values. The relative error terms were simulated as a random number generated from a normal distribution multiplied by the magnitude of the simulated response. The constant error term was chosen to be small relative to the expected responses, however constant errors had little bearing on the analysis that was performed. Similar to the procedure performed in Hayes et al. (1997), for the nonlinear response and fit functions, the estimated error in the x -intercept was calculated as a function of its relative magnitude compared to the maximum dose point. Unlike the case for a linear fit function, since Equation (1) has 3 unknown parameters, the extreme values dose point distributions (e.g. single high/low point distributions) could not be used. In other words, using only two additive dose points was not sufficient to solve for all three unknowns in Equation (1). Levenberg-Marquardt

least squares was used for all fits, and the error in the x -intercept was calculated from the covariance matrix term for the m_3 parameter.

7.3 Results

For the linear response and linear fit case, the number of dose points was set at 10 per fit and the maximum additive dose point was set to 1000 a.u. (arbitrary units). For each distribution, a total of 1000 Monte Carlo runs were performed, after which the calculated relative errors in the x -intercept were all averaged. Figure 7.3 shows the mean relative error in the x -intercept as a function of the size of the x -intercept relative to the maximum dose point.

The nomenclature used here was as follows; HnH was half of all measurements at the zero dose and half at a single high dose, Const is a fixed dose distance for each measurement as seen in Figure 7.1, SHP is where all the measurements were at the zero dose with only one single high point measurement at the maximum dose, Log used a logarithmic distribution effectively bunching additive doses closer to the maximum dose while alternatively the Linear grouping simply increased additive doses linearly with each step effectively giving some concentration of measurements near the intercept. Any of these distributions could in principle be used in practice. It is immediately evident from the data in Figure 7.3 that beyond the point where the x -intercept (X_{int}) is 10% of the maximum dose point, of the tested distributions, the half-and-half distribution yields the lowest relative errors in the x -intercept. Similar to the results found in Hayes et al. (1997), it was found here that for the linear case, the distributions that only had points at the extreme values had consistently lower propagated error than the others.

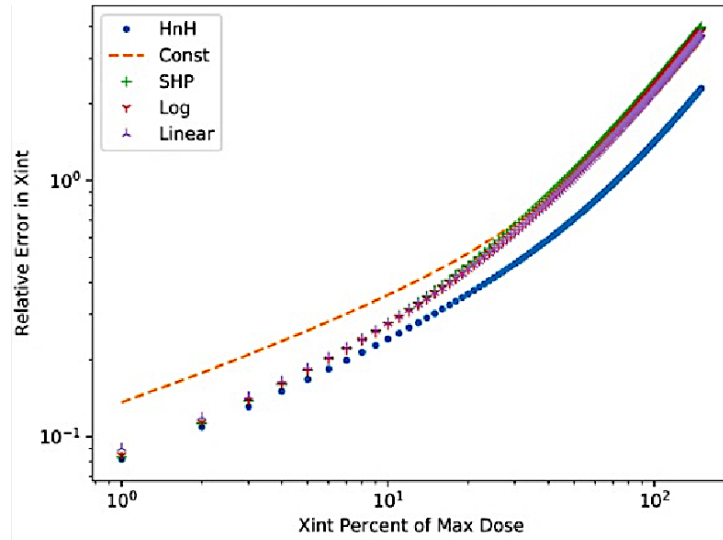


Figure 7.3: Relative error in the x -intercept as a function of the x -intercept's percent of the maximum dose point for the half-and-half (HnH) distribution, constant distribution (Const), single high point distribution (SHP), logarithmic distribution (Log) and linear distribution.

After confirming the finding that the extreme value distributions resulted in the lowest relative x -intercept errors, it was shown that the number of dose points placed at the maximum is functionally dependent on the on the x -intercept's percentage of the maximum additive dose. Figure 7.4 shows the calculated dependence of high point placement on the relative size of the x -intercept compared to the maximum dose point. No attempt to smooth out the Monte Carlo results was done here. Note also that only linear responses are being considered at this point.

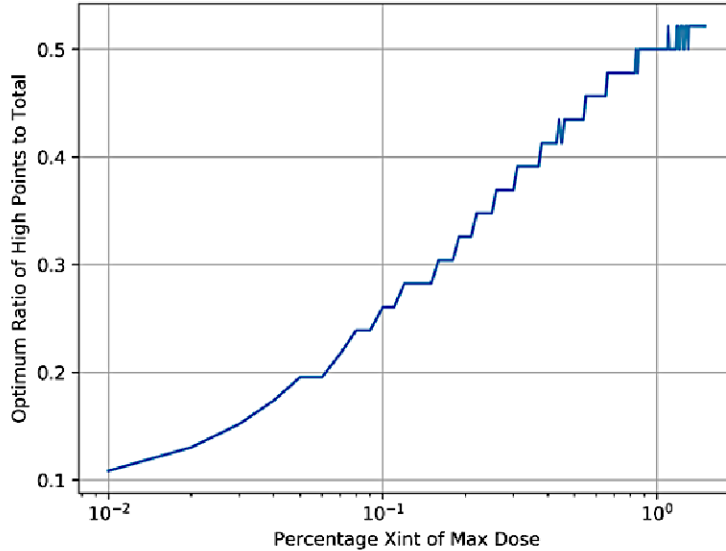


Figure 7.4: Optimum number of high dose points as a function of the size of the x -intercept relative to the maximum additive dose point.

From Figure 7.4 it can be seen that the optimum number of dose points at the maximum dose point is dependent on the relative size of the x -intercept with respect to the maximum dose point. Similar to the findings from Hayes et al. (1997), it appears as though the optimum percentage of dose points placed at the maximum dose point occurs at 50%. In other words, it will in general always be advantageous to group more measurements near the zero but if a long extrapolation is required, up to 50% of the measurements can be placed at the highest dose point.

7.3.1 Nonlinear Responses

For the nonlinear response and fit case, again the number of dose points was initially set to 10 with a maximum dose point of 1000 a.u. (arbitrary units). For each of the tested distributions a total of 1000 Monte Carlo runs were performed and the average relative errors in the x -intercept were plotted versus the x -intercept as a percentage of the maximum dose point (Figure 7.5).

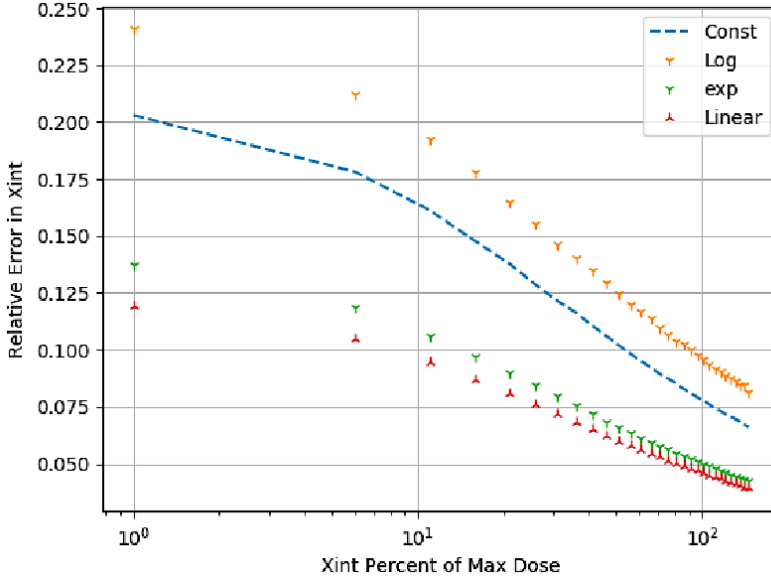


Figure 7.5: Relative error in the x -intercept as a function of the x -intercept's percent of the maximum dose point for the constant distribution (Const), logarithmic distribution (Log), exponential distribution (exp), and linear distribution.

Figure 7.5 shows the relative error in the x -intercept as a function of the x -intercept as a percent of the maximum dose point for the three best performing distributions. It can also be seen that contrary to the behavior observed for the linear case, in non-linear reconstructions, the relative error in the x -intercept decreases as the relative size of the x -intercept relative to the maximum dose point increases. This reflects the need to obtain the correct curvature in the saturating exponential sufficient to extrapolate appropriately to the x -intercept m_3 .

Figure 7.6 shows the relationship between the number of dose points and the relative error in the x -intercept for a linear distribution of dose points. As expected, the relative x -intercept error decreases non-linearly with an increasing number of dose points. For the linear distribution, the multiplicative factor between successive dose points was defined as

$$m = \left(\frac{\phi}{\tau}\right)^{\frac{1}{N-1}}, \quad (2)$$

where N was the number of dose points (10), ϕ was the maximum dose point (1000) and τ was the first non-zero additive dose point, such that the dose delivered to each point after the zero-dose point was simply the previous dose point multiplied by m .

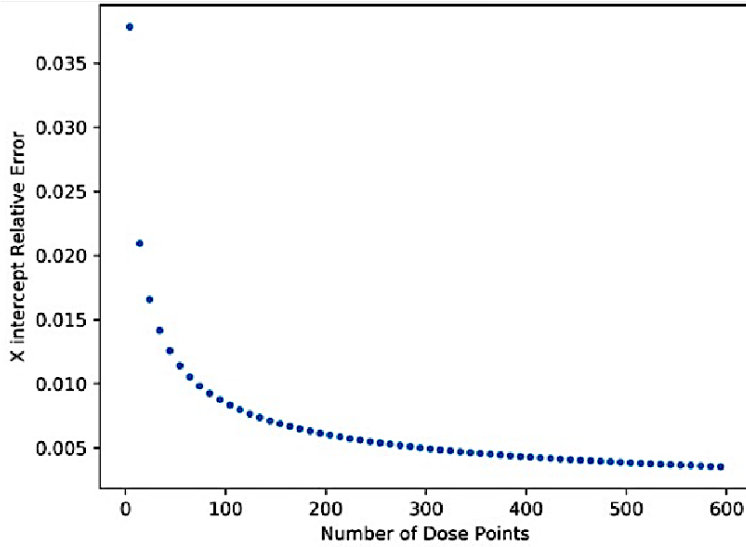


Figure 7.6: Relative error in the x -intercept as a function of the number of dose points in the fitted distribution.

In Figure 7.7, the relative x -intercept error is plotted as a function of the dose point step size (N). It can be seen from this figure that the relative x -intercept error decreases nonlinearly as the multiplicative factor increases.

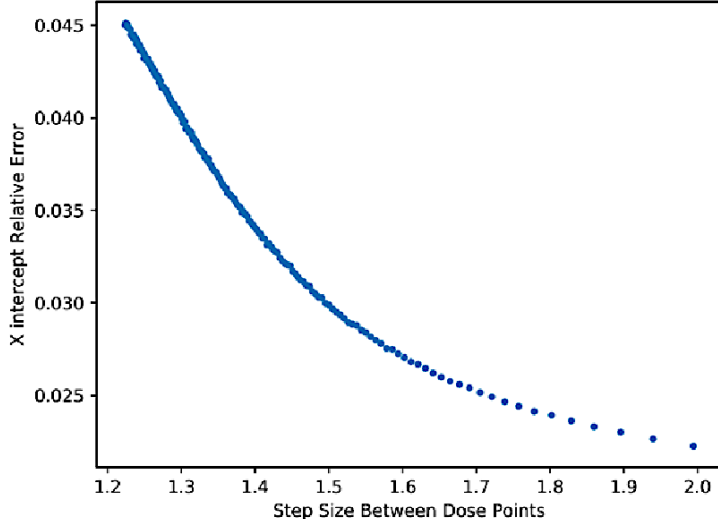


Figure 7.7: Relative error in the x -intercept as a function of the multiplicative step-size between dose points.

Increasing the multiplicative factor, m , functionally places relatively more additive dose points near the zero-dose point and fewer towards the maximum dose point. This indicates that the dose points of greatest importance for nonlinear fits are those at the lower additive doses, as

was found with linear functions. Likewise, the optimum distribution requires some knowledge of these various parameters relative to the material of interest.

7.4 Conclusions

In this work, a Monte Carlo approach was used to confirm the theoretical optimal distributions (Hayes et al., 1997) for additive dose solid-state dosimetry, when the response to those additive doses is linear. The results from this analysis agreed with the main findings presented in Hayes et. al (1996): (a) for a linear response the optimum additive dose distribution will have dose points only at zero and at the maximum; (b) for a given choice of maximum applied dose, the number of dose points placed at that maximum should increase for larger estimated initial dose (as brought into the lab, see Figure 7.1); and (c) the total number of dose points measured can be used to tune the desired relative error in the x -intercept.

Additionally, this work applied a similar treatment for cases where the assumption of a linear response function can no longer be used. Preliminary recommendations for minimizing the x -intercept error in such cases can be made based on these findings. First, utilize a linear distribution of dose points between zero and the chosen maximum added dose. Second, select the multiplicative step size to yield the desired uncertainty and time constraints. Third, if still smaller uncertainties are desired, the number of dose points can be increased.

Finally, there are two avenues of future work being identified on this topic. First, the uncertainties discussed herein only refer to the uncertainties inherent to the fit protocol but do not necessarily indicate closeness of the estimate to the true intercept. Future numerical treatments should test these dose distributions for their ability to reconstruct the true, underlying x -intercept. In other words, is there any inherent bias which is not normal that can be introduced or enhanced with a given distributions of additive dose points. A second area of interest is characterizing the functional distribution of the intercept errors (are they distributed normally, or not). Computing the distributions of the intercept errors will give additional insight into the uncertainty budget for additive dose dosimetric estimates.

Chapter 8

Radionuclide Assay of Brick Material Using a High Purity Germanium Detector and Low-level Detection Facilities

This material was submitted as:

O'Mara RP, Hayes RB. Radionuclide Assay of Brick Material Using a High Purity Germanium Detector and Low-level Detection Facilities. *J. Environ. Rad.* 2019. (Submitted)

8.1 Introduction

In many parts of the world, construction products are often composed of earthen materials in the form of wood, silicates and minerals such as gypsum or flyash. Such products can be expected to have elemental concentrations reflective of the geographical locations from which they were collected. Building materials such as granite, concrete, bricks, gypsum and cement have been identified as potential sources of public gamma radiation exposure because they contain radionuclides such as ^{238}U , ^{40}K and ^{232}Th (CDC, 2018). For these reasons alone, interest exists for methods of quantifying the expected dose rates to occupants of dwellings built from these materials.

In addition to the radionuclides present in building materials derived from earthen components (rocks and soil), there are mineral crystals, such as quartz, which can be used to measure radiation doses using luminescence techniques. This becomes particularly useful when the materials have had their dosimetric signal zeroed due to sintering as in the case of brick and tile. Luminescence dosimetry with quartzes extracted from building materials, such as roofing tiles, has even been used to reconstruct doses to atomic bomb survivors (Fujita et. al., 2006; Ichikawa et al., 1987). Quartz from bricks has similarly been used to measure integrated dose to residents downwind of the Nevada Test Site (Haskell et al., 1994) and residents of Chelyabinsk (Bougrov et al., 1998). Quartz is also quite often used in dating applications such as pottery and aeolian sands¹ (McKeever, 1985) where the age is approximately the integrated dose divided by the ambient dose rate.

Recent novel applications using bricks has demonstrated how dose depth profile measurements can provide energy discrimination information of an incident radiation field (O'Mara and Hayes, 2018; see Chapter 4). Even surface mount resistors which are ubiquitous in all modern electronics (thumb drives, watches, key fobs etc.) have been shown to be capable of reconstructing background doses due to environmental sources (Hayes and O'Mara, 2019). These dosimetric studies can also be important in determining doses received by the public in the

¹ Here, the dosimetric signal is zeroed by the bleaching effects of sunlight so the accrued dose to buried aeolian sands divided by the ambient dose rate is an estimate of their age in terms of how long ago they were buried.

wake of a nuclear accident or as a means to detect illicit nuclear activities. (Bailiff et al., 2016; Hayes et al., 2019).

Luminescence dosimetry consists of measuring subtle electronic changes in materials that result from radiation interactions with insulator materials. The measured signal is the light output, luminescence, from the material in response to optical or thermal stimulation (Yukihara and McKeever, 2011). As with any radiation quantification approach, the detection limit is a function of the background and total uncertainty; knowing these for a long signal acquisition period could become a very important factor in some instances. A very simple estimate for the detection limit L_D would be $L_D = 1.645(\sigma_B + \sigma_L)$ where 1.645 is the critical t value for the 95% confidence level, σ_B is the uncertainty in the background contribution and σ_L is the uncertainty of the measurement right at the detection limit L_D where it is assumed the background average has been removed from the assay (NIST, 1994). How to obtain this background average in luminescence dosimetry is therefore of interest.

In order for anthropogenic doses in building materials to be detectable by luminescence dosimetry, the dose delivered by anthropogenic sources must be large relative to the total dose accrued over the lifetime of the material due to naturally occurring sources of radiation (i.e., the natural background dose) in the immediate environment. The rate at which the background dose to a material grows will be dependent not only on the amount of naturally occurring radioactive materials (NORM) in the local environment around the material, but also on the total activity of all radionuclides inside the material itself. Furthermore, this can be spatially dependent in the material due to lack of buildup contributions near a surface, as radiation emanates out from the material. As a result, if the activity concentrations of the radionuclides in a given building material and the environmental radiation field can be measured, then the detection limit for the anthropogenic radiation dose can be estimated based on the age of the building and as a function of position in the material.

A general framework for computing activity concentrations from bricks using gamma spectra collected with a portable high purity germanium (HPGe) detector has been demonstrated elsewhere (O’Mara and Hayes, 2018b). In O’Mara and Hayes (2018b), a forward transport simulation was performed in order to estimate the energy efficiency of the detector system to a set of photon energies representative of background NORM. A separate transport calculation was performed to calculate the expected attenuation of the background photon spectrum due to a

brick placed in front of the detector crystal, assuming the brick contained no radionuclides. Then any increase in the difference between spectra measured with and without a brick in front of the detector was attributed to contributions from radionuclides in the brick. Ultimately it was found that with a nominally short integration time and intrinsic detector efficiency, at best, such an analysis could only be used to determine the maximum amount of radionuclide that could be present and still be undetectable.

8.1.1 A New Energy Efficiency Methodology

One potential shortcoming of the previous analysis was that it relied on the simplification that a single energy calibration, calculated for the background spectrum, was sufficient for both measured spectra (with and without the brick). In reality, however, the energy efficiencies for a background gamma source could be quite different for a source distributed within a brick sample even if the two source terms have the same energy distribution. As a result, the efficiency for each photon energy E_i must be known when the shield is in place for both the NORM components in the shield and those from the background portion penetrating the shield.

Let the energy dependent contribution from external NORM have an efficiency ε_i^{NORM} which can be approximated by simulating a source uniformly distributed on a sphere centered on the detector enclosing the shield where each photon is initially directed exactly at the center of the detector. This same model could allow estimating the efficiency of the NORM components in the shield itself ε_i^{shield} by replacing the external source with a uniformly distributed source only in the shield itself with an isotropic source direction distribution.

The measured shielded count rate (CR_i^{meas}) for a photon with energy, E_i , is then the sum of the contributions from the radionuclides in the shield itself (CR_i^{shield}) and the contributions from the shielded background photons ($CR_i^{NORM(shielded)}$):

$$CR_i^{meas} = CR_i^{shield} + CR_i^{NORM(shielded)}. \quad (1)$$

The photon generation rate (PGR) from the shield itself at each energy, E_i , would then be PGR_i^{shield} and those from the external NORM would be $PGR_i^{NORM(shielded)}$. With this, the total measured count rate for the shielded detector, CR_i^{meas} , at each energy E_i is then given by

$$CR_i^{meas} = \varepsilon_i^{shield} PGR_i^{shield} + \varepsilon_i^{NORM(shielded)} PGR_i^{NORM(shielded)}. \quad (2)$$

Here, $\varepsilon_i^{NORM(shielded)}$ is the energy dependent efficiency for photons from the external NORM with the shield in place and ε_i^{shield} is the energy dependent efficiency for photons born in the shield itself. From Equation (2), the goal is to isolate the photon generation rate of the shield (PGR_i^{shield}). The $PGR_i^{NORM(shielded)}$ term can then be calculated from the measured count rates from the unshielded detector ($CR_i^{NORM(unshielded)}$) configuration, divided by the energy efficiency for the unshielded configuration,

$$PGR_i^{NORM(shielded)} = \frac{CR_i^{NORM(unshielded)}}{\varepsilon_i^{NORM(unshielded)}}, \quad (3)$$

and the energy efficiency for the shielded NORM ($\varepsilon_i^{NORM(shielded)}$) is also calculated from forward transport simulations. Solving for the photon generation rate of the shield (PGR_i^{shield}) then gives

$$PGR_i^{shield} = \frac{CR_i^{meas} - \frac{\varepsilon_i^{NORM(shielded)}}{\varepsilon_i^{NORM(unshielded)}} CR_i^{NORM(unshielded)}}{\varepsilon_i^{shield}}, \quad (4)$$

where all efficiency factors (ε_i^X) can be calculated by a forward transport calculation and each of the count rates is obtained directly from the measured spectra.

The activity in the shield however requires utilizing the actual photon branching ratio (B_i) for each energy. From this, the activity corresponding to a single isotopic emission in the shield A_i^{shield} is then found as $A_i^{shield} = \frac{PGR_i^{shield}}{B_i}$ which will then allow the assays from the portable HPGe (Figure 8.1) to be compared across different measurement modalities.

In the current study, samples of brick were subjected to gamma ray measurements at two metrology laboratories having reduced environmental background levels. The high precision measurements acquired from these facilities will be compared to the results from the portable HPGe measurements following the methodology described above. This would then allow for an

estimate of how well such HPGe activity concentration measurements could be performed in-situ. Finally, the activity concentrations provided by the low-level counting experiments will be used to characterize the internal dose rates inside of a simulated individual brick and that of a wall by Monte Carlo transport to provide the spatially dependent dose distribution which is typically not considered in luminescent dosimetry studies.

8.2 Description of Measurements

8.2.1 Low-level Counting Experiments

A standard red brick was purchased from a local hardware store in Raleigh, North Carolina. A 6.99-cm diameter cylindrical core was removed from the brick, perpendicular to the long axis of the brick. The resultant core was radially sliced into two cylindrical disks, one with a thickness of 4.45 cm (sample LB) and another with a thickness of 0.95 cm (sample SB). Both samples were prepared in Raleigh North Carolina and then packaged and shipped to the Ciambrone Radiochemistry Laboratory (USAF CIL) at Patrick Air Force Base. The reported mass of samples LB and SB were 370.6 g and 96.4 g, respectively.

Three gamma ray detectors were used to make the gamma spectrum measurements. Two of the detectors were located at CIL (G23 and G30) and the third (H1) was located at the Harkins Laboratory complex. Detector G23 was a p-type coaxial HPGe detector with a relative efficiency of 70% coupled with a 4" standard lead shield. Detector G30 was 50% relative efficiency, n-type, Compton suppressed, coaxial HPGe detector, also with a 4" standard lead shield. Detector H1 was a p-type coaxial HPGe with 120% relative efficiency designed to have very low background. In addition, the measurements made with detector H1 were performed with an equivalent of 610 m of granite overburden.

The Canberra ISOCS Software was used to determine the detector/sample specific efficiency curves for each of the low-level counting measurements. After this, Genie2k was used to analyze the spectra and compute the activity concentrations and uncertainties. A 10% systematic uncertainty factor was incorporated into the uncertainty budget as an estimate of systematic measurement uncertainties. This contribution was therefore incorporated into the total uncertainty calculated for the individual measured activity concentrations. The reported measurement dwell times were 5000 minutes for the H1 measurement, 5600 minutes for G23

and 5800 minutes for G30. The G23 and G30 measurements were made on 3 January 2019 and 7 January 2019. The measurement made with H1 was performed on 1 February 2019.

8.2.2 In-situ Laboratory Measurements

The in-situ gamma spectra from bricks were measured using an Ortec microDetective high-purity germanium (HPGe) detector. In order to minimize the impact of the background gamma field within the laboratory, standard red bricks were arranged in a mated enclosure around the crystal of the germanium crystal of the detector. Figure 8.1 shows the arrangement of the bricks and detector attempting to give the detector an almost 4π view of the brick material.



Figure 8.1: Experimental setup with the brick shield in place. Shown are the bricks (in black plastic bags) surrounding the germanium crystal of the detector.

MCNP6[®] was used for all forward transport calculations needed to determine the energy-dependent efficiency factors in Equation (4), $(\varepsilon_i^{shield}, \varepsilon_i^{NORM(unshielded)} \text{ and } \varepsilon_i^{NORM(shielded)})$ (Goorley et al., 2011). The detector geometry was created using measurements made from high resolution x-ray images of an Ortec microDetective HPGe detector. The geometry and model validation for the HPGe detector were discussed in (Hayes, 2016). The brick shield was modeled as a 20.53-cm by 19.06-cm by 21.23-cm cube composed of standard red brick material, with a density of 2.3 g/cm³ (McConn Jr., 2011). Although variations in the true density and mineral composition between the real and model bricks can be expected, for photon transport

calculations such as these the experimental uncertainties should vastly outweigh any computational biases.

For both sets of simulations used to determine the NORM efficiencies (shielded and unshielded), the background source was uniformly distributed on the surface of a 300-cm radius sphere and centered on the detector crystal. The energy distribution of the background source was simulated by 37 photon energies between 46.5 keV and 2.614 MeV (Wallace, 2013). The efficiency of this background source was calculated both with and without the brick shield. The efficiency factor for gamma rays borne in the shield itself was calculated for a source with the same energy distribution, only uniformly distributed within the shield (brick enclosure) itself.

Radionuclide analysis from the measured gamma spectra was performed using the Maestro® software package by Ortec®. In order to maintain consistency between the laboratory measurements and the low-level counting experiments, the same gamma library used by the labs that performed the low-level counting measurements was used for the in-laboratory HPGe measurement analysis.

8.2.3 Dose Rate Calculation Description

The primary question being explored was the spatially dependent average annual dose rate inside a general brick as a function of position for the internal radionuclides present (assumed homogenously distributed). The general strategy then was to determine the radionuclide concentrations in the brick, and then to use Monte Carlo transport simulations to calculate dose profiles in the brick material. All photon dose calculations were carried out using the SCALE code package (Rearden and Jessee, 2016). The measured brick was also modeled as a 24-cm by 7-cm by 11.2-cm cuboid composed of standard composition brick material (McConn, 2011). The standard recommended density of 2.3 g/cm^3 was used for the simulated brick.

The Origen module in SCALE was used to determine the photon, beta and alpha source terms of the brick material based on the measured activity concentrations. It was assumed that the activity concentrations of each of the brick samples were representative of the brick as a whole. The reported activity concentrations were used as the radionuclide concentrations inputs into Origen. The gamma source energies were calculated for 300 linearly distributed bins between 10 eV and 10 MeV, the beta source energies were calculated for 300 linearly distributed bins between 10 eV and 5 MeV and the alpha source energies were calculated for 300 linearly

distributed bins between 10 eV and 20 MeV. The final source strengths were scaled by the ratio of the sample mass to the total mass of the brick from which the samples were collected. All other library settings were left in the default mode for generation of the source spectra.

The photon transport calculations were then carried out using the Mavric module in SCALE. Mavric is a general-purpose Monte Carlo particle transport code that can accept direct source energy distributions generated by Origen. The photon fluxes were tallied using a track-length tally applied to a mesh on the problem geometry. For the single brick case, a 2-mm cubic mesh was used, and for the simulated wall a 24-cm by 7-cm by 11.2-cm mesh was used. For this analysis, all simulations were run in continuous energy mode. For each simulation 40,000 particles were simulated per batch and 20 batches were computed per simulation. These settings were sufficient to bring the relative uncertainties in the photon fluxes below 1.0%. The Henderson conversion factors (MT 9502) were used to convert the calculated fluxes into dose rates (Rearden and Jessee, 2016). The Henderson conversion factors provide dose rates in rad/hr which were then converted to mGy/yr since luminescence dosimetry doses are generally measured in Gy.

8.3 Measurement Results

8.3.1 Low-level Counting Experiments

A total of 18 radionuclide activity concentrations were contained in the final measurement report. Table 8.1-Table 8.3 contain the estimated activity concentrations for the total gamma field measured by each of the three low-level counting systems discussed in Section 8.2.1. Also included in these tables are the detection limits (critical level (L_c) and minimum detectable activity (MDA)) for each isotope and detection suite. Isotopes for which an “N/A” appears in the “Activity” column are those which could not be identified. The full report of the activity concentrations for all of the radionuclides can be found in Appendix A.1.

Table 8.1: Detection Limits and Isotope Activity Concentrations Measured on Detector G23.

Nuclide Name	Lc (Bq /Samp)	MDA (Bq /Samp)	Activity (Bq /Samp)	Act Unc (Bq /Samp)
^{40}K	2.34×10^{-1}	4.72×10^{-1}	2.24×10^2	3.21×10^1
^{137}Cs	3.11×10^{-2}	6.25×10^{-2}	N/A	N/A
^{223}Ra	1.61×10^{-1}	3.24×10^{-1}	N/A	N/A
^{231}Th	4.27×10^{-1}	8.56×10^{-1}	N/A	N/A
^{228}Th	2.37	4.75	1.95×10^1	5.13
^{212}Bi	4.27×10^{-1}	8.59×10^{-1}	1.40×10^2	1.87
^{228}Ac	8.71×10^{-2}	1.76×10^{-1}	1.36×10^1	1.55
^{224}Ra	5.34×10^{-1}	1.07	1.35×10^1	2.50
^{212}Pb	5.38×10^{-2}	1.08×10^{-1}	1.26×10^1	1.96
$^{234\text{m}}\text{Pa}$	3.13	6.31	1.24×10^1	2.27
^{234}Th	6.74×10^{-1}	1.35	9.10	2.32
^{214}Bi	6.37×10^{-2}	1.28×10^{-1}	7.77	8.98×10^{-1}
^{214}Pb	7.22×10^{-2}	1.45×10^{-1}	7.76	1.11
^{226}Ra	6.26×10^{-1}	1.26	7.63	2.55
^{210}Pb	3.31	6.64	7.62	2.16
^{208}Tl	2.46×10^{-2}	5.02×10^{-2}	5.04	6.72×10^{-1}
^{227}Th	1.82×10^{-1}	3.66×10^{-1}	5.00×10^{-1}	1.14×10^{-1}
^{235}U	4.00×10^{-2}	8.03×10^{-2}	4.68×10^{-1}	1.24×10^{-1}

Table 8.2: Detection Limits and Isotope Activity Concentrations Measured on Detector G30.

Nuclide Name	Lc (Bq /Samp)	MDA (Bq /Samp)	Activity (Bq /Samp)	Act Unc (Bq /Samp)
^{40}K	1.10×10^{-1}	2.24×10^{-1}	60.5	8.68
^{137}Cs	1.15×10^{-2}	2.33×10^{-2}	N/A	N/A
$^{234\text{m}}\text{PA}$	1.36	2.75	5.10	9.46×10^{-1}
^{212}Bi	1.63×10^{-1}	3.30×10^{-1}	4.07	5.90×10^{-1}
^{224}Ra	1.50×10^{-1}	3.03×10^{-1}	3.83	7.11×10^{-1}
^{228}Th	6.61×10^{-1}	1.33	3.65	1.33
^{228}Ac	4.36×10^{-2}	8.83×10^{-2}	3.64	4.24×10^{-1}
^{212}Pb	1.67×10^{-2}	3.35×10^{-2}	3.37	5.20×10^{-1}
^{234}Th	1.37×10^{-1}	2.75×10^{-1}	2.40	6.07×10^{-1}
^{214}Bi	2.56×10^{-2}	5.17×10^{-2}	2.15	2.56×10^{-1}
^{214}Pb	2.46×10^{-2}	4.96×10^{-2}	2.11	3.04×10^{-1}
^{210}Pb	2.61×10^{-1}	5.24×10^{-1}	1.88	4.77×10^{-1}
^{208}Tl	8.15×10^{-3}	1.70×10^{-2}	1.36	1.85×10^{-1}
^{231}Th	1.19×10^{-1}	2.39×10^{-1}	7.55×10^{-1}	3.04×10^{-1}
^{226}Ra	2.24×10^{-1}	4.51×10^{-1}	6.28×10^{-1}	5.41×10^{-1}
^{235}U	1.43×10^{-2}	2.88×10^{-2}	1.90×10^{-1}	4.15×10^{-2}
^{223}Ra	5.86×10^{-2}	1.18×10^{-1}	1.33×10^{-1}	6.40×10^{-2}
^{227}Th	4.66×10^{-2}	9.39×10^{-2}	1.26×10^{-1}	3.15×10^{-2}

Table 8.3: Detection Limits and Isotope Activity Concentrations Measured on Detector H1.

Nuclide Name	Lc (Bq /Samp)	MDA (Bq /Samp)	Activity (Bq /Samp)	Act Unc (Bq /Samp)
^{40}K	1.73×10^{-1}	3.52×10^{-1}	2.00×10^2	28.7
^{137}Cs	2.89×10^{-2}	5.83×10^{-2}	N/A	N/A
^{210}Pb	62.4	1.26×10^2	N/A	N/A
^{227}Th	3.73×10^{-1}	7.51×10^{-1}	N/A	N/A
^{231}Th	1.03	2.06	N/A	N/A
^{212}Bi	3.82×10^{-1}	7.71×10^{-1}	11.4	1.50
^{228}Ac	9.06×10^{-2}	1.83×10^{-1}	11.2	1.26
^{212}Pb	6.01×10^{-2}	1.21×10^{-1}	11.1	1.52
$^{234\text{m}}\text{Pa}$	3.43	6.93	7.78	1.61
^{214}Pb	7.69×10^{-2}	1.55×10^{-1}	6.74	9.14×10^{-1}
^{214}Bi	6.16×10^{-2}	1.24×10^{-1}	6.58	7.61×10^{-1}
^{228}Th	5.67	11.4	6.21	3.63
^{224}Ra	5.78×10^{-1}	1.16	6.13	1.66
^{234}Th	1.28	2.58	5.86	2.04
^{208}Tl	1.03×10^{-2}	2.15×10^{-2}	4.22	5.53×10^{-1}
^{226}Ra	9.73×10^{-1}	1.95	1.83	4.37
^{235}U	6.21×10^{-2}	1.25×10^{-1}	6.83×10^{-1}	3.32×10^{-1}
^{223}Ra	2.00×10^{-1}	4.02×10^{-1}	3.23×10^{-1}	1.49×10^{-1}

With the total isotopic activities measured on each of the three low-level counting detector systems, the specific activities of the samples can be determined. For a sample of mass m , containing I radioisotopes with activities A_i , the specific activity, SA , of the sample is given by

$$SA = \frac{\sum_{i=1}^I A_i}{m}. \quad (5)$$

The specific activities calculated by applying Equation (5) to the measured isotopic activities in Table 8.1-Table 8.3 are shown in Table 8.4. It can be seen from the values in Table 8.4, that the G30 detector calculated the highest specific activity for the small brick sample (SB).

Correspondingly, Detector G30 also detected the largest number of radioisotopes. An uncertainty weighted average of all results (assuming isotropic source terms) gave a specific activity estimate of $0.85 \pm 0.08 \text{ Bq g}^{-1}$.

Table 8.4: Specific Activities Determined by Each of the Three Detection Suites.

Detector	Specific Activity (Bq/g)
G23	0.9 ± 0.2
G30	1.0 ± 0.2
H1	0.8 ± 0.1

8.3.2 Laboratory Measurements

Table 8.5 contains the radioisotopes detected using the small microDetective HPGe spectra measurements. The net isotope activities were calculated by the methodology described in Section 8.1.1 and are shown in Table 8.5 as the total activity in the entire shield.

Table 8.5: Isotope Activity Concentrations Measured on the microDetective HPGe.

Isotope	Net Activity (Bq/shield)
^{40}K	7534 ± 14
^{212}Bi	2217 ± 1875
^{214}Pb	943 ± 225
^{226}Ra	1080 ± 25
^{228}Ac	570 ± 170
^{212}Pb	358 ± 2
$^{234\text{m}}\text{Pa}$	352 ± 70
^{214}Bi	344 ± 80
^{208}Tl	170 ± 11
^{223}Ra	75 ± 13
^{235}U	21 ± 7

The total mass of the brick enclosure was 15.20 ± 0.05 kg. Applying Equation (1), the estimated gross specific activity of the brick tent using the microDetective HPGe detector was 0.90 ± 0.1 Bq g⁻¹. Comparing the brick shield specific activity to those in Table 8.4 it can be seen that the microDetective HPGe measurements with corrected gamma ray efficiencies effectively estimate the radionuclide concentrations in the brick shield. Still, the HPGe only detected approximately 60% of the total number of radionuclides identified by the low-level counting experiments. While the new methodology presented here is able to correct for efficiency between the background and brick signals, it in no way improves the resolution of the detection system in the low energy range due to the buildup of the Compton continuum during the in-situ assay. As a result, the portable HPGe measurements miss those radionuclides with low energy gamma signatures (e.g. ^{232}Th).

8.3.3 Dose Rate Simulation Results

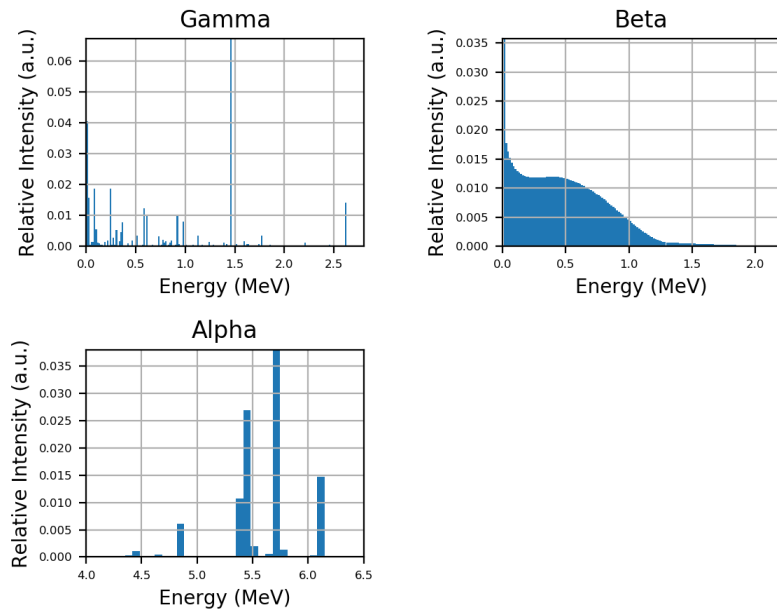


Figure 8.2: Origen calculated gamma, beta and alpha spectra (in arbitrary units, a.u.) based on brick sample activity concentrations measured by detector G30. The G30 measurements were made using a 96.40-g brick sample having a total volume of 36.50 cm³.

Figure 8.2 shows the expected particle source spectra inside the brick sample, determined by Origen for the isotopic activity concentrations estimated using the G30 detector. The radionuclides from the G30 detector measurements were selected because these constituted the largest number of radioisotopes. Based on the methodology described in Section 8.2.3, the annual, volume averaged absorbed dose rate from photons in the simulated brick was calculated to be 1.524 ± 0.003 mGy/yr. In an effort to quantify the relative contributions of beta and alpha particles to the annual dose rate within the brick material, three addition particle transport calculations were performed in MCNP6®, one for each particle type (photons, betas and alphas). In each transport calculation, the energy deposition, in MeV/g, was calculated with a track-length tally of energy deposition (F6 tally) for the appropriate source particle type. Table 8.6 contains the source strength terms (in particles per second per gram of brick material (p/s/g)), calculated by Origen, and the expected energy deposition relative to the photon dose deposition.

Table 8.6: Total Internal Dose Rate Contributions for Photons, Beta Particles and Alpha Particles.

Detector	Source strength (p/s/g)	Relative energy deposition
Photon	0.68719	1.00
Beta	0.75237	8.55
Alpha	0.10353	2.44

Based on the results in Table 8.6, the total annual, internal energy deposition rate contribution from beta particles is nearly nine times greater than that of photons, while the contribution from alpha particles is more than double. In a practical sense, the dose contribution from alpha particles can be approximated as negligible since the range of alpha particles in quartz is approximately 20 μm and has a substantially smaller luminescence signal emitted per dose absorbed (Aitken, 1985). As a result, the energy deposited from alpha particle emissions will be nearly all contained either within the mineral grains that contain alpha emitting inclusions or very near surfaces of neighboring grains. A similar argument applies to the beta dose rate although beta transport gives the same luminescent signal per dose as photons, unlike that from alphas.

Potassium is a common inclusion found in feldspar grains, while traditionally it is the quartz grains within a building material sample that are selected for dosimetry. Since beta particles have a shorter range than photons, the true relative beta dose rate to the dosimetric (quartz) grains is likely less than that predicted by this model. A 2007 study showed that for sand-sized grains in sediment samples from 4000 geographic locations, beta emissions from ^{40}K accounted for between 27 and 62% of the total dose rate (ignoring contributions from alpha emissions) to quartz grains (Ankjærgaard and Murray, 2007). Based on the transport simulation data in Table 8.6, the energy deposition contribution of beta particles was predicted to be nearly 90%, despite the model calculating the dose rate to the total material matrix (not to the quartz grains specifically).

It was not expected that the dose rate in the brick would be uniformly distributed throughout the brick volume. Specifically, when you approach the brick face, the source term is only on one side of that surface so that edge dose rates should approach around half that at the center (a quarter at an edge etc.), all depending on the size of the brick and energy of the photons. In other words, the source term on the face of a brick has half the source term than in

the middle due to the air having only an extremely low radon progeny concentration. To confirm, the dose rate within the brick was calculated on an approximately 2-mm cubic grid. Figure 8.3 shows the resultant calculated internal dose rate ranges for the brick. Here it can be seen that for an isolated brick, the internal dose rate is consistently lower on all faces and substantially lower on the corners.

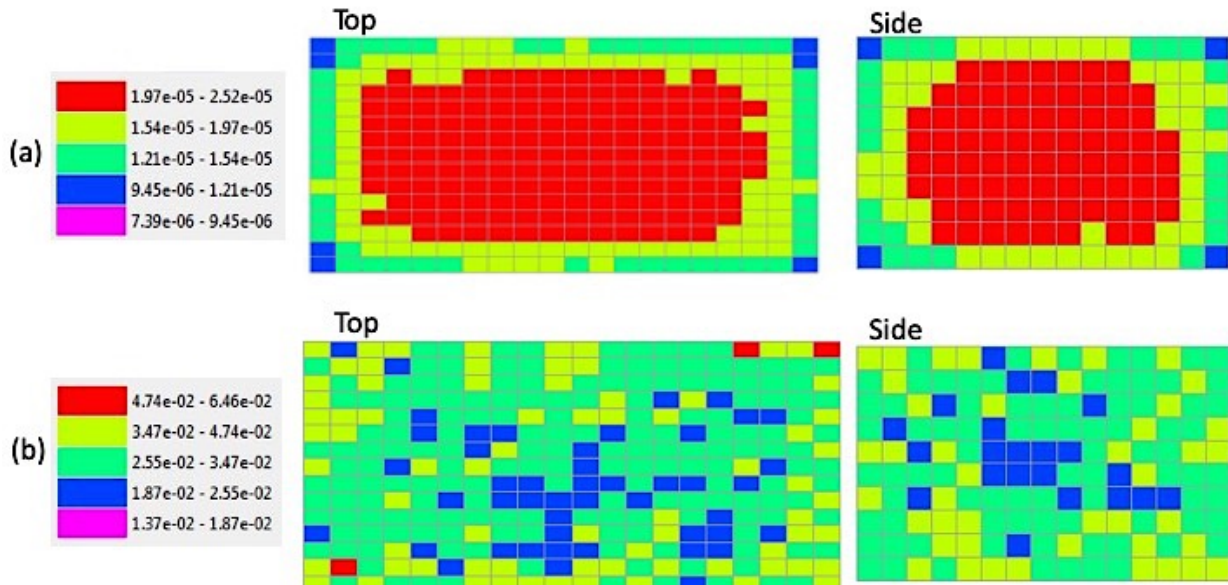


Figure 8.3: (a) Mesh tally of internal dose rate (rad/hr) within a single brick. (b) Relative uncertainties in the calculated dose rates (a).

In a more realistic scenario, the dose rates to bricks within a brick wall would be of interest. As an example, consider a brick wall measuring 33 m long by 5 m high by 0.7 m thick, composed of standard composition bricks (McConn Jr., 2011), each with an internal source term determined by the radionuclide composition measured by the G30 detector. For the full-scale wall simulation, the dose was tallied on a grid approximately the size of common brick in order to reflect the actual measure of interest (e.g. dose rate to a single brick). Figure 8.4 shows the calculated resultant absorbed dose rates in the simulated wall. It can be seen that the maximum dose rates again occur at the center of the geometry. For the case of the wall, the maximum absorbed dose rate averaged over the volume of a single brick was calculated to be 5.510 ± 0.003 mGy/yr. The dose rate distribution in the wall is also shown with the same gridded cell size as the side portions in Figure 8.4.

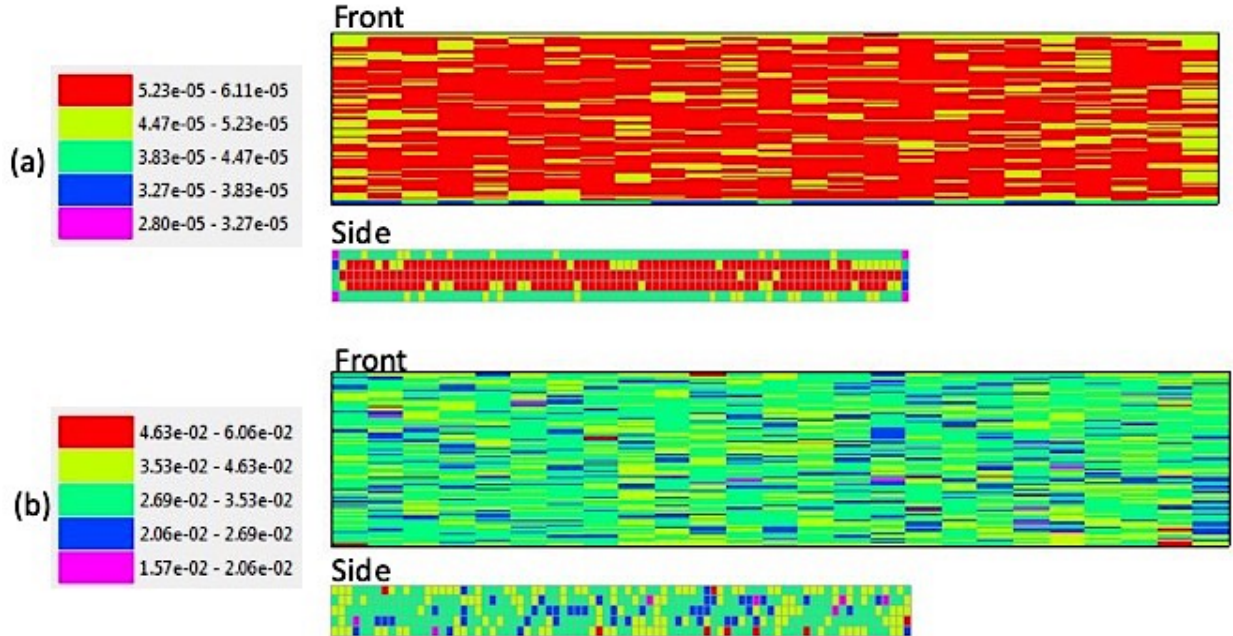


Figure 8.4: (a) Mesh tally results of the internal dose rate (rad/hr) in a simulated brick when including all emissions including those from neighboring bricks. (b) Relative uncertainties in the calculated dose rates (a).

Finally, a Sampler perturbation analysis was performed as a first attempt to quantify the potential variability in the internal dose rates of a brick due to the constituent radionuclide concentrations (Williams et. al., 2005). For the perturbations, the activity concentrations of each of the measured radionuclides were sampled from normal distributions whose mean and standard deviation parameters were taken as the measured activity concentration and the uncertainty in that same activity concentration, respectively. The radionuclide concentrations were sampled 200 times. In each sample, Origen was used to calculate the total source term for the brick. Then that source term was distributed uniformly throughout the volume of the brick and a Mavric transport calculation was performed for a new volume averaged dose rate estimate for each realization. Figure 8.5 shows the histogram of the calculated annual volume averaged dose rates for the simulated bricks.

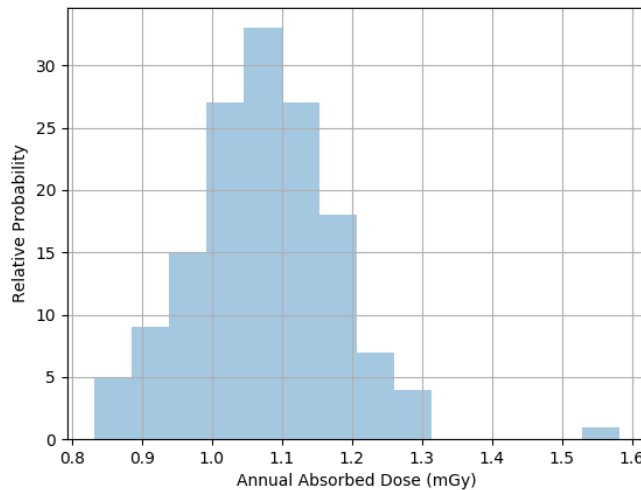


Figure 8.5: Histogram of calculated annual volume averaged dose rates within the brick material for the 200 sample runs.

In order to better estimate the population distribution of annual dose rate estimates, a kernel density estimate, with a Gaussian kernel function (e.g., weighted histogram), was performed on the sample realizations. The resultant kernel density estimator (KDE) is displayed in Figure 8.6. Kernel density estimators are a standard statistical tool for smoothing sampled data (Smith, 2014). Ideally, the resultant distribution will be representative of the underlying population distribution from which the samples were drawn.

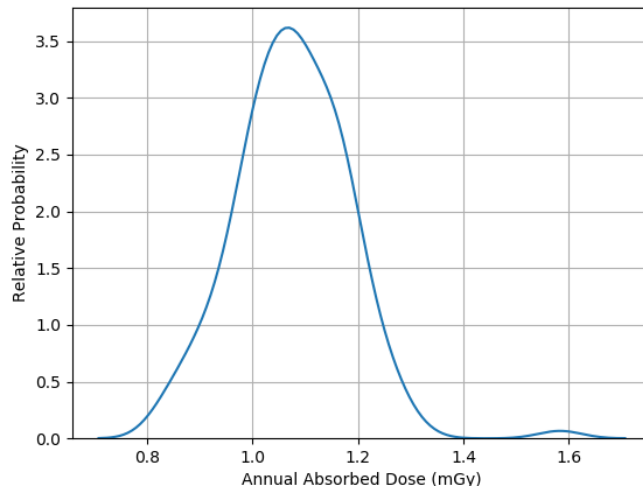


Figure 8.6: Kernel density estimate of annual volume averaged dose rates within the brick material for the 200 sample runs.

Based on the KDE of the 200 sample perturbation cases, the average annual dose rate within the brick was estimated to be 1.1 ± 0.1 mGy/yr, at the $1-\sigma$ level. As expected, the uncertainty in the internal dose rate to the bricks, due to uncertainties in the constituent radionuclides, is significantly greater (approximately 60 times) than the Monte Carlo uncertainties.

8.4 Discussion

Compared to the low-level counting experiments, the in-laboratory radioisotopic assay (via a portable HPGe) was able to detect between 65 and 75% of the radioisotopes identified by the former. As expected, the radioisotopes where the portable HPGe failed were those that were associated with low-energy photon emissions (e.g. Th-228, Th-231 and Th-234). For low energies, the Compton buildup masks lines from ambient background fields. For the purposes of this analysis, to emulate a radioisotopic assay in the field, there is little that could be done to improve detection of photons below 200 keV without additional instrumentation such as Compton suppression. The Compton background in this low energy range is sufficiently large both with and without the brick enclosure to obscure small, low energy photopeaks.

Based on the low-level counting experiments, some of the low energy emitting thorium isotopes can be relatively large contributors to the total activity of the brick material. This is potentially problematic for calculations of the internal dose rate of brick structures, because these low energy photon emissions from these radioisotopes would be expected to deposit most of their energy within brick material. As a result, those low energy photon sources could contribute to the brick's internal dose rate disproportionately to their relative content in the brick material. These low energy photon sources also have the potential to increase the normal gradient of the dose depth profile into the face of the brick.

It was also found that by using forward transport modeling to account for the photon detection efficiency differences between the gamma rays originating from the background environment and those originating within the brick shield, it was possible to estimate activity concentrations within the brick material that agreed with the low-level counting experiments. The method presented, in its current form at least, does suffer from significant limitations. Namely, since it relies on comparing the photon generation rates calculated from identical gamma lines between the background and shielded spectra, only those lines present in both

spectra are useful. As a result, the possible resolution of the technique is determined by the number of gamma lines that can be resolved in the lowest resolution spectrum, generally the shielded spectrum. This mainly affects the low energy end of the spectrum, since the shield acts as a source of scattered environmental background photons. This also results in relatively large uncertainties in the final activity estimates for those nuclides where only a single, common gamma ray line can be identified between the unshielded and shielded spectra. Finally, the analysis in the approach presented here is not easily automated, making it quite laborious and complicated, and therefore not highly desirable for routine use.

8.5 Conclusions

Luminescence dosimetry is an attractive technology for nuclear safeguards and security due to the passivity and prevalence of dosimetric materials. However, technical challenges and questions still exist, such as long integration times, lack of specificity and lack of uniformity of these materials. For example, the integration time for a luminescence dosimeter is the lifetime of the dosimeter material, from the last time the signal was zeroed until the time that the signal is read. As a result, these materials have a constantly growing background signal due to dose contributions from environmental radioactivity (internal and external). In order for an anthropogenic dose to be detectable by luminescence dosimetry, the magnitude of the anthropogenic dose must be large relative to the background dose absorbed over the lifetime of the material.

This work presented a method for determining the radioisotopic constituents of common brick material using a simple portable HPGe detector. With the measured radionuclide constituents, it has been shown that using a gamma-ray source calculation code and a photon transport code, such as Origen and Mavric, respectively, it is then possible to estimate an annual dose rate to the brick material, including the edge effects present at the outer faces and corners of brick. This would allow an investigator to then estimate the total background dose expected in a brick as a function of position in the brick (if the age of the building could be estimated). Knowing the naturally occurring background dose and internal radioactivity content for a ceramic can then effectively enable a minimum detectable level to be estimated for any anthropogenic dose.

Chapter 9

Retrospective Assay and Localization of an Unknown Source Using Luminescence Dosimetry

This material was submitted as:

O'Mara RP, Hayes RB. Retrospective Assay and Localization of An Unknown Source Using Luminescence Dosimetry. *Nuc. Instr. Meth. A.* 20 19. (Submitted)

9.1 Introduction

Recent studies in the field of luminescence dosimetry have demonstrated the potential to assay sources (O’Mara and Hayes, 2018; see Chapter 4) and even determine the historical locations of source material (Hayes and O’Mara 2017, 2020) through photon dose measurements in distributed dosimetric materials. It has even been shown that small electronic components, common to nearly all electronic devices, carried by most individuals in developed nations, can serve as personal dosimeters in the case of a radiological emergency (Hayes and O’Mara, 2019). All of these prior studies have demonstrated the potential utility and impact that luminescence dosimetry could have in nuclear security, safeguards and radiological emergency response, should the technology ever be adopted, developed and implemented.

To date, the nuclear community does not implement luminescence dosimetry with ubiquitous materials in attempts to reconstruct historical radiological activities at nuclear facilities. The purpose of this study was to demonstrate an application of luminescence dosimetry as an investigational tool for confirming historical radiological activities. To support that purpose, the following study was structured as a single-blind study, wherein the party performing the analysis had no prior knowledge about the identity of the source material, nor the location of the source with respect to the irradiated samples.

In past analyses, particularly those involving retrospective energy assay of photon sources, the energy was determined by comparing measured dose deposition profiles to those simulated by particle transport codes (Hayes and Sholom, 2017; O’Mara and Hayes, 2018; Chapter 4). Those methods require precise knowledge about the nature and position of the source prior to calculating the expected dose deposition profile and then source energy. Without prior knowledge about the historical source position, the first step in characterizing the source is generally to determine a likely source position. The simplest method for estimating the historical location of a source is by choosing a source geometry for which a closed-form equation for the geometric dose distribution exists, e.g. a point source. An alternate method is by employing computational optimization methods for a full transport model with a distributed source. Inferring source energies or material types is an associated exercise in discriminating dose depth profiles from spatial distribution effects.

9.1.1 The Inverse Radiation Transport Problem

The general problem of inferring properties of a radiological source is a special class of optimization problems, known as the inverse radiation transport problem. In general, solutions to the inverse radiation transport problem can be found through a series of iterative updates to any unknown source parameters, followed by forward radiation transport calculations and determining the goodness-of-fit between the simulated results and the measurements. Then the input source parameters are updated based on the goodness-of-fit measure. Ideally, the updates to the unknown parameters would follow the gradient of the underlying goodness-of-fit function. This can be confounded, in general, as the gradient information can often be either not reliable (noisy or near a local rather than global minimum) or too costly to calculate.

In cases where gradient information for the optimization problems' goodness-of-fit function is unavailable, black-box optimization routines exist. Such black-box optimization routines generally do not require access to information such as the cost function, goodness-of-fit, the function itself or its gradient. One such optimization method based on Bayesian analysis is the delayed rejection adaptive metropolis (DRAM) Markov chain Monte Carlo (MCMC) method.

One of the most attractive characteristics of the DRAM method is that it treats the unknown parameters as random variables with their own probability distributions (Smith, 2014). In this way, the method itself recognizes the likelihood of uncertainties inherent to the unknown parameters themselves. The DRAM method then works by attempting to determine the posterior distributions of the unknown parameters and then account for how those uncertainties are propagated through the model under investigation (Miles, 2018). One drawback to such MCMC methods is that they do not attempt to converge towards optimal parameters, like the gradient descent methods. In contrast, an MCMC method would prioritize thoroughly sampling the parameter space in order to build reliable posterior distributions for the parameters of interest. However, with the posterior distributions, one is provided with not only a likely optimum parameter value but also a measure of the uncertainty in that optimum value based on the obtained knowledge of the distribution under the assumption that the parameter space has had an adequately dense sampling.

9.2 Materials and Methods

9.2.1 Sample Setup

All sample irradiations were performed at the Device Assembly Facility (DAF) at the former Nevada Test Site during the summer of 2018. Our goal was to effectively emulate a scenario of some radiological activity where an inspector might reasonably expect to collect samples for luminescence dosimetry. To do this, a mock wall was constructed out of randomly selected brick and tile materials obtained from a local hardware store. Figure 9.1 shows images of the wall received by the investigating party that were subsequently used to model the wall geometry for photon transport calculations. Figure 9.2 shows the model reconstruction used in the particle transport simulations carried out using MCNP6® (Goorley et al., 2011).



Figure 9.1: Images of the mock wall constructed for testing the ability to retrospectively assay and locate the unknown source. The left image was the bottom and the right image was the top of the mock wall. The brick samples are seen in the lower left with OSLODs attached.

It can be seen from the images that nanoDot® optically stimulated luminescence dosimeters (OSLDs) were affixed to the back of the wall and brick base. These OSLDs were originally intended to serve as secondary confirmation of the exit dose following irradiation of the samples. It can also be seen from the images, that no useful information about the source

location or identity could be gathered from the supplied images and had to be obtained by retrospective dosimetry alone.

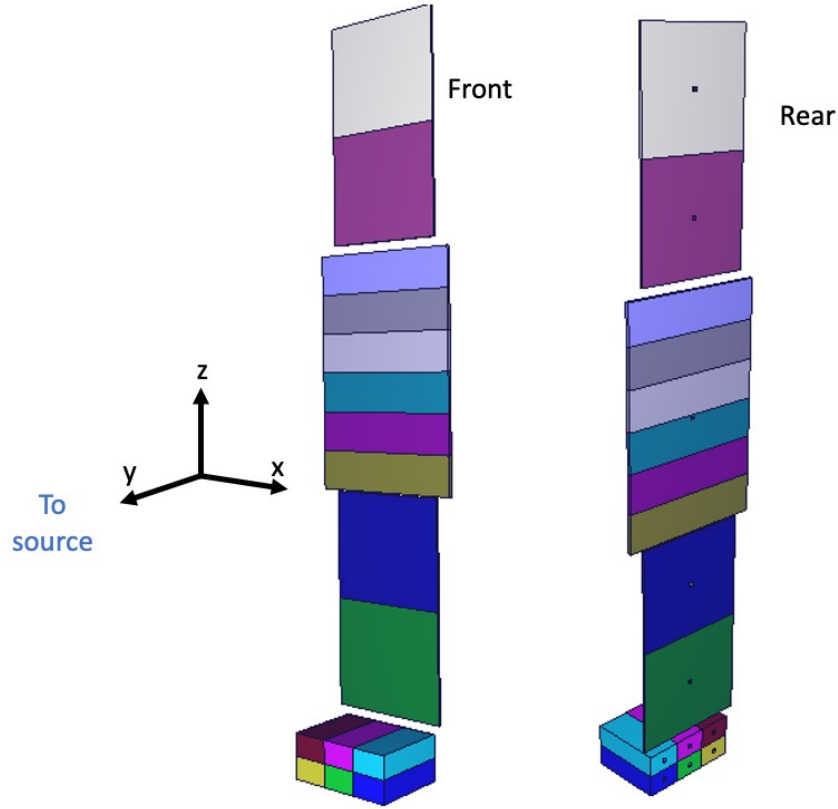


Figure 9.2: Vised rendering of modeled geometry for the mock wall irradiated at the DAF in the summer of 2018 (Schwarz et al., 1993).

9.2.2 The Source

The mock wall was exposed to a critical burst from the GODIVA IV criticality assembly without the knowledge of the individual conducting this analysis. The burst was a prompt critical excursion resulting in a 137°C rise in temperature due to an excess reactivity of 108.6 cents. Since the dosimetric materials used in this experiment are primarily sensitive to photons, only the photon spectrum resulting from the critical excursion was of interest.

The GODIVA IV assembly is a cylindrical core, 17.8 cm in diameter by 15.2 cm in height, composed of six stacked rings of uranium-molybdenum alloyed metal (1.5 wt% molybdenum). The core has a mass of approximately 66 kg and is composed primarily of 93.5 wt% enriched ^{235}U . In addition to the core there are a number of structural components

surrounding the core. The structural components are intended to keep the core intact during a prompt critical burst. A critical burst is then terminated when thermal expansion of the core causes the electromagnet holding the core to disengage, allowing the core to dismantle itself.

9.2.3 Sample Preparation – Source Localization

As previously mentioned, the first step in this analysis was to attempt to determine the position of the source relative to the mock wall. Pursuant to this, the OSLDs affixed to the back side of the wall were the first data to be collected. The doses to the OSLDs were read on a microStarri medical dosimetry unit by Landauer®. The doses to the OSLDs were then used to calculate an initial estimate of the probable source location.

Once an initial estimate of the source location was generated, samples of the tile material were selected in an attempt to refine the location estimate. All sample preparation was performed under subdued red lights. Initially, 2.54-cm diameter samples of tile material were removed from the bulk tiles. The tile samples were crushed with a mortar and pestle and then sieved to collect those grains with diameters in the range of 90-250 µm. The samples were then divided into smaller aliquots, loaded into stainless steel cups and analyzed using a Risø DA-20 TL/OSL reader. All samples were analyzed using a single aliquot regenerative (SAR) protocol (O’Mara and Hayes 2018; Chapter 4), using blue LEDs as the stimulation source.

It was later found that the tile exhibited a very low sensitivity to radiation dose. It was hypothesized that the weak dose response was due a lack of aluminum oxide grains in the tested aliquots. As a result, more tile samples were later prepared in a similar manner as above, except for the latter samples an IsoMet® wafering saw was used to remove the top 2 mm of the tile in order to isolate the tile glaze. The glaze samples were then crushed, sieved and analyzed in the same fashion as tile samples.

9.2.4 Sample Preparation – Energy Assay

Based on the estimated location of the source, it was decided to analyze the dose deposition in the brick perpendicular to the top surface of the brick. A 2.54-cm diameter cylindrical core of brick material was removed from the center, top brick. The brick core was sliced into 2-mm thick discs using the low speed IsoMet® wafering saw set to a cutting speed of

150 rpm. Then each disc was prepared in the same manner as the tile samples discussed above. The dose to each slice was then measured using the same blue light SAR protocol.

9.2.5 Computational Optimization

All forward transport calculations were performed using MCNP6® (Goorley, 2012). Because no information was available about the source geometry, the source was initially modeled as a simple point source. The unknown parameters in the modeled source geometry were initially taken to be the x, y and z positions of the source and the source energy. The optimizations of these unknown parameters were broken up into two stages. First the source positions were sought, and then the source energy was calculated for a source located at the estimated location. Finally, the size of the source was estimated by assuming that the source was spherically distributed.

The spatial parameter (x, y, and z) optimizations were handled using the DRAM method in the *pymcmcstats* python module (Miles, 2018). The *pymcmcstats* module is a general-purpose MCMC package that allows for simple integration with black box problems. A python wrapper was written to integrate the *pymcmcstats* framework with the MCNP6® model evaluations, and *pymcmcstats* handled all of the parameter sampling and chain tracking tasks. In this case, the cost function was defined as the sum-squared errors between the measured and simulated doses of interest. Each optimization run consisted of 5000 model evaluations with a burn-in period of 1500 evaluations. The choice in the number of model evaluations was made primarily due to the constraints imposed by the use of a standard desktop computer for the optimizations.

The brick compositions were modeled as standard red bricks, with densities of 2.3 g cm^{-3} (McConn, 2011). The tiles were modeled as composed of porcelain (kaolinite; $\text{Al}_2\text{Si}_2\text{O}_5(\text{OH})_4$) with a density of 2.65 g cm^{-3} . The glaze on the tiles was ignored for the transport calculations because the sub-millimeter thickness of the glaze was not expected to add a significant amount of photon attenuation. For the source location optimization runs, the doses to the nanoDot® OSLDs were modeled as point detector (F5) tallies, centered on the aluminum oxide element of the OSLD. The use of the point detector tally in this case allowed for significantly shorter run times. Each forward transport calculation was allowed to run for 100 minutes of computer time, again to keep computational times reasonable. The position parameters were constrained only to ensure that the source was not positioned in the wall itself.

For the source energy optimizations, the doses to brick core slices were modeled by modified pulse height (*F8) tallies. Due to the higher complexity of the pulse height tally compared to the point detector tally, the energy optimization forward transport calculations were allowed to run for 1200 minutes of computer time. Although the true densities or compositions of the bricks and tiles were not measured in this case, the natural variability in characteristics are much smaller than other measurement factors such as the luminescence sensitivity of the quartz in the brick. In the end, it was determined that the Bayesian techniques used for determining the size and shape of the source were too computationally expensive for the initial analysis. Instead, the energy was estimated by searching for a minimum in the sum-squared residuals between the measured and simulated dose deposition profiles using a bisection approach (Press, 1992). Although this method required fewer forward transport calculations, it was time consuming because the process was not automated at the time of the analysis.

9.3 Results

9.3.1 Source Location

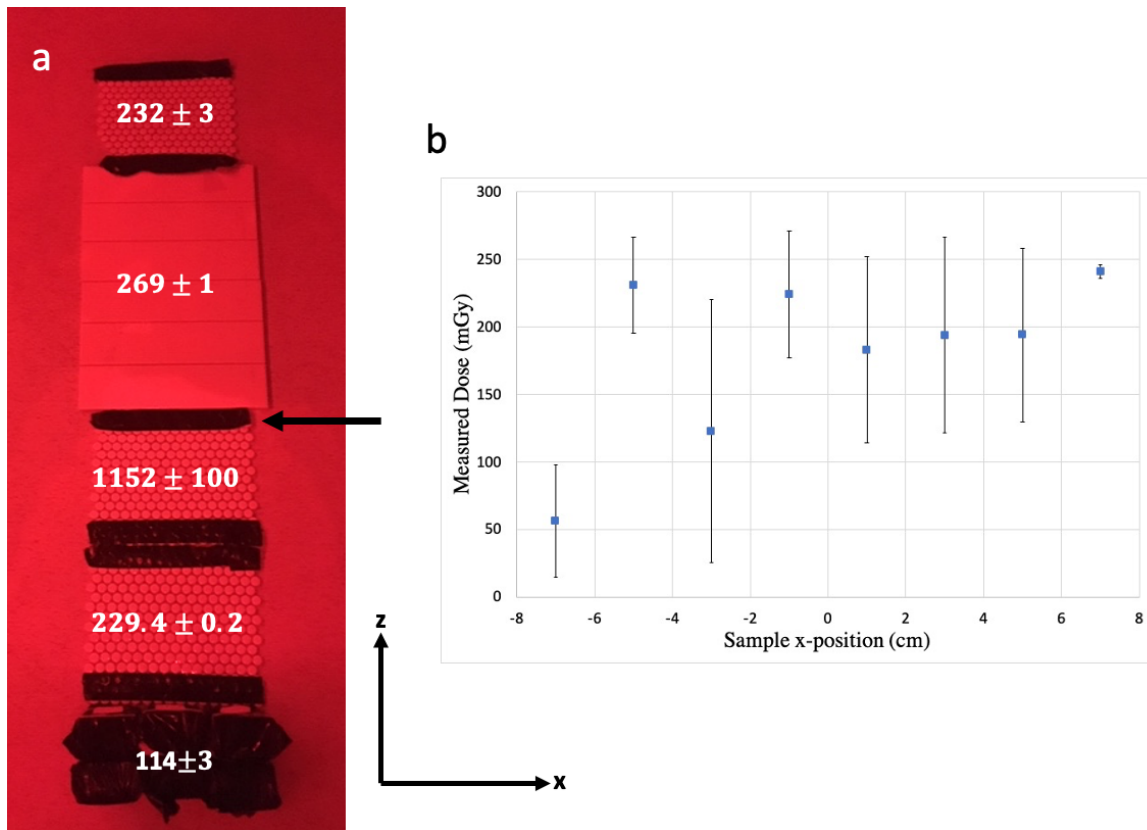


Figure 9.3: (a) Wall, rebuilt at North Carolina State University, with OSLD doses (in mGy) placed in the relative locations of the dosimeters. (b) Doses measured to tile glaze samples taken from the row of tile dots located at the arrow.

Figure 9.3a shows an image of the mock wall with the measured doses (in mGy) transcribed in the locations of the dosimeters. It can be seen from the plot in Figure 9.3b that the doses measured by the tile glaze were substantially smaller than the dose measured by the dosimeter affixed behind the nearest tile giving an apparent underestimate (being lower than the values above or below on the array). Whether this was from transient signal contributions, sample preparation or analysis upsets was unclear. This was not investigated further as the OSLD results did not present any indications of confounding factors. The decision was then made to rely on the OSLD dose measurements for the initial source localization rather than the doses to the tile material.

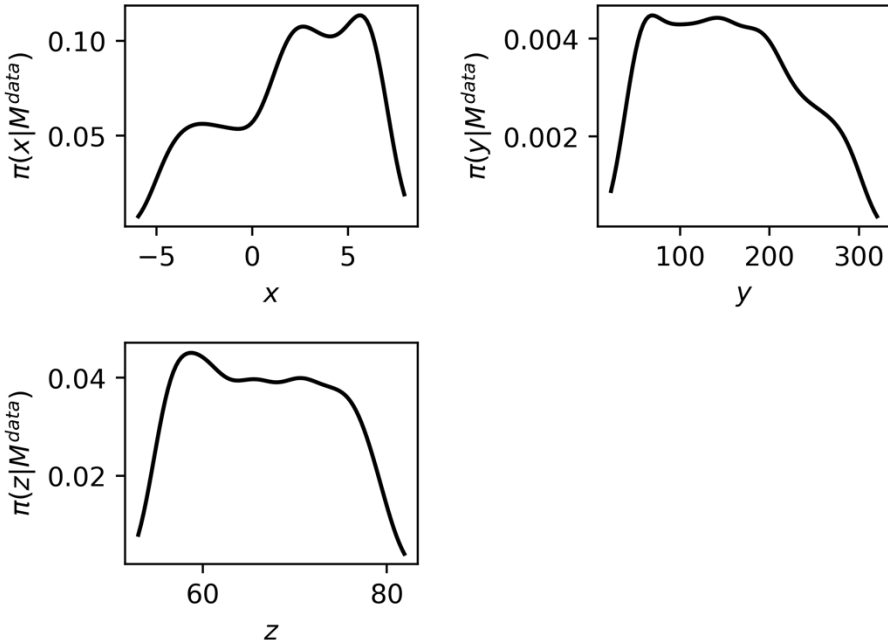


Figure 9.4: Marginal posterior density distributions obtained for the x-y-z position of the simulated point source. The width of the distributions is indicative of the relative insensitivity of the sum-squared errors with respect to the parameters. Ideally the x and z distribution widths should be close to 15 in these units for an accurate prediction.

Figure 9.4 shows the marginal posterior distributions obtained for the x, y and z coordinates of the source that would deliver the measured doses to the OSLDs, assuming an initially isotropic source probability distribution. The marginal posterior density, $\pi(x_i|M^{data})$, gives the probability density of parameter x_i 's given the measurements, M^{data} . The optimized source coordinates and uncertainty estimates can then be taken as the mean and standard deviation of these posterior distributions. Following this methodology, the source location was determined to be $x = 0.87 \pm 1$ cm, $y = 148 \pm 80$ cm and $z = 68 \pm 6$ cm relative to an origin (0,0,0) point located at the bottom back surface of the modeled wall. Essentially these results indicated that the source would have been located roughly centered to the wall (in the x-direction), about 70 cm from the floor and approximately 1.5 m from the surface of the wall.

Since it was assumed that the true source distribution was unlikely to be a point in space, the next step was to attempt to determine a spatial extent parameter for the actual source distribution. To this end, the source was next modeled as a uniform, spherical volume distribution, in vacuum, centered on the coordinates determined above. One of the main repercussions of using a volume source distributed in a vacuum is that any self-attenuation within the source material will be neglected. Although the effect of self-attenuation would be

expected to be greater for source energy determination, for a true source composed of a sufficiently dense material, self-attenuation could have an effect on the source size determination because the amount of attenuation in the source effectively limits the amount of source material that the dosimetric materials see. However, since the methods used here depended on relative dose deposition shapes, the source self-attenuation effects on source shape determinations are somewhat limited. Based on these assumptions, the optimum radius of a spherically distributed source was estimated to be 2.4 ± 1.0 cm, again using the DRAM module.

Table 9.1 contains the calculated and known values for the source location and spatial extent (assumed radius). Because the source was not actually a sphere, for comparison the radius parameter was taken to be the radius of a sphere with the same cross-sectional area as the Godiva assembly. Also contained in Table 9.1 are the z-scores for the hypothesis that the true parameter values were members of the calculated parameter distributions. Using the critical *t* value (T^{crit}) of 1.960, it can be seen that only the spatial extent parameter disagreed at the 95% confidence level using this spherical approximation model.

Table 9.1: Comparison of Estimated Spatial Parameters with the Known Values.

Parameter	Calculated (cm)	True (cm)	Z-Score
x	0.87 ± 1	0	0.87
y	148 ± 80	200	0.65
z	68 ± 6	70	0.33
radius	2.4 ± 1	9.28†	6.88

† Assumes true source distribution is a sphere with the same cross-sectional area as the cylindrical assembly.

9.3.2 Source Energy

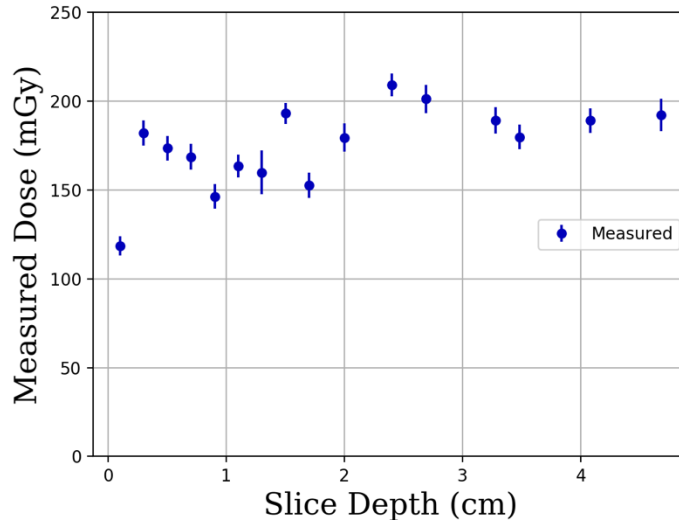


Figure 9.5: Measured dose deposition in the brick core plotted against depth into the brick.

Figure 9.5 shows the measured dose deposition profile from the brick core. It was initially assumed that the experiment had failed, because unlike previous experiments, the measured dose deposition profile did not exhibit any resemblance to a decaying exponential. However, the experiment proceeded in the interest of determining the conclusions that would be drawn from the measured data.

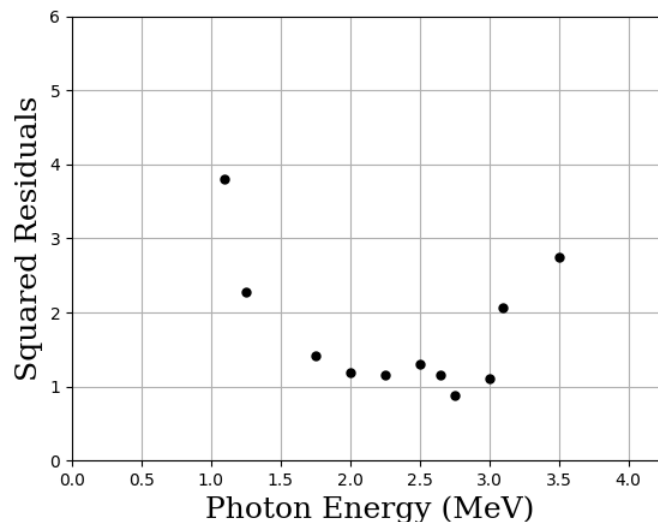


Figure 9.6: Plot of the sum-squared residuals between the measured and simulated dose deposition profile in the brick near the minimizing energy value.

Figure 9.6 shows a section of the plot of the sum-squared residuals between the simulated and measured dose deposition profiles near the eventual source energy estimate. In general, the optimized energy is the one which minimizes the sum of the squared residuals between the measured and simulated dose deposition profile. Additionally, it was described (O'Mara and Hayes, 2018; Chapter 4) how fitting the inverted sum-squared residuals plot with a Gaussian provides not only an optimal energy estimate but also an uncertainty estimate. Figure 9.7 shows the Gaussian fit to the inverted sum-squared residuals. From the fit parameters of the Gaussian in Figure 9.7, the source energy was determined to be 2.6 ± 0.9 MeV. After these results were obtained and disclosed, the identity of the source was finally revealed to the investigator June 16th, 2019 during the initial presentation of the findings from above.

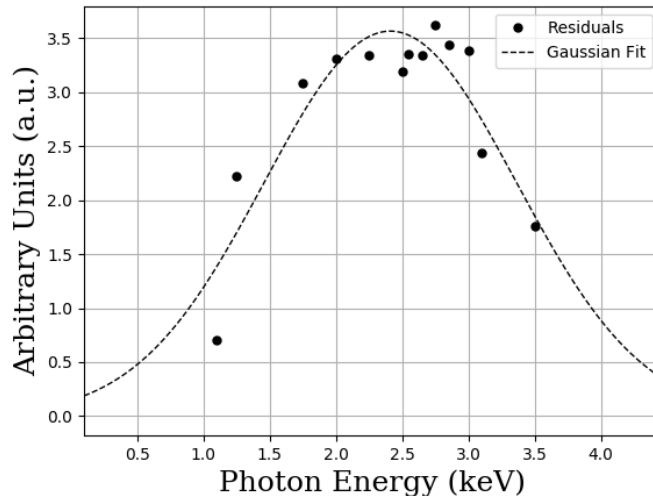


Figure 9.7: Gaussian fit to the inverted sum-squared residuals between the measured and simulated dose deposition profile in the brick.

In order to test the agreement between the estimated source energy and the true source energy it was necessary to calculate the source spectrum from a critical burst of highly enriched ^{235}U . It was decided that only the prompt gamma ray spectrum would be considered, since the vast majority of the delivered dose results from the prompt gammas from fissions (Shultis and Faw, 2000).

The Godiva assembly was modeled as simple cylinder 17.8 cm in diameter by 15.2 cm in height. There were a number of effects that had to be considered in order to accurately model the gamma spectrum exiting the Godiva core. First, the gamma source strength is proportional to the number of fissions occurring in the core. As a result, a higher fission gamma density will occur

closer to the center of the core and will therefore be subjected to greater self-shielding with exponentially increasing attenuation with decreasing energy. Next, the fission gamma energy distribution was sampled from the Peele and Maienschein (1970) fission spectrum approximations.

In order to define the gamma source density distribution throughout the core, the core material was divided into concentric cylinders. Then a converged critical k-code calculation was run in order to calculate the number of fissions in each of the cylindrical regions. The calculated fission densities from the k-code calculations were then used to define the gamma source densities in each of the regions. Next, a forward photon transport calculation was performed using the k-code determined source term densities where the photon energies exiting the surface of the outer cylindrical core were tallied with a surface flux (F2) tally. The number of concentric cylinders was increased, and the above steps were repeated, until the gamma spectrum exiting the core was constant. A thin Al cladding shell was ignored in this analysis. Figure 9.8 shows the final spectrum calculated for 20 concentric cylinders.

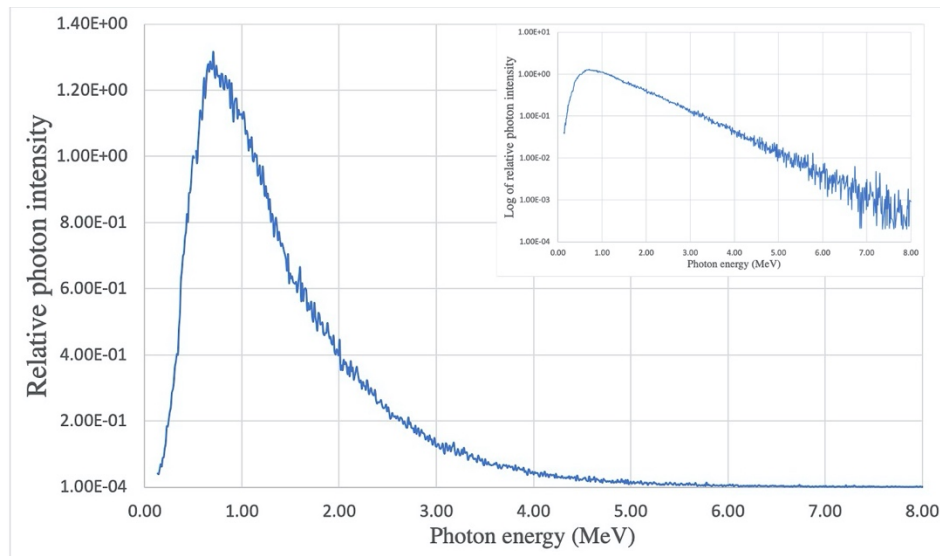


Figure 9.8: Calculated photon spectrum from prompt fission gammas exiting the HEU core. *Inset:* Semilog plot of the relative photon intensity.

The true energy source was then calculated as the average energy of the photon spectrum in Figure 9.8. The resultant source energy was 1.365 MeV. The z statistic for the hypothesis that the true source energy and the estimated energy are statistically identical ($T^{crit}=1.960$) was

calculated to be 1.37. Therefore, the measured and estimated energies ultimately agreed at the 95% confidence level.

9.4 Discussion

One of the primary challenges faced in this analysis was that the dose delivered to wall materials was relatively small. As a result, it was difficult to determine whether the reconstructed doses were physically consistent with the exposure that had occurred or whether the results were effectively noise. A number of factors determine the noise level when performing dose measurements with ubiquitous building materials and that noise level determines the detection limit of these techniques (e.g. any background dose, unrelated to the event of interest, absorbed by the materials). If the background dose is large compared to the anthropogenically delivered dose, then it could confound detecting the anthropogenic dose. That was not expected to be a problem in this case, since the materials were fairly new. However, a more relevant concern in this analysis was that the delivered doses were relatively small (up to 1 Gy, Figure 9.3b). Depending on the material and preparation methods used, the detection limits for optically stimulated luminescence in quartz can be on the order of tens to hundreds of milliGray (O’Mara and Hayes, 2018, Chapter 4). This effect can be seen in the results obtained from the samples of tile glaze (Figure 9.3b). As a result, significant doubt existed in the beginning of this study as to whether the analysis would yield fruitful results.

Although the results are promising for a first-ever single-blind retrospective source assay and localization study, a number of improvements could be made to the methods used here. Methods are currently being explored in an effort to decrease the detection limit of the tile material in order to allow meaningful dose estimates to improve the source localization capability. However, in a true operational facility, one could expect larger doses to ubiquitous building materials (due longer integration times for multiple exposures) and thus lowering the detection limit would be less of a concern. Further, it is likely that using the DRAM routine to determine the posterior distribution of the energy would yield a more precise energy estimation and uncertainty. This though would incur a significant computational cost. Other considerations with regards to the source energy estimates might include the effects of the external structural supports present around the Godiva core (hardening the spectrum resulting in a higher average energy expectation) and the effects of delayed gammas from fissions (softening the spectrum). In

a practical sense, the improvements in the true source spectrum would probably be relatively small compared to the uncertainties in the measured dose estimate and thus any gains in accuracy might be marginal.

Finally, the apparent inaccuracy in the size determination of the source should be addressed. Referring to Table 9.1, the “true” size of the source was taken to be the radius of a sphere with the same cross-sectional area as the Godiva core. It must be recalled that for a distributed source, the photon flux at a distance of ten times the characteristic length of the source distribution is approximately equivalent to the flux from a point at the center of the source distribution. For convenience, letting the characteristic length, L_c , be equal to the square root of the cross-sectional area of the Godiva assembly would result in a L_c of approximately 16.4 cm. Since the dosimetric materials used in this analysis were placed at a distance of 2 m from the source, it should be expected that the photon flux at the wall was roughly equivalent to that of a point source. As a result, it may be physically impossible to resolve the true size of the source in this case. That is not to say, however, that the size estimate would offer no investigative value. With knowledge of the physical dimensions of the space from which such retrospective dosimetry samples were collected it would be possible, beforehand, to estimate the size resolution constraints for an unknown source based on its distance from the sampled surfaces. An investigator could then use that prior knowledge to put bounds on the possible size of any detected source and combining such a bounding estimate it may be possible to differentiate between likely sources without needing to precisely calculate the exact size of the source.

9.5 Conclusion

It has previously been shown that using luminescence responses in ubiquitous materials, it is possible to passively image and assay radiological sources (O’Mara and Hayes, 2018; Hayes and O’Mara, 2017). The current work shows that by coupling luminescence dose measurements with computational models and optimization routines, it is possible to localize and assay a radiological source even when no advanced knowledge about the source or exposure exists. This work was able to blindly discern the location and average energy of a critical assembly using this technique. The potential applicability of luminescence dosimetry for retrospective reconstructions of radiological source distributions has ramifications in both emergency response and nuclear security.

Chapter 10

Three-dimensional Positional Analysis of Weapons Grade Plutonium Using Gridded Arrays of Dosimeters

10.1 Introduction

Luminescence dosimetry has long been a mainstay in the realms of personnel and accident dosimetry; however, recent advances have demonstrated that these techniques may also have a place in nuclear nonproliferation and treaty verification. Previous research (see Chapter 4) has shown that using a combination of optically stimulated luminescence (OSL) and thermoluminescence (TL) allows for the assay of nuclear material with surprising resolution using common bricks as a spectrometer (O’Mara and Hayes, 2017). Likewise, doses to surface mount resistors (SMRs), like those found in common personal electronics, have been measured down to background levels using OSL (Hayes and O’Mara, 2018). Even more recently, a linear array of commercially available optically stimulated luminescence dosimeters (OSLDs) were used to localize the position of a weapons grade plutonium (WGpu) source (Hayes and O’Mara, 2020) effectively demonstrating any array of dosimeters might serve as a 3D gamma camera.

One of the principle challenges with respect to weapons treaty verification is that many conventional measurement techniques can reveal classified or protected information about the weapons. As a result, signatories of such treaties would be expected to object to the use of such instrumentation for verification activities. Gross dose rate information, such as that measured by luminescence dosimeters, on the other hand, can be expected to be much more palatable to treaty signatories since it is unlikely to contain protected design information given its current role as a simple radiation protection measure.

10.1.1 Analytical Source Position Analysis

As done previously (Hayes and O’Mara, 2020; Chapter 9) when using a single linear distribution of OSLDs, the positions of a spherical source can be approximated as a point source. Under this approximation, the linear array of measured doses will follow the functional form of

$$Y = m_1 / (m_2^2 + (Z - m_3)^2), \quad (1)$$

where m_2 is the radial position estimate and m_3 axial position estimate, in cylindrical coordinates. In Equation (1), the m_1 parameter is then simply related to the magnitude of the dose delivered. Under this coordinate system, the “z-axis” is the line connecting the linear array of dosimeters.

Applying Equation (1) for a single linear array of detectors, it was shown that the position of the source could be determined with a 1° angular resolution (Hayes and O'Mara, 2020).

Hayes and O'Mara (2020) also showed that by coupling forward particle transport solutions with black-box optimizations routines, the source position and radius could also be simultaneously determined (see also Chapter 9). It was noted, however, that using the full transport solutions were computationally expensive. As a result, it would be advantageous to use simplified methods, such as applying Equation (1), to solve for the approximate source position and then use the more computationally expensive routines only to solve for other source characteristics, such as the radius. This work builds upon the results reported by Hayes and O'Mara (2020), by illustrating a method by which a gridded array (or simply orthogonal linear arrays) can be used to solve for the three-dimensional position of a source. The resultant position could then be used in subsequent full transport models to determine other source characteristics.

10.2 Materials and Methods

All measurements were made in June of 2019 at the Device Assembly Facility (DAF) at the former Nevada Test Site. The source under investigation was a 4.48-kg sphere of WGPu with a diameter of 7.5876 cm. The WGPu sphere was constructed in 1980 with initial isotopic weight percentages of .02, 93.735, 5.95, 0.2685 and 0.028 for the isotopes of ^{238}Pu , ^{239}Pu , ^{240}Pu , ^{241}Pu and ^{242}Pu respectively with 557 ppm of ^{241}Am (Hayes and O'Mara, 2020).

Two arrays composed of nanodot OSLDs, by Landauer, taped to a foam board backing were constructed and exposed to the source for 85.7 hours. The first OSLD array, termed the large array (LA), was built on a foam board that measured 135 cm long by 90 cm wide. The LA consisted of a 10-by-10 array of OSLDS where the OSLDs on the long axis had a center-to-center spacing of 15 cm and those on the short axis had a center-to-center spacing of 10 cm. The second array, the small array (SA), consisted of an 8-by-8 array of OSLDs, with center-to-center spacings of 10 cm and 7 cm on the long and short axes, respectively. The foam board backing for the SA measured 70 cm by 49 cm in total.

Figure 10.1 shows the outer configuration of the OSLD arrays with the source in place. It can be seen from the image that the LA was suspended parallel to the floor, above the source using two utility carts. The SA was secured perpendicular to the LA on one of the utility carts. It can also be seen that the source was placed offset from the center of the LA, 20 cm closer to the utility cart supporting the SA.

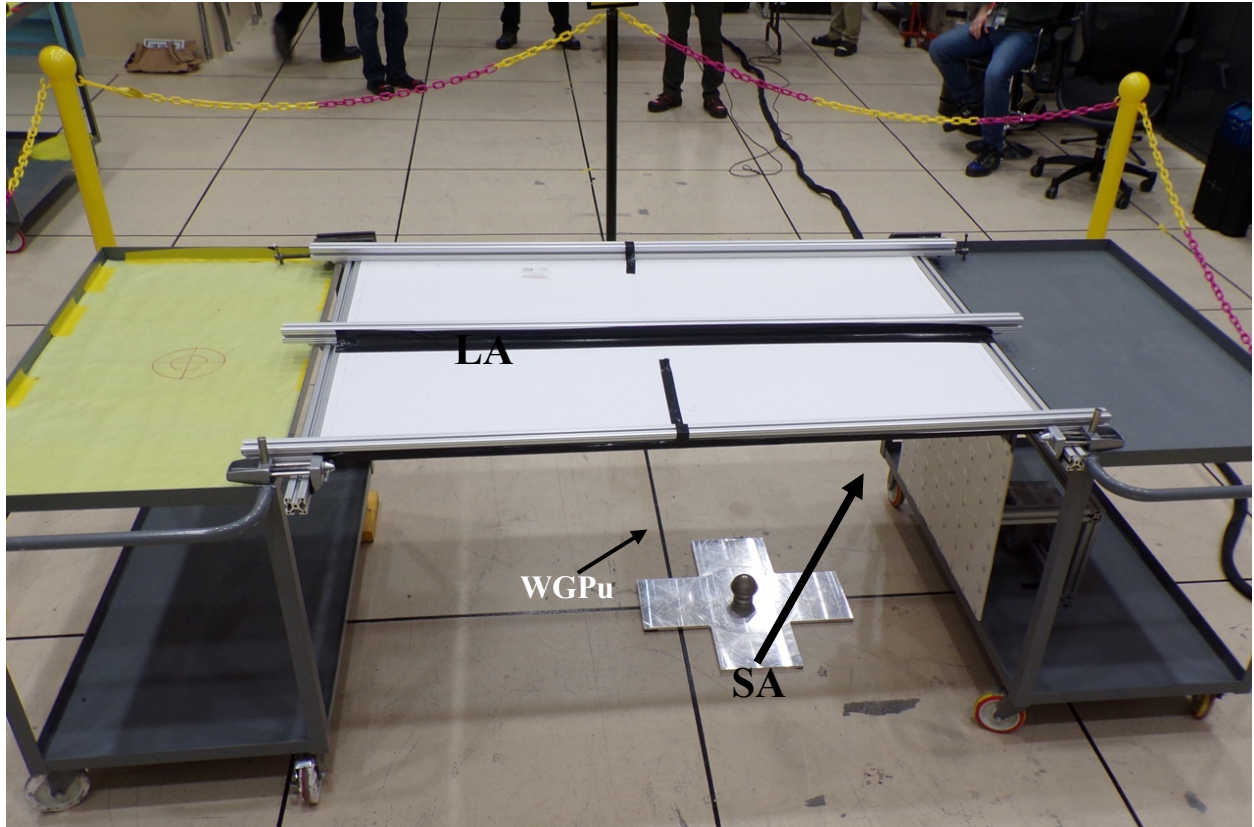


Figure 10.1: Outer view of the dosimeter arrays. The LA has dosimeters on the opposite side seen here with the SA having dosimeters visible. The clad WGPu was placed on a cross plate of Al on the floor composed of tile on top of concrete.

Figure 10.2 shows the position of the source from floor level. It can be seen here that the entirety of the SA is positioned above the source. As such, there is no line of OSLDs bisecting the source perpendicular to its central axis where the cladding has a lip. Also shown in Figure 10.2 is the aluminum stand that the source rests on. The benefit of having both arrays above the source was to reduce the shadowing effect by this stand and to reduce the albedo effect from the floor primarily from the metal cross upon which the WGPu was positioned (Figure 10.1). There is also a cladding lip around the WGPu which is partially shadowing the lower half of the WGPu to the SA but not the LA as shown in Figure 10.2.

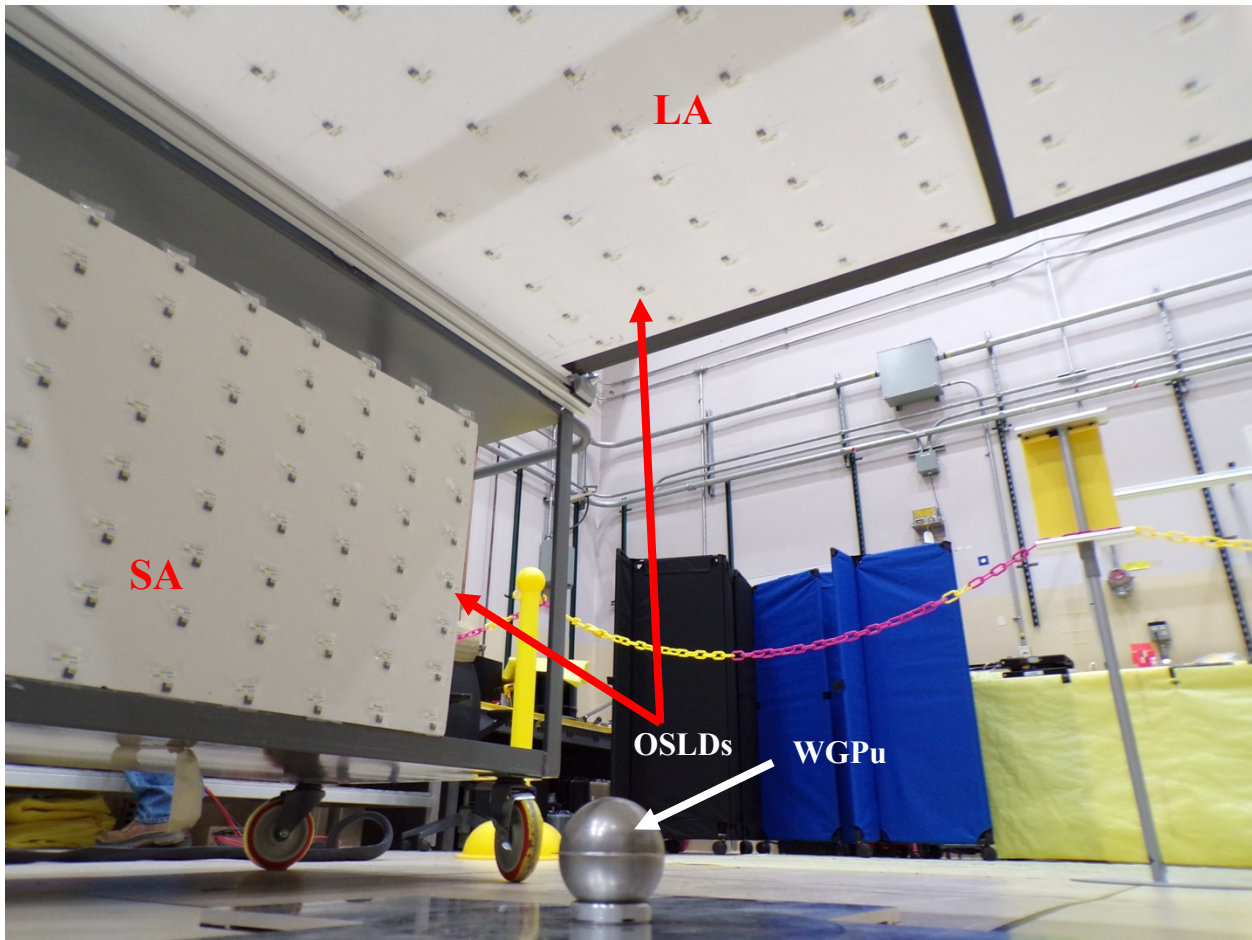


Figure 10.2: Underside of the exposure geometry, showing the weapons grade plutonium source and both of the dosimeter arrays.

10.2.1 OSLD Measurement

The dose to each of the OSLDs was measured using a Landauer microStarri® medical dosimetry unit. Prior to the measurement of the OSLD doses, a set of known exposure (NIST traceable doses) OSLDs were utilized to ensure the constancy of the unit calibration and dose estimates. Each dosimeter was read a single time; however, each read consists of a dose estimate from four individual LED pulses. The resultant dose estimate is then the average of the four pulses and the dose uncertainty is its standard deviation.

The nanoDOT™ OSLDs are all calibrated for exposures perpendicular to the top surface of the dosimeter cassette and as a result the dose estimates from the nanodots can be somewhat sensitive to the angle of the dosimeter relative to the irradiation source (Kerns et al., 2011). The angular dependence of the dosimeters was calculated by a Monte Carlo simulation using MCNP6® (Goorley, 2012). The source's photon spectrum was determined using the Origen

module of the SCALE package (Bowman and Gauld, 2010). The Origen calculation was used to decay the original, measured source material by 39 years and determine the expected present-day isotopic compositions and gamma source rate term. Only those gamma source rate terms with relative contributions greater than 1E-8 were included in the final source specification for the particle transport simulations. The source term was uniformly spread throughout the volume of the modeled plutonium sphere, in order to account for self-shielding effects.

The photon dose deposition in the $\text{Al}_2\text{O}_3:\text{C}$ chip within each dosimeter set was calculated using a pulse height, energy deposition (*F8) tally. The *F8 tally provides the energy distribution of “pulses” created in a cell modeled as a physical detector (Goorley et al., 2011). The source spectrum from the Origen calculation was transported mono-directionally at various angles relative to the surface of the simulated dosimeter. Finally, the angular correction factor was calculated as the ratio of the calculated dose deposition for an angle θ to the calculated dose deposition at 90° . The dose measurement for each dosimeter was multiplied by the correction factor calculated for the angle between the dosimeter and the center of the source.

10.2.2 Source Position Analysis

For each of the two dosimeter arrays, Equation (1) was first fit (using the Levenberg-Marquardt (LM) method) to measured dose profiles both row and column-wise, in order to obtain estimates for each of the two coordinates in the plane of the array (see Figure 10.3). The final coordinate estimates were calculated as the variance-weighted average of all of the m_2 parameters from the fit to each dosimeter row (or column). Next, the estimated in-plane coordinates were used to calculate the perpendicular distance between the source and the dosimeter plane using the m_3 , or radial position parameters from the fits of Equation (1) to each line of dosimeters. Given the estimates of the in-plane (axial) coordinates of the source relative to a given line of dosimeters, the perpendicular distance between the source and the dosimeter plane (e.g. the third spatial coordinate of the source) can be solved by applying the Pythagorean theorem where the length of the hypotenuse of the triangle formed between the source and a given line of detectors is equal to the m_3 parameter given by the fit of Equation (1) to the dose profile. Again, the final estimate of the out-of-plane coordinate was calculated as the variance-weighted average of all of the individual estimates.

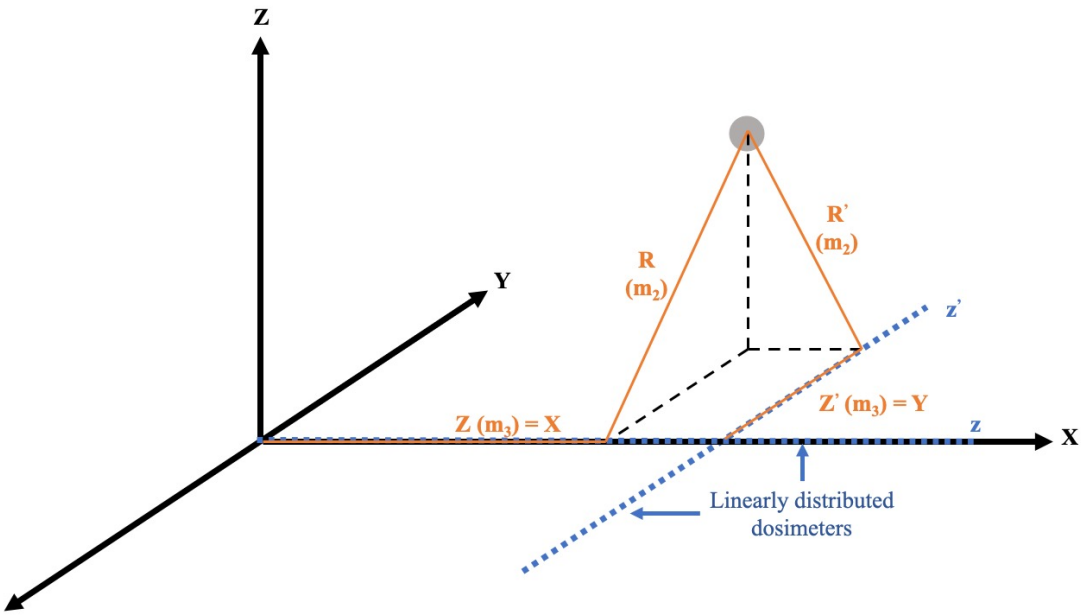


Figure 10.3: Method for determining the three-dimensional position of a point source using the dose estimates in two orthogonal linear arrays.

With the position estimates determined using the point source approximation, it was hypothesized that an estimate for the source radius would be attainable using forward transport modeling. A simplified model of the exposure geometry was constructed using the MCNP6® code. The modeled geometry included the source, aluminum stand, floor and OSLD arrays. In order to simplify the geometry specification, the utility carts supporting the OSLDs were ignored. Additionally, the OSLD arrays were each modeled as a continuous rectangle of aluminum oxide, Al_2O_3 , surrounded by a polyethylene case. Point detector (F5) tallies were placed in the Al_2O_3 region at the locations of the actual dosimeters. While this simplification ignores the spatial extent of the dosimeters, the cost of such a simplification is justified by the greatly reduced computational time required compared to pulse height (*F8) tallies. Further, it is not expected that this approximation will substantially alter the response of the tally compared to the actual energy deposition physics.

10.2.3 Inverse Transport Methods

The inverse transport problem is a special class of optimization problems where a parameter set in a forward transport model is optimized to match some set of experimental measurements. In many cases, such problems fall into another special class of problems known as black box optimization problems. The term “black box” refers to the non-analytical nature of

the forward transport solutions and further, generally implies that gradient information for the parameters of interest is either non-existent or prohibitively expensive to calculate. While many black-box optimization algorithms exist in the literature, this work only focused on relatively simplistic gradient-free, coordinate search methods.

The first, and simplest, solution method (the raster method) consisted of first defining a set of bounds for each of the parameters of interest, the spatial coordinates and radius of the source in this instance, and then computing the chi squared value between simulated and measured doses at equally spaced points within those bounds. Next, the bounds of the previous iteration were moved to bracket the parameter that minimized the chi squared. The subsequent interval was again divided into equally spaced points upon which the chi squared value between simulated and measured doses was calculated. This process of interval refinement was repeated twice and ultimately the parameter value that minimized the chi squared was taken to be the optimal value.

The second method used for the parameter optimization followed the same general approach as the previous method, where each spatial coordinate was optimized independently and sequentially followed by the radius. The main difference was that instead of using a graphical analysis of the chi squared distribution, the second approach used Brent's method to find the minimum of the chi squared values and the resultant optimum parameter value (Brent, 1973). The benefit of this approach was that since Brent's method is available in the Scientific Python, *SciPy*, optimization library it was relatively simple to implement and required no interaction with the user (Virtanen et al., 2020).

The bounds for each spatial coordinate were selected as a combination of the interval containing the highest dose dosimeters in each direction and any constraints imposed by the physical dimensions of the problem geometry, such as the locations of the floors and the arrays themselves. For example, in the large array, the bounds for the x and y coordinates were taken to be large enough to contain all OSLDs for which a dose greater than 1.6 Gy was measured. This resulted in x-bounds of [-20 cm, 40 cm] and y-bounds of [-25 cm, 45 cm]. The upper boundary of the z-interval was taken to be the largest coordinate of a dosimeter on the small array for which a dose greater than 3 Gy was measured, or between 0 cm and 40 cm, where 0 cm in this case was taken to be the surface aluminum cross plate.

10.3 Results

Figure 10.4 shows a graphic rendering of the exposure geometry in addition to the coordinate system used in all of the subsequent analysis and results. The resultant acquired dose profiles for the large and small arrays are shown in Figure 10.5 and Figure 10.6 respectively. In these figures, the dose points were plotted on a linear mesh and the resultant dose map surface was generated by linearly interpolating between the measured dose points. Additionally, beneath each surface, in the grid plane, a contour heat map has been plotted.

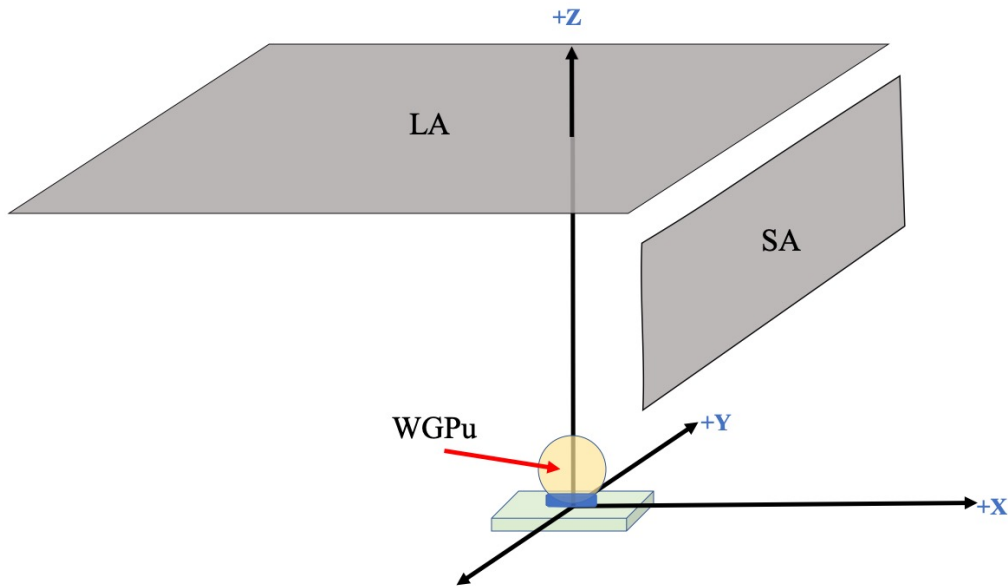


Figure 10.4: Coordinate system used for the dosimeter arrays with respect to the WGpu source.

The plot in Figure 10.5 shows an apparent maximum in the dose deposition surface near the (0,0) point in the x-y plane. It was hypothesized that this would be a near optimal measurement scenario since a global maximum implies that the dose measurements have been made on a grid fully containing the source. In contrast, the plot in Figure 10.6 shows the dose values still increasing at the edge of the z-domain, indicating that the position of the source may fall outside the dose measurement locations in the z-direction. This was indeed the case, as Figure 10.2 shows, the SA was positioned above the source.

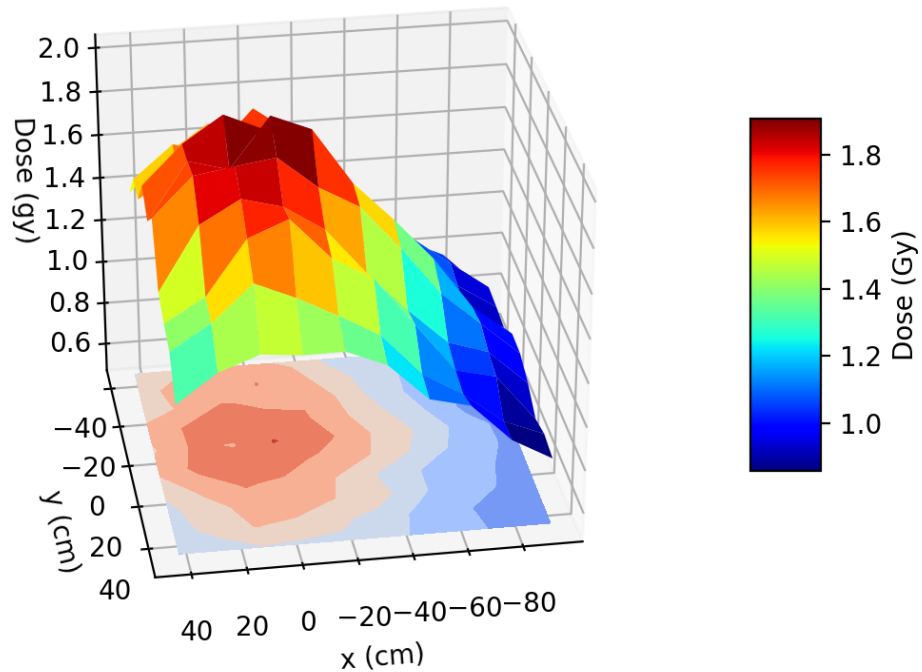


Figure 10.5: Measured doses to the OSLDs in the large array (LA). The surface map is colored according to the dose, and the doses between adjacent OSLDs were taken as simple linear interpolations. The contour map in the x-y plane shows that a dose gradient exists in both directions, and the OSLD array fully bounded the source distribution.

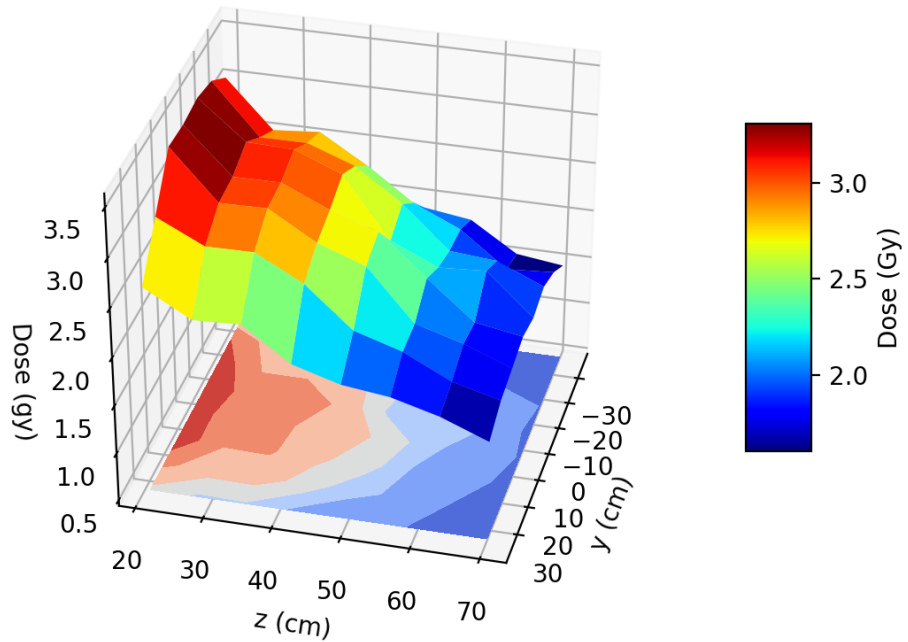


Figure 10.6: Measured doses to the OSLDs in the small array (SA). The surface map is colored according to the dose, and the doses between adjacent OSLDs were taken as simple linear interpolations. No definite peak is seen in the z-direction, indicating that the dosimeter array does not extend beyond the source location in the z-direction.

Table 10.1 contains the position estimations calculated from the doses measured in the small and large arrays, respectively, using the analytical method described in Section 10.2.1. The coordinate system for the dosimeter arrays was defined such that the center of the WGPu sphere was located at position (0,0,4.5) in centimeters.

Table 10.1: Estimated Source Position Coordinates Calculated from the Dosimeters in the Small Array (SA) and Large Array (LA).

Array	X (cm)	Y (cm)	Z (cm)
SA	4.4 ± 0.8	-0.2 ± 0.4	10 ± 5
LA	4.6 ± 0.7	-5.6 ± 0.7	2 ± 27

It can be seen from the values in Table 10.1 that the point source approximation method used to estimate the source position tends to poorly resolve all source coordinates. The largest disparity between the assumed true location and the calculated location existed in the y-coordinate estimated from the dosimeters in the large array, followed by the x-coordinate estimates. Referring to the contour plot of the dosimeter measurements in Figure 10.7, it is

apparent that larger measured doses were biased toward the negative y direction. Although steps were taken to align the central axes of each dosimeter array to bisect the center of the source, it is quite reasonable to accept that some uncertainty inevitably existed in the true source locations assumed above. The uncertainty in the x and y positions of the source were taken to be 2 cm each, while the z position uncertainty was taken to be 2 mm. The x and y uncertainty estimates were considerably larger than the z position uncertainty due to the large size of the arrays and the distance between arrays and the source.

It must also be noted that the overall resolution possible in the positional estimates will be inversely correlated to the spacing between the dosimeters, and as result it is expected that observed disagreement between the assumed true and the estimated source positions resulted from a combination of the uncertainty in the true position of the source and resolution limits imposed by the dosimeter spacing chosen. Using the uncertainty estimates for the known source position added in quadrature with position estimate uncertainties, a t-test was performed in order to compare the known source position to the estimates. Table 10.2 contains the computed *t*-values for each of the coordinates, where the critical *t* at the 95% confidence level was 1.960. It can be seen from the values in Table 10.2 that only the y-estimate from the SA and the z-estimate from the LA were statistically indistinguishable from the measured values. Therefore, there was disagreement between the known and estimated values that are not accounted for by their associated uncertainties. It was hypothesized that this excess disagreement may have been the result of resolution limits imposed by the spacing of the dosimeters in the arrays.

Table 10.2: t-Statistics Comparing the Known and Estimated Source Positions. Here the null hypothesis was that the known and estimated positions were identical.

Array	X	Y	Z
SA	9.13	0.31	3.47
LA	6.87	8.36	0.35

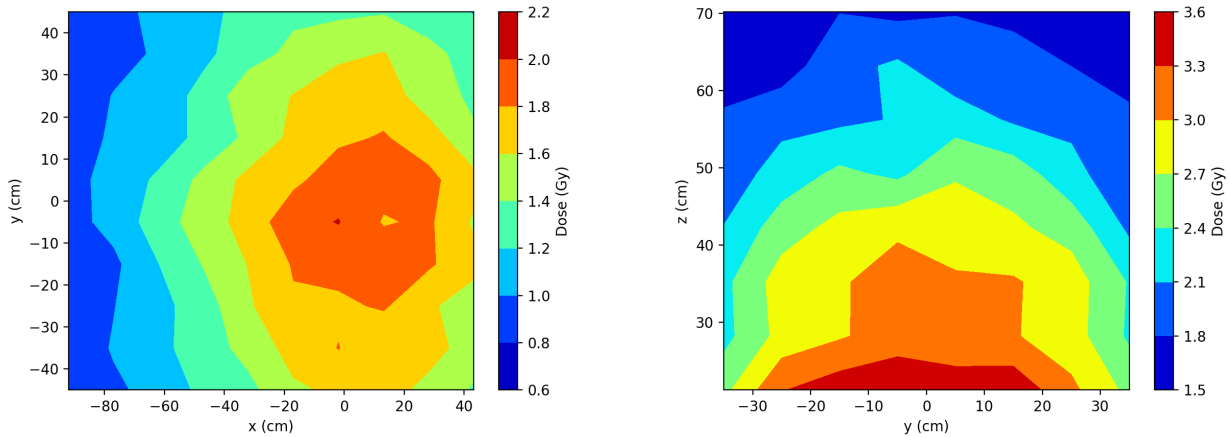


Figure 10.7: Contour plot of measured doses to the OSLDs in the Large Array (left), and Small Array (right).

Table 10.3: Estimated Source Position Coordinates Calculated from the Dosimeters in the Small Array (SA) and Large Array (LA).

Method	Array	X (cm)	Y (cm)	Z (cm)	R(cm)
raster	SA	-1.25	-1.86	10.42	4.49
raster	LA	2.32	-4.86	8.11	4.02
Brent's	SA	5.9	-0.36	18.5	4.22
Brent's	LA	11.0	-9.3	11.1	1.98

Table 10.3 contains the optimum parameters for the source position and radius using each of the inverse transport methodologies described above. It is again apparent that the resolution of the parameter estimates is dependent on the spacing between the dosimeters in the array. One of the challenges with each of the methods tested here was that the total chi-squared values for the arrays were relatively insensitive to changes in the position and source radius for a broad range of values around the true source position. For example, Figure 10.8 shows the chi-squared value for the simulated and measured dose values for the dosimeters in the small array. It can be seen that the changes in the computed chi squared were relatively small over a 5-cm range of radius

estimates. This problem is compounded by stochastic noise inherent to both the measured and simulated element doses resulting in an unavoidable baseline level of noise in the chi squared as a function of position and radius.

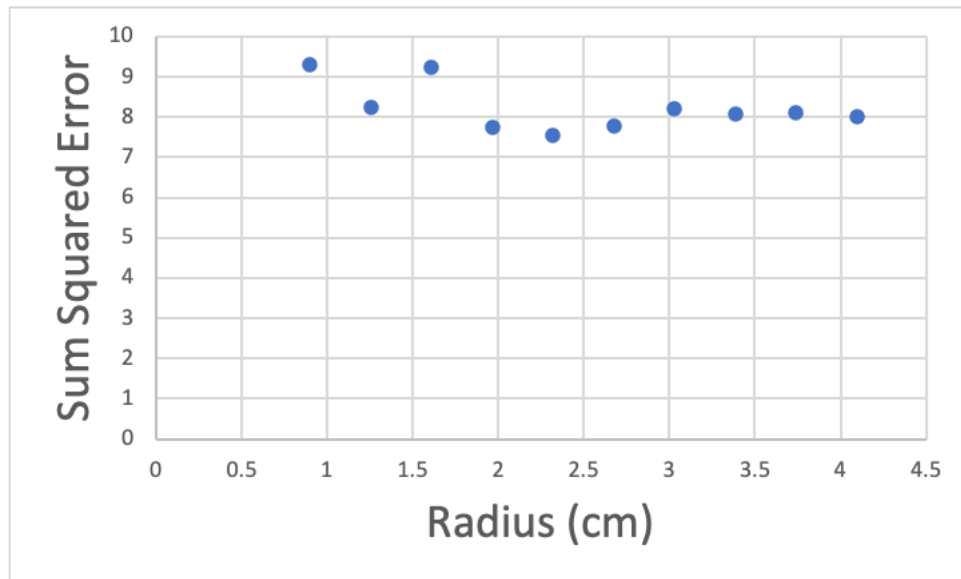


Figure 10.8: Plot of the chi squared between the simulated and measured dosimeters in the small array as a function of the simulated radius (cm).

Another possible limitation for the raster and Brent's methods is that the final results may be dependent on the order in which the parameters are optimized. The results presented in Table 10.3 were all computed by optimizing the x-, y-, and z- coordinates followed by the radius. To test this theory, the Brent's method was used to compute estimates for the radius, x-, y-, and z-coordinates (in that order) resulting in estimates that for the radius and x-position (3.73 cm and -5.6 cm, respectively) substantially differed from those presented in Table 10.3.

10.4 Conclusions

Previous analyses with a linear array of dosimeters showed promising results for estimating the axial position and radial distance of a source with respect to the line of dosimeters (Hayes and O'Mara, 2020; Chapter 9). In this work, two dimensional arrays were used to reconstruct the three-dimensional location of a spherical weapons grade plutonium source. The method consisted of using LM fitting to linearly arrayed dosimeters in orthogonal directions to obtain spatial position estimates. All positional estimates were within 12 cm of the true source position, with the majority of estimates being within 7 cm of the true values. From the position

estimates, it was clear that it is important for the dosimeter array to fully contain the profile of the source facing the array. This guarantees that the dose distribution in the array will contain points on each side of the maximum dose.

Using inverse radiation transport methods with coordinate search optimization algorithms, it was again shown that reasonable estimates of the source position (within 10 cm worst case) and source radius (within 2 cm worst case) can be obtained. The major limitation for these methods appeared to be the relatively large range of insensitivity of the chi-squared with respect to the positional and size parameters. Another potential limitation that was discovered during the course of this investigation was that when optimizing multiple parameters, the ordering in which the parameters are optimized can affect the final estimates. The magnitude of this effect, however, can be expected to be inversely proportional to the sensitivity of the results to the parameters being optimized.

In terms of return on investment, the analytical method (Section 10.1.1) would be the preferable technique for determining the position of a source from a gridded array of dose measurements. Although both of the inverse transport optimization methods required less than 500 model evaluations, and less than 2 hours running time on a single node of a cluster with 32 cores per node, the analytical method returns reasonable results within a matter of seconds on a standard laptop. In terms of making actionable determinations about the presence, or non-presence, of undisclosed source material, the results from the analytical method would be more than sufficient. However, comparable analytical techniques for determining more complex source characteristics such as size, shape, material composition and/or shielding have yet to be developed or tested. As a result, inverse transport optimization methods are, at present, the only and best option for estimating these characteristics. Therefore, future efforts should be devoted to testing the applicability of similar inverse transport optimization methods for estimating more complex, non-positional source characteristics.

Finally, although the dosimetric material used for the dose reconstructions in this study were commercially produced aluminum oxide OSLDs, the ultimate goal is to be able to achieve similar results using minerals derived from ubiquitous materials such as bricks. In general, however, minerals derived from bricks and other earthen based building materials presents additional challenges. Namely, without precise control over the dosimetric material, as there is in commercial OSLDs, there is no guarantee that any samples collected will exhibit sufficient

luminescence sensitivity to be useful, especially at low radiation doses. In addition, uncertainties in dose estimates from ubiquitous minerals tend to be higher than those from commercial OSLDs, as a result, the attainable resolution in position and size estimates is decreased for mineral samples. Still, based on the capabilities presented herein, using commercial dosimetry materials, it is likely that the actionable information could be derived using materials derived from environmental materials.

Chapter 11

Conclusion

Solid-state, retrospective dosimetry measures persistent electronic changes caused by radiation interactions in insulating and semiconducting materials. When ionizing radiation interacts with such materials, delocalized, excited electrons may become trapped at distant bound trap states. Since within a range of absorbed doses, the excitation and subsequent trapping of electrons is proportional to the dose received by the material, quantifying the populations of trapped electrons allows for the calculation of radiation dose. The materials capable of recording information about their radiation environment are everywhere and require no upkeep beyond collection and measurement to make use of their dose records. This dissertation demonstrated how simple bricks can be used as gross gamma ray spectrometers being able to accurately discriminate between the radiation fields of ^{241}Am (Chapter 4) and prompt fission gammas (Chapter 9).

Traditionally retrospective dosimetry techniques have been applied to a broad range of problems including archeological dating, emergency response dosimetry and epidemiological population dosimetry. However, the ubiquitousness of natural dosimetric materials makes them attractive for a number of new uses. In a world of rapidly expanding nuclearization and pervasive medical and industrial utilization of radiological sources, there is more need than ever for rapid, reliable and widespread radiation monitoring capabilities. Whether in the case of an unexpected release of nuclear material or illicit manufacturing of nuclear weapons, dosimeters being continuous monitors of radiation environments can provide the information to inform future decisions.

The advances in optically stimulated luminescence and thermoluminescence applications presented here have demonstrated that it is possible to not only detect the past presence of radiation, but to also characterize the energy of the radiation environment using only commonplace building materials. This was proved by accurately estimating the average source energy of both a prompt critical system and the low energy gamma field from a TRU isotope (Chapter 9). Further, using newly developed measurement protocols it is possible to carry out these studies with less sample preparation than ever before (Chapters 4 and 6). This significantly lessens the burden of these types of analyses. In addition to reduced sample preparation needs, it has also been shown that the sample readout times can be reduced by optimally selecting the dose reconstruction protocol parameters used in dose recovery experiments (Chapter 7).

Another challenge to utilizing environmental material for characterizing historical radiation environments is the confounding effect of natural background dose due to naturally occurring radioactive material (NORM). Although annually the absorbed dose rates due to environmental NORM are small, it is important to remember that the integration time for solid-state dosimetry materials is the lifetime of the material and therefore the doses received due to NORM are a constantly growing background noise contribution to the minimum detection limit. Then, the signal-to-noise ratio for an anthropogenic source decreases with increased temporal separation from the event of interest. Similarly, the age of the dosimeter material will increase the detection limit for an anthropogenically delivered dose. As a result, it can be important to be able to accurately characterize the background radiation environment within bulk, earthen materials. It was shown, in Chapter 8, that this task can be tackled with relatively modest equipment, such as a portable high-purity germanium gamma ray spectrometer.

In addition to the ability to perform radiation field energy assay using bulk materials, solid-state retrospective dosimetry has great potential for determining the historical locations of radiological sources. In Chapters 9 and 10, and Hayes and O’Mara (2020), it was shown that by using a point source approximation, it is possible to determine the historical position of radiation sources, in one to three dimensions, depending on the locations of the dosimeters with respect to the source. Alternatively, advanced black-box optimization routines can be employed to reconstruct source positions, energies and spatial extent parameters simultaneously. These black-box optimization methods have even been validated in a single-blind format where the analyst had no prior information about the identity of the source or source’s location.

While solid-state retrospective dosimetry shows great promise for nonproliferation and emergency response applications, a number of outstanding challenges and opportunities for advancement still exist. Chapter 8 showed that by combining luminescence and electronic spin resonance methods, nearly any insulating material can be used as a dosimeter. However, in a true emergency or investigative situation, access to bulk materials such as cores from bricks, electrical insulator fixtures, or surface mount resistors from electronics may not be available. In such instances, the only dosimeter material available could be surface removable minerals. It remains to be seen how applicable the methods explored in this dissertation translate to small (single grain) sample sizes. Although single grain optically stimulated luminescence dosimetry has been extensively explored for archeological dating, nonproliferation and emergency response

applications have additional challenges caused by the high likelihood of partial bleaching from ambient light sources. Electron paramagnetic resonance for surface removable minerals, on the other hand, does not suffer from light sensitivity but it is not well-equipped to handle samples sizes on the order of a few grains of sand. It remains to be seen how the challenges presented by small samples sizes may be addressed.

In summary, we have developed and tested several new applications of solid-state dosimetry to meet current deficiencies in the fields of nonproliferation and emergency response. These applications include energy assay and imaging of radiological source material, without direct access to that material. Our methods expanded the amount of information that can be obtained with the gross gamma-ray absorbed dose estimates provided by solid-state dosimetry measurements. We have also developed a technique for estimating the detectable limits for an anthropogenic exposure to materials that themselves contain trace amounts of radioactive nuclides. Finally, we have demonstrated the ability to build a solid-state dosimetry suite equipped to perform physical dosimetry with almost any crystalline insulating material in response to radiological emergencies.

REFERENCES

- Aitken, M.J., Tite, M.S., Reid J. "Thermoluminescent dating: progress report" *Archaeometry*. 6, 65–75, 1963.
- Alexander ,G.A., Swartz, H.M., Amundson, S.A., Blakely, W.F., Buddemeier, B., Gallez, B., Dainiak, N., Goans, R.E., Hayes, R.B., Lowry, P.C., Noska, M.A., Okunieff, P., Salner, A.L., Schauer, D.A., Trompier, F., Turteltaub, K.W., Voisin, P., Wiley, A.L., Wilkins, R. "BiodosEPR-2006 Meeting: Acute dosimetry consensus committee recommendations on biodosimetry applications in events involving uses of radiation by terrorists and radiation accidents." *Rad. Meas.* 42, 972–996, 2007.
- Ankjærgaard, C., Murray, A.S. "Total beta and gamma dose rates in trapped charge dating based on beta counting." *Rad. Meas.* 42, 352-359, 2007.
- Bailiff, I.K. "The Pre-Dose Technique." *Rad. Meas.* 23(2/3), 471-479, 1994.
- Bos, A.J.J., Wallinga, J., Johns, C., Abellon, R.D., Brouwer, J.C., Schaart, D.R., Murray, A.S. "Accurate calibration of a laboratory beta particle dose rate for dating purposes." *Rad. Meas.*, 41, 1020-1025, 2006.
- Bøtter-Jensen, L., Junger, H., Poolton, N.R.J. "A continuous OSL scanning method for analysis of radiation depth-dose profiles in bricks." *Rad. Meas.*, 4, 525, 1995.
- Bøtter-Jensen, L., Murray, A.S. "Optically stimulated luminescence techniques in retrospective dosimetry." *Rad. Phys. and Chem.* 61, 181, 2000.
- Bowman, S.M. and Gauld, I.C. "OrigenARP Primer: How to Perform Isotopic Depletion and Decay Calculations with SCALE/ORIGEN." ORNL/TM-2010/43, Oak Ridge National Laboratory, Oak Ridge, Tennessee, April 2010.
- Boyle, R. *Register of the Roy. Soc.* 213, 1663.
- Brent R.P. "Chapter 4: An Algorithm with Guaranteed Convergence for Finding a Zero of a Function", Algorithms for Minimization without Derivatives, Englewood Cliffs, NJ: Prentice-Hall (1973).
- Brown, F.B., Sweezy, J.E., Hayes, R.B. "Monte Carlo Parameter Studies and Uncertainty Analyses with MCNP5." Los Alamos National Lab, Los Alamos NM, LA-UR-04-0499.
- CDC (2017), Radiation from Building Materials.
<https://www.cdc.gov/nceh/radiation/building.html>, Accessed: January 20, 2018.
- Colarossi, D., Duller, G.A.T, Roberts, H.M., Tooth, S., Lyons, R. "Comparison of paired quartz OSL and feldspar post-IR IRSL dose distributions in poorly bleached fluvial sediments from South Africa." *Quaternary Geochronology* 30, 233, 2015.

Fujita, H., Sakaue, H., Nomura, S., Hashimoto, T., Nakata, Y. "Comparison of accumulated doses in quartz and feldspar extracts from atomic bomb-exposed roof tiles using several luminescence methods." *Rad. Meas.*, 41(14), 1015-1019, 2006.

Goorley, T., James, M., Booth, T., Brown, F., Bull, J., Cox, L.J., Durkee, J., Elson, J., Fensin, M., Forster, R.A., Hendricks, J., Hughes, H.G., Johns, R., Kiedrowski, B., Martz, R., Mashnik, S., McKinney, G., Pelowitz, D., Prael, R., Sweezy, J., Waters, L., Wilcox T., Zukaitis, T. "Initial MCNP6 Release Overview", *Nuclear Technology*, 180(3), 298-315, 2012.

Grün, R. "Errors in dose assessment introduced by the use of the "linear part" of a saturating dose response curve," *Rad. Meas.*, 26, 297-302, 1996.

Guskova, A.K., Barabanova, A.V., Baranov, A.Y., Gruszdev, G.P., Pyatkin, Y.K., Nadezhina, N.M., Metlyanova, N.A., Selidovkin, G.D., Moiseev, A.A., Gusef, I.A., Dorofeeva, E.M., Zykova, I.E. "Acute radiation effects in victims of the Chernobyl accident, in Appendix to Annex G of "Early effects in man of high radiation doses""", *UNSCEAR*, 1988.

Hansen, V., Murray, A., Buylaert, J.P., Yeo, E.Y., Thomsen, K. "A new irradiated quartz for beta source calibration." *Rad. Meas.*, 81, 123-127, 2015.

Hayakawa, M. "Increase in disaster-related deaths: risks and social impacts of evacuation." *Annals of the ICRP*. 45, 123-128, 2016.

Humphreys, J.C., Desrosiers, M.F., Bensen, D.L., Puhl, J.M., Seltzer, S.M., McLauhlin, W.L., Walker, M.L. "Radiation Processing Dosimetry Calibration Services: Manual of Calibration Procedures." *NIST SP*, 250-245, 1998.

Hayes, R.B., Haskell, E.H., Kenner, G.H. "A Mathematical Approach to Optimal Selection of Dose Values in The Additive Dose Method of EPR Dosimetry," *Rad. Meas*, 27, 315-323, 1997.

Hayes, R.B., Haskell, E.H., Wieser, A., Romanyukha, A.A., Hardy, B.L., Barrus, J.K. "Assessment of an alanine EPR dosimetry technique with enhanced precision and accuracy." *Nucl. Instr. Meth. A*. 440, 453-461, 2000.

Hayes, R.B. "Implementation of a Portable HPGe for Field Contamination Assay." *Health Phys.* 100, 571, 2016.

Hayes R.B., Sholom S.V. "Retrospective Imaging and Characterization of Nuclear Material." *Health Phys.* 113(2), 91-101, 2017.

Hayes, R.B., O'Mara, R.P. "Enabling Nuclear Forensics Applications from The Mineral Particulate in Contamination Surveys." *Advances in Nonproliferation Technology and Policy Conference*, Orlando Fl, Nov 12-15, 200-204, 2017.

- Hayes, R.B. O'Mara, R.P. "Retrospective Characterization of Special Nuclear Material in Time and Space." *Rad. Meas.* 133, 2020.
- Hayes, R.B., O'Mara, R.P., Hooper D.A. "Initial TL/OSL/EPR Considerations for Commercial Diatomaceous Earth in Retrospective Dosimetry and Dating." *Rad. Prot. Dosim.* 2019.
- Hayes, R.B., O'Mara, R.P. "Retrospective Dosimetry at The Natural Background Level with Commercial Surface Mount Resistors." *Rad. Meas.* 121, 42-48, 2019.
- Hayes, R.B., O'Mara, R.P., Abdelrahman, F. "Nuclear forensics via the electronic properties of particulate and samples." *ESARDA Bull.* 59, 21- 28, 2019.
- Huntley, D. J., Godfrey-Smith, D. I., Thewalt, M. L. W. "Optical dating of sediments". *Nature*. 313,105–107, 1985.
- Ichikawa, Y., Nagatomo, T., Hoshi, M., Kondo, S. "Thermoluminescence dosimetry of gamma rays from the Hiroshima atomic bomb at distances of 1.27 to 1.46 kilometers from the hypocenter." *Health Phys.* 52(4), 443-51, 1987.
- International Atomic Energy Agency (IAEA). *Incident and Trafficking Database (ITDB)* <http://www.ns.iaea.org/security/itdb.asp> (accessed October 7, 2018).
- International Atomic Energy Agency (IAEA). The interface between safety and security at nuclear power plants. Vienna: International Atomic Energy Agency; International Nuclear Safety Group No. 24; 2010.
- Jacobs, Z., Roberts, R.G. "An improved single grain OSL chronology for the sedimentary deposits from Diepkloof Rockshelter, Western Cape, South Africa." *J. Arch. Sci.* 63, 175-192, 2015.
- Jaworska, A. "Types of radiation mass casualties and their management," *Ann. Inst Super. Sanita.*, 45(3), 246-250 2009.
- Kaderit, A., Kreutzer, S. "Risø Calibration Quartz – A Challenge For B-Source Calibration. An applied study with relevance for luminescence dating.: *Measurement*, 46, 2238-2250, 2013.
- Kerns, J.R., Fry, S.F., Sahoo, N., Followill, D.S., Ibbott, G.S. "Angular dependence of the nanoDot OSL dosimeter." *Med. Phys.* 38(7), 3955-3962, 2011.
- Li, B., Jacobs, Z., Roberts, R.G., "Investigation of the Applicability of Standardised Growth Curves for OSL Dating of Quartz from Haua Fteah Cave, Libya," *Quaternary Geochronology*, 35, 1, 2016.
- McConn Jr, R.J. "Compendium of Material Composition Data for Radiation Transport Modeling." PNNL-15870 Rev. 1, 2011.

McKeever, S.W.S., *Thermoluminescence of Solids*. Cambridge University Press. New York, NY, 1985.

McKeever, S.W.S., Sholom, S. "Biodosimetry versus physical dosimetry for emergency dose assessment following large-scale radiological exposures." *Rad. Meas.* 92, 8-18, 2016.

Miles P., pymcmcstat: A Python Package for Bayesian Inference Using Delayed Rejection Adaptive Metropolis. *Journal of Open Source Software*, 4(38), 1417, 2019. <https://doi.org/10.21105/joss.01417>.

Meckback, R., Jacob, P." Gamma exposures due to radionuclides deposited in urban environments. Part II: Location factors for different deposition patterns." *Rad. Prot. Dosim.* 25(3), 181-190, 1988.

Meckback, R., Bailiff, I.K., Goksu, H.Y., Jacob, P., Stoneham, D. "Calculation and measurement of dose-depth distribution in bricks." *Rad. Prot. Dosim.* 66, 183-186, 1996.

Mosteller, R.D., Goda, J.M. "Analysis of GODIVA-IV Delayed and Super-Prompt-Critical Conditions." Los Alamos National Laboratory Report, LA-UR-09-01007, 2009.

O'Mara, R.P., Hayes, R.B. "Total Uncertainty Propagation in Monte Carlo N-Particle Dosimetry Simulations", *62nd Annual Health Physics Society Meeting*. Raleigh, NC, July 9-13, 2017.

O'Mara, R.P., Hayes, R.B. "Dose deposition profiles in untreated brick material." *Health Phys.* 114(4), 414-420, 2018.

O'Mara, R.P. "Non-Gradient Based Optimization Methods for Black-box Inverse Transport Problems." XCP-3:18-041(U), 2018b.

O'Mara, R.P., Hayes, R.B. "Grain Size and Density Separation Effects on Luminescence Dose Estimates Using Brick Material." *Advances in Nonproliferation Technology and Policy Conference*, Orlando Fl, Nov 12-15, 2018c.

O'Mara, R.P., Hayes, R.B. "Characterization and Inter-Calibration of Laboratory Irradiation Sources Used for Multiple Solid-State Dosimetry Modalities." *Rad. Phys. And Chem.* 2019. (Submitted)

Peele, R.W., Maienschein, F.C. "The absolute spectrum of photons emitted in coincidence with thermal-neutron fission of Uranium-235." ORNL-4457, Oak Ridge National Laboratory, Oak Ridge, TN, 1970.

Press, W.H. *Numerical Recipes In C: The Art of Scientific Computing*. Cambridge, Ny: Cambridge University Press. Ch 9, Pp. 347-383, 1992.

Rahu, K., Rahu, M., Tekkel, M., Veidebaum, T., Hakulinen, T., Auvinen, A., Bigbee, W.L., Hartshorne, M.F., Inskip, P.D., Boice, J.D. "Chernobyl cleanup workers from Estonia: cohort description and related epidemiological research". *J. Radiol. Prot.* **35**, 35-45, 2015.

REAC/TS. *The medical aspects of radiation incidents*. Radiation Emergency Assistance Center/Training Site, Oak Ridge Associated Universities, Oak Ridge, TN. 2017.

Rearden, B.T., Jessee, M.A., Eds., SCALE Code System, ORNL/TM-2005/39, Version 6.2, Oak Ridge National Laboratory, Oak Ridge, Tennessee, 2016.

Schwarz, R.A., Carter, L.L., Dole, T.P., Fredrickson, S.M., Templeton, B.M. "Graphical User Input Interface for MCNP." *Trans. Am. Nucl. Soc.*, 69, 401, 1993.

Shultz, J. K., Faw, R. E. *Radiation shielding*. La Grange Park, IL: American Nuclear Society. Ch 4, pp. 80-111, 2000.

Smith, R. *Uncertainty Quantification: Theory, Implementation, and Applications*. United States, Society for Industrial and Applied Mathematics, 2014.

Trowbridge J, Burbank J.E. *Am. J. Sci.*, 5(4), 55, 1898.

Virtanen, P., Gommers, R., Oliphant, T.E., Haberland, M., Reddy, T., Cournapeau, D., Burovski, E., Peterson, P., Weckesser, W., Bright, J., van der Walt, S.J., Brett, M., Wilson, J., Millman, K.J., Mayorov, N., Nelson, A.R.J., Jones, E., Kern, R., Larson, E., Carey, C.J., Polat, I., Feng, Y., Moore, E.W., VanderPlas, J., Laxalde, D., Perktold, J., Cimrman, R., Henriksen, I., Quintero, E.A., Harris, C.R., Archibald, A.M., Ribeiro, A.H., Pedregosa, F., van Mulbregt, P., SciPy 1.0 Contributors. "SciPy 1.0: Fundamental Algorithms for Scientific Computing in Python." *Nature Methods*, 17, 261-272, 2020.

Wallace, J.D. "Monte Carlo Modeling of Large-Scale NORM Sources using MCNP." *Journal of Environmental Radioactivity* 126, 55-60, 2013.

Weil, John A. *Electron Paramagnetic Resonance: Elementary Theory and Practical Applications* Hoboken, N.J.: Wiley-Interscience, 2007.

Williams ML, Havlúj F, Lefebvre RA, Wiarda D, Wieselquist WA, Pigni MT, Guals LC, Jessee MA, Lefebver JP, Gugan KJ and Rearden BT. "Sampler: A Module for Statistical Uncertainty Analysis with Scale Sequences." ORNL/TM-2005/39, Oak Ridge National Laboratory, 2018.

Wintle, A.G. "Anomalous Fading of Thermoluminescence in Mineral Samples," *Nature*, 245, 143, 1973.

Wintle, A.G., Murray, A.S. "A Review of Optically Stimulated Luminescence Characteristics and Their Relevance in Single Aliquot Regenerative Dating Protocols," *Rad. Meas.*, 41, 369, 2006.

Wintle, A.G., Adamiec, G., “Optically Stimulated Luminescence Signals from Quartz: A Review,” *Rad. Meas.*, 98, 10, 2017.

Wolberg, J. *Data Analysis Using the Method of Least Squares*, 2006, SPRINGER.

Yukihara, E.G. *Optically Stimulated Luminescence: fundamentals and applications*. West Sussex: Wiley & Sons, 2011.

Zavoisky, E. *J. Phys. U.S.S.R.*, 9(211), 245, 1945.

APPENDIX

A.1. Brick Analysis Report Provided by the Air Force Technical Applications Center



Air Force Technical Applications Center Air Force Radiochemistry Laboratory Patrick Air Force Base



WO_00000081 Gamma Spectrometry Analysis of Brick Core Samples

Introduction

The Air Force Radiochemistry Laboratory (USAF CIL) received two brick core samples for gamma spectrometry measurement from Dr. Robert Hayes at North Carolina State University. The objective of the project was to determine initial radionuclide concentrations in off-the-shelf brick samples. The initial concentrations will be used by Dr. Hayes for investigating an alternative technique to determining retrospective dose. The bricks were measured on three different gamma spectrometers; two at CIL and the ultra-low background GeMINI at Harkins Laboratory Complex.

Objective

Quantification of the major gamma-emitting radionuclides in the uranium and thorium series was requested with combined standard uncertainties less than 50%. An optional measurement quality objective was given to count until a positive detection was obtained for Cs-137.

Timeline

Two brick cores were created at North Carolina State University on Dec of 2018. The bricks were received on 2 JAN 2019 at Ciambrone Radiochemistry Laboratory at Patrick Air Force base. The bricks were measured at the Ciambrone Radiochemistry Laboratory on 3 JAN 2019 and 7 JAN 2019. The bricks were then sent to the Harkins Laboratory Complex at Cheyenne Mountain Air Force Station for additional measurement which was performed on 1 FEB 2019. Sample IDs and dimensions were determined by Ciambrone Radiochemistry Laboratory as indicated in Table 1 below. The physical dimensions of the bricks were difficult to precisely measure due to some irregular and broken edges which are assumed to be from the coring

Sample ID	F00APZ	F00APY
Description	LARGE BRICK	SMALL BRICK
diameter (cm)	6.99	6.99
height (cm)	4.45	0.95
volume (cm ³)	170.33	36.50
mass (g)	370.60	96.40
density (g/cm ³)	2.18	2.64

Setup

The average density of the two brick samples (2.41 g/cc) was noted to be very close the pre-defined density of concrete in the Canberra ISOCS Geometry Composer software (2.35g/cc), therefore the bricks were modelled as concrete. Table 2 provides the information on the instruments used for measurements. Analytes in the natural decay series were set to the half-life of the series progenitor with the exception of Pb-210 which uses its reference half-life. For a complete listing of all nuclear constants used, see the Brick Library in Appendix A. The large brick was measured on detectors G23 and H1. The small brick was measured on G30. Canberra ISOCS software was used to generate efficiency curves specific to each detector/sample combination.

Table 2. Detector models and information.

Det #	Det Model	Description
G23	GC7020	70% ptype coax, 4" standard lead shield
G30	GR5021	50% ntype coax, Compton suppressed, 4" standard lead shield
H1	GX12021	120% ptype coax, custom built ultra-low bkg, 2000 ft granite overburden

Summary Results

Summary results from all three measurements are presented in Table 3. All results employ the ISOCS detector/sample-specific efficiency curves. A systematic uncertainty factor of 10% was entered into Genie2k and is incorporated in these results as an estimate of the systematic measurement uncertainty associated with the measurement of these samples. The concentration of the analytes is compared across the two sample types. Duplicate comparisons were performed between the three measurements using a Z-score calculation. The Z-scores passed for all analytes within the typical laboratory acceptance range of ± 3 , but there were 4 analytes in the warning range of ± 2 which may be indicative of an underestimated uncertainty or bias. All results are reported at time of measurement. The only decay corrections performed are decay during the count.

Table 3. Results summary and duplicate Z-score comparison.

Sample	FO0APZ		FO0APY		FO0APZ		Z-score G23 G30	Z-score G23 H1	Z-score G30 H1
	Nuclide Name	Activity (Bq/g)	G23 A Unc (Bq/g)	G30 Activity (Bq/g)	G30 A Unc (Bq/g)	H1 Activity (Bq/g)	H1 A Unc (Bq/g)		
K-40	6.04E-01	8.7E-02	6.28E-01	9.0E-02	5.39E-01	7.7E-02	-0.2	0.6	0.7
Cs-137	N/A	N/A	N/A	N/A	N/A	N/A	N/A	N/A	N/A
Tl-208	1.36E-02	1.8E-03	1.41E-02	1.9E-03	1.14E-02	1.5E-03	-0.2	0.9	1.1
Pb-210	2.06E-02	5.8E-03	1.95E-02	4.9E-03	N/A	N/A	0.1	N/A	N/A
Bi-212	3.77E-02	5.0E-03	4.22E-02	6.1E-03	3.07E-02	4.0E-03	-0.6	1.1	1.6
Pb-212	3.41E-02	5.3E-03	3.49E-02	5.4E-03	3.00E-02	4.1E-03	-0.1	0.6	0.7
Bi-214	2.10E-02	2.4E-03	2.23E-02	2.7E-03	1.78E-02	2.1E-03	-0.4	1.0	1.4
Pb-214	2.09E-02	3.0E-03	2.19E-02	3.2E-03	1.82E-02	2.5E-03	-0.2	0.7	0.9
Ra-223	N/A	N/A	1.38E-03	6.6E-04	8.72E-04	4.0E-04	N/A	N/A	0.7
Ra-224	3.64E-02	6.7E-03	3.97E-02	7.4E-03	1.65E-02	4.5E-03	-0.3	2.5	2.7
Ra-226	2.06E-02	6.9E-03	6.52E-03	5.6E-03	4.93E-03	1.2E-02	1.6	1.1	0.1
Th-227	1.35E-03	3.1E-04	1.31E-03	3.3E-04	N/A	N/A	0.1	N/A	N/A

Ac-228	3.66E-02	4.2E-03	3.78E-02	4.4E-03	3.02E-02	3.4E-03	-0.2	1.2	1.4
Th-228	5.26E-02	1.4E-02	3.79E-02	1.4E-02	1.68E-02	9.8E-03	0.8	2.1	1.3
Th-231	N/A	N/A	7.83E-03	3.2E-03	N/A	N/A	N/A	N/A	N/A
Pa-234m	3.33E-02	6.1E-03	5.29E-02	9.8E-03	2.10E-02	4.3E-03	-1.7	1.6	2.97
Th-234	2.46E-02	6.2E-03	2.49E-02	6.3E-03	1.58E-02	5.5E-03	0.0	1.1	1.1
U-235	1.26E-03	3.3E-04	1.98E-03	4.3E-04	1.84E-03	9.0E-04	-1.3	-0.6	0.1

Detection Limits

The detection limits for the radionuclides of interest are presented in Table 4 for all three detectors used. The GeMINI detector (H1) from Harkins Laboratory is noted to provide improved detection limits for most high energy emitting radionuclides, starting at the 661 keV emission from Cs-137. The sample count times were set for a minimum of 5000 minutes (H1 measurement), and ran for as long as operationally feasible at CIL (5600 minutes on G23, and 5800 minutes on G30).

Table 4. Detection limit comparison.

Nuclide Name	G23 MDC (Bq/g)	G30 MDC (Bq/g)	H1 MDC (Bq/g)
K-40	1.3E-03	2.3E-03	9.5E-04
Cs-137	1.7E-04	2.4E-04	1.6E-04
Tl-208	1.4E-04	1.8E-04	5.8E-05
Pb-210	1.8E-02	5.4E-03	3.4E-01
Bi-212	2.3E-03	3.4E-03	2.1E-03
Pb-212	2.9E-04	3.5E-04	3.3E-04
Bi-214	3.5E-04	5.4E-04	3.4E-04
Pb-214	3.9E-04	5.1E-04	4.2E-04
Ra-223	8.7E-04	1.2E-03	1.1E-03
Ra-224	2.9E-03	3.1E-03	3.1E-03
Ra-226	3.4E-03	4.7E-03	5.3E-03
Th-227	9.9E-04	9.7E-04	2.0E-03
Ac-228	4.7E-04	9.2E-04	4.9E-04
Th-228	1.3E-02	1.4E-02	3.1E-02
Th-231	2.3E-03	2.5E-03	5.6E-03
Pa-234m	1.7E-02	2.9E-02	1.9E-02
Th-234	3.7E-03	2.9E-03	7.0E-03
U-235	2.2E-04	3.0E-04	3.4E-04

Discussion

With respect to L_C and MDA, the detection limit performance was largely as expected. The bricks contain a fair amount of radioactivity, even by CRL standards. The continuum background is principally from the brick samples, not from outside the shield or near-detector components. The GeMINI background advantage was therefore mostly negated for energies

below approximately 661 keV. The GeMINI detector was also noted to have minor disadvantages in efficiency and resolution. The efficiency of the GeMINI was hindered due to difficulty in placing the samples as close to the detector as CRL due to the inverted detector construction. The GeMINI resolution was also noted to be outside that of typical detectors at CRL. Additionally the GeMINI spectrum had peak tailing on both the low and high sides of each peak.

With respect to the detection limits provided in this report, where multiple photopeaks are provided for a radionuclide in the analysis library, Genie2k will report the lowest single-photopeak detection limit observed for that radionuclide. In the attached sample reports, the final section of each is the detection limit report which provides the Lc and MDA for each line of each nuclide in the library. For all reported analytes the best detection limits were obtained using the same energy lines across all three detectors with the single exception of Th-227, which produced a slightly improved detection limit on the GeMINI using the 256 keV emission instead of the 236 keV emission. Other examples of improved detection limits between the GeMINI and standard CRL coax are noted in the detection limit report for Nd-147 at 91 keV vs 531 keV and Eu-152 at 122 keV vs 344 keV, although these were not requested nuclides for reporting. The analysis library, Bricks_20190117.pdf, is attached to this report.

Attachments

The following supporting files are attached to the PDF version of this report.

Table 5. List of PDF Attachments.

Filename	Description
23_Lg_Brick_2.35.pdf	ISOCS geometry model of large brick on G23
30_Sm_Brick_2.35.pdf	ISOCS geometry model of small brick on G30
H1_Lg_Brick_2.35.pdf	ISOCS geometry model of large brick on H1
Bricks_20190117.pdf	Library report of nuclear data used
G23_FOOAPZ_20190103.cnf	G23 large brick spectrum
G23_FOOAPZ_20190103.pdf	G23 large brick report
G30_FOOAPY_20190107.cnf	G30 small brick spectrum
G30_FOOAPY_20190107.pdf	G30 small brick report
H1_FOOAPZ_20190201.cnf	H1 large brick spectrum
H1_FOOAPZ_20190201.pdf	H1 large brick report
Sample Results Summary Brief 2019.xls	sample results summary spreadsheet

The data contained in the attached report have been reviewed by the personnel shown below. The data are believed to be compliant with the requirements of the USAF CIL Quality Assurance Manual and usable for their intended purpose, except where specifically noted above.

[REDACTED]
1 Apr 2019
Date

[REDACTED]
01 Apr 2019
Date

 ***** LIBRARY LISTING REPORT *****

Filename: P:\TLM\GENIE2K\CAMFILES\Bricks_20190117.NLB

Nuclide Library Description:

Nuclide Name	Half-Life (Days)	Energy (keV)	Energy Uncert. (keV)	Yield (%)	Yield Uncert. (Abs.+ -)
Be-7	5.32200E+01	477.603	0.002	10.4400	0.0400
Na-22	9.50281E+02	1274.537	0.007	99.9400	0.0140
Na-24	6.24875E-01	1368.626*	0.005	99.9936	0.0015
		2754.007	0.011	99.8550	0.0050
K-40	4.55820E+11	1460.820*	0.005	10.6600	0.1700
Co-57	2.71740E+02	122.061*	0.000	85.6000	0.1700
		136.474	0.000	10.6800	0.0800
Co-58	7.08600E+01	810.759	0.002	99.4500	0.0100
Co-60	1.92528E+03	1173.228	0.003	99.8500	0.0300
		1332.492*	0.004	99.9826	0.0006
Zn-65	2.43930E+02	1115.539*	0.002	50.0400	0.1000
Sr-85	6.48490E+01	514.005*	0.002	96.0000	4.0000
Y-88	1.06627E+02	898.042	0.003	93.7000	0.3000
		1836.063*	0.012	99.2000	0.3000
		2734.000	0.500	0.7100	0.0700
Y-91	5.85100E+01	1204.800*	0.130	0.2600	0.0130
Zr-95	6.40320E+01	235.690	0.020	0.2700	0.0200
		724.192	0.004	44.2700	0.2200
		756.725*	0.012	54.3800	0.2200
Nb-97	7.04583E-01	657.940	0.090	98.2300	0.0800
		1024.400	0.300	1.0900	0.0700
Zr-97	7.04583E-01	254.170	0.140	1.1500	0.0700
		355.400	0.090	2.0900	0.0900
		507.640	0.080	5.0300	0.1900
		743.360*	0.030	93.0900	0.0300
		1147.970	0.080	2.6200	0.1000
Mo-99	2.74900E+00	181.068	0.008	6.1400	0.1200
		366.421	0.015	1.2040	0.0220
		739.500*	0.017	12.2600	0.2200
		777.921	0.020	4.3000	0.0800
		960.754	0.020	0.0960	0.0030
Rh-102	1.36673E+03	475.060	0.040	95.0000	4.0000
		631.290	0.050	56.0000	2.0000
Ru-106	3.71800E+02	428.400	0.200	0.0710	0.0030
		616.220	0.090	0.7500	0.0800
		621.930*	0.060	9.9300	0.2300
		873.490	0.050	0.4390	0.0110
		1050.410	0.060	1.5600	0.0400
		1128.070	0.050	0.4040	0.0100
Sn-113	1.15090E+02	255.134	0.010	2.1100	0.0800
		391.698*	0.003	64.9700	0.1700
I-131	8.02520E+00	80.185	0.002	2.6200	0.0400
		284.305	0.005	6.1200	0.0600

Nuclide Library Description:

Nuclide Name	Half-Life (Days)	Energy (keV)	Energy Uncert. (keV)	Yield (%)	Yield Uncert.(Abs.+-)
I-131	8.02520E+00	364.489*	0.005	81.5000	0.8000
		636.989	0.004	7.1600	0.1000
		722.911	0.005	1.7700	0.0300
Xe-131m	1.18400E+01	163.930*	0.008	1.9500	0.0600
Cs-134	7.54294E+02	569.331	0.003	15.3730	0.0170
		604.721*	0.002	97.6200	0.1100
		795.864	0.004	85.4600	0.0600
		1365.185	0.007	3.0170	0.0080
Cs-137	1.09864E+04	661.657*	0.003	85.1000	0.2000
Ce-139	1.37641E+02	165.857*	0.001	80.0000	8.0000
Ba-140	1.27527E+01	132.687	0.001	0.2020	0.0050
		162.660	0.001	6.2200	0.0900
		304.849	0.003	4.2900	0.0600
		423.722	0.001	3.1500	0.0500
		437.575	0.002	1.9290	0.0200
		537.261*	0.009	24.3900	0.2200
Ce-141	3.25110E+01	145.443*	0.001	48.4000	0.3000
Ce-143	1.37662E+00	57.356	0.007	11.7000	0.4000
		231.550	0.002	2.0500	0.0500
		293.266*	0.002	42.8000	0.4000
		350.619	0.003	3.2300	0.0400
		490.368	0.005	2.1600	0.0300
		664.571	0.015	5.6900	0.0700
		721.929	0.013	5.3900	0.0700
		880.460	0.010	1.0310	0.0130
Ce-144	2.84910E+02	80.120	0.005	1.3600	0.0600
		133.515*	0.002	11.0900	0.1900
		696.510	0.003	1.3420	0.0140
		1489.160	0.005	0.2780	0.0050
		2185.662	0.007	0.6940	0.0150
Nd-147	1.09800E+01	91.105*	0.002	28.1000	0.7000
		120.480	0.050	0.3760	0.0090
		275.374	0.015	0.9100	0.0190
		319.411	0.018	2.1300	0.0400
		398.155	0.020	0.9120	0.0190
		439.895	0.022	1.2800	0.0300
		531.016	0.022	13.4000	0.3000
		594.800	0.030	0.2830	0.0060
		685.900	0.040	0.8860	0.0180
Eu-152	4.93695E+03	121.782	0.000	28.5300	0.1600
		244.697	0.001	7.5500	0.0400
		344.278	0.001	26.5900	0.2000
		778.904	0.002	12.9300	0.0800
		964.057	0.005	14.5100	0.0700
		1085.837*	0.010	10.1100	0.0500
		1112.076	0.003	13.6700	0.0800
		1408.013	0.003	20.8700	0.0900
Eu-154	3.14143E+03	123.071*	0.001	40.4000	0.4000
		723.301	0.002	20.0600	0.1900
		1274.429	0.004	34.8000	0.3000
Hg-203	4.65940E+01	279.195*	0.001	81.5600	0.0500
Tl-208	5.11336E+12	72.805	0.000	2.0100	0.0600

Nuclide Library Description:

Nuclide Name	Half-Life (Days)	Energy (keV)	Energy Uncert. (keV)	Yield (%)	Yield Uncert.(Abs.+ -)
Tl-208	5.11336E+12	74.969	0.000	3.3500	0.0900
		233.360	0.150	0.3100	0.0100
		252.610	0.010	0.7800	0.0200
		277.371	0.005	6.6000	0.3000
		583.187*	0.002	85.0000	0.3000
		722.040	0.120	0.2400	0.0400
		763.130	0.080	1.7900	0.0300
		860.557	0.004	12.5000	0.1000
		1093.900	0.200	0.4300	0.0200
		2614.511	0.010	99.7540	0.0040
Pb-210	8.10833E+03	46.539*	0.001	4.2500	0.0400
Bi-212	5.11336E+12	39.857	0.004	1.0600	0.0900
		288.200	0.040	0.3370	0.0030
		452.980	0.050	0.3630	0.0030
		727.330	0.009	6.6700	0.0900
		785.370	0.080	1.1020	0.0130
		893.408	0.005	0.3780	0.0190
		952.120	0.011	0.1700	0.0300
		1078.620	0.010	0.5640	0.0190
		1512.700	0.300	0.2900	0.0400
		1620.500	0.100	1.4700	0.0300
Pb-212	5.11336E+12	115.183	0.005	0.5960	0.0090
		176.680	0.050	0.0520	0.0060
		238.632	0.002	43.6000	0.5000
		300.087	0.010	3.3000	0.0400
		609.320*	0.005	45.4900	0.1600
Bi-214	1.63189E+12	703.110	0.040	0.4720	0.0090
		768.360	0.005	4.8940	0.0110
		806.180	0.009	1.2640	0.0050
		934.056	0.006	3.1070	0.0100
		1120.294	0.006	14.9200	0.0300
		1238.122	0.007	5.8340	0.0150
		1280.976	0.010	1.4340	0.0060
		1377.669	0.008	3.9880	0.0110
		1385.310	0.013	0.7930	0.0050
		1401.515	0.012	1.3300	0.0050
		1407.988	0.011	2.3940	0.0070
		1509.210	0.010	2.1300	0.0100
		1583.204	0.015	0.7050	0.0050
		1661.274	0.016	1.0470	0.0060
		1729.595	0.011	2.8780	0.0080
		1764.491	0.010	15.3000	0.0300
		1847.429	0.013	2.0250	0.0090
		2118.514	0.019	1.1600	0.0060
		2204.059	0.022	4.9240	0.0180
Pb-214	1.63189E+12	53.228	0.002	1.0750	0.0070
		77.107	0.000	9.7000	0.5000
		241.995	0.002	7.2510	0.0160
		258.860	0.030	0.5310	0.0040
		274.800	0.040	0.3550	0.0100
		295.223	0.002	18.4200	0.0400
		351.932*	0.002	35.6000	0.0700

Nuclide Library Description:

Nuclide Name	Half-Life (Days)	Energy (keV)	Energy Uncert. (keV)	Yield (%)	Yield Uncert.(Abs.+ -)
Pb-214	1.63189E+12	487.140	0.060	0.4320	0.0050
		580.140	0.030	0.3700	0.0040
		785.960	0.080	1.0600	0.0300
		839.070	0.080	0.5830	0.0080
Ra-223	2.57056E+11	154.208	0.010	5.7000	0.1600
		269.463	0.010	13.9000	0.3000
		338.282	0.010	2.8400	0.0700
Ra-224	5.11336E+12	240.986	0.006	4.1000	0.0500
Ra-226	1.63189E+12	186.211	0.013	3.6400	0.0400
Th-227	2.57056E+11	235.960	0.020	12.9000	1.1000
		256.230	0.020	7.0000	0.6000
Ac-228	5.11336E+12	329.850	0.020	2.9000	0.3000
		57.766	0.005	0.4700	0.0300
		99.509	0.006	1.2600	0.0700
		129.065	0.001	2.4200	0.0900
		153.977	0.010	0.7220	0.0210
		209.253	0.006	3.8900	0.0700
		270.245	0.006	3.4600	0.0600
		328.000	0.006	2.9500	0.1200
		338.320	0.003	11.2700	0.1900
		409.462	0.006	1.9200	0.0400
		463.004	0.006	4.4000	0.0700
		562.500	0.006	0.8700	0.0300
		674.750	0.006	2.1000	0.7000
		726.863	0.015	0.6200	0.0800
		755.315	0.004	1.0000	0.0300
		772.291	0.005	1.4900	0.0300
		782.142	0.005	0.4850	0.0190
		794.947	0.005	4.2500	0.0700
		830.486	0.008	0.5400	0.0210
		835.710	0.006	1.6100	0.0600
		840.377	0.007	0.9100	0.0400
		911.204*	0.004	25.8000	0.4000
		964.766	0.010	4.9900	0.0900
		968.971	0.017	15.8000	0.3000
Th-228	5.11336E+12	1247.080	0.040	0.5000	0.0300
		1495.910	0.020	0.8600	0.0400
		1501.570	0.050	0.4600	0.0300
		1580.530	0.030	0.6000	0.0400
		1588.200	0.030	3.2200	0.0800
		1630.627	0.010	1.5100	0.0400
		1638.281	0.010	0.4700	0.0300
		84.373	0.003	1.1900	0.0400
		215.983	0.005	0.2470	0.0080
Th-231	2.57056E+11	81.501	0.001	1.3200	0.0400
		84.214*	0.001	6.6000	0.4000
		89.950	0.020	1.0000	0.0600
Pa-233	2.69750E+01	311.904	0.005	38.5000	0.4000
Pa-234m	1.63189E+12	258.227	0.003	0.0764	0.0021
		742.813	0.005	0.1066	0.0023
		766.420	0.100	0.3170	0.0050
		1001.030	0.100	0.8420	0.0080

Nuclide Library Description:

Nuclide Name	Half-Life (Days)	Energy (keV)	Energy Uncert. (keV)	Yield (%)	Yield Uncert.(Abs.+-)
Th-234	1.63189E+12	63.290	0.020	3.7000	0.4000
		92.590	0.010	4.2300	0.2000
U-234	8.96664E+07	120.900*	0.020	0.0350	0.0050
U-235	2.57056E+11	105.604	0.000	1.3100	0.0300
		143.760	0.020	10.9600	0.1400
		163.356	0.003	5.0800	0.0600
		185.715	0.005	57.0000	0.6000
		205.316	0.010	5.0200	0.0600
U-237	6.75000E+00	59.541	0.000	34.5000	0.8000
		97.069	0.000	15.4000	0.4000
		101.059	0.000	24.5000	0.6000
		208.005	0.023	21.2000	0.3000
Np-238	2.11700E+00	984.450*	0.070	25.2000	0.3000
		1025.870	0.020	8.7500	0.0700
		1028.530	0.020	18.2300	0.1200
Am-241	1.58003E+05	59.541	0.000	35.9000	0.4000

* = key line

TOTALS: 52 Nuclides 215 Energy Lines